Reconstruction of the Subsidence and Uplift History of a proposed CO$_2$ Storage Site in the Northern North Sea

Jens Fredrik Kolnes

Thesis submitted for the degree of

Geology

60 credits

Department of Geoscience

Faculty of mathematics and natural sciences

UNIVERSITY OF OSLO

01.06.19

Reconstruction of the Subsidence and Uplift History of a proposed CO_2 Storage Site in the Northern North Sea

Abstract

This study aims to reconstruct the subsidence and uplift history of Smeaheia, a proposed long-term CO2 storage site, located on the Horda Platform in the northern North Sea. The storage site is situated between extensive subsidence in the Viking Graben and uplift of southern Norway. Rock properties that govern the storage capacity and the seal integrity of storage formations can be significantly affected by the target formations subsidence and uplift history. The uplift history of Norway and the Norwegian continental shelf is complex and consist of several phases. The offshore basins response to this uplift is still greatly debated. Considering Smeaheia's location, quantifying maximum burial depth, potential exposure to chemical compaction and net-uplift is therefore important for assessing storage capacity and seal integrity. In order to perform a genuine reconstruction of the subsidence and uplift history, net-erosion above the marked Pleistocene unconformity had to be estimated. Post- and pre-stack seismic inversion were performed to obtain velocity and lithology data. This data was further utilized to estimate net-erosion, by comparing velocities of predicted clean sandstone units with velocity trends for the equivalent lithology. The reconstruction was then performed using backstripping methodology, with net-erosion estimation and paleobathymetries as constraints. A great amount of uncertainty was observed in the methodology and data used to estimate net-erosion. The uncertainties were greatest above the Beta Structure. A range of burial histories has therefore been proposed for the Beta Structure, from quantifying the uncertainties with the greatest impact. The minimum scenario suggests that the Beta Structure was exposed to chemical compaction for a couple of million years, and uplifted 1200 m. This is comparable with the burial history that was reconstructed for the Alpha Structure. The maximum burial history for the Beta Structure suggest 60 million years of chemical compaction, reaching a maximum temperature of 95 ^{o}C. This can result in a significant reduction in storage capacity. Furthermore, the maximum burial history also suggests that the Beta Structure has been uplifted approximately 1800 m. This extends a proposed limit of uplift from where formations are more prone to fracture development and subsequent CO2 leakage.

II

Preface

This thesis was completed as part of a two-year master program in Geosciences at the Department of Geosciences, University of Oslo (UiO) in the candidacy of the M.Sc. in Geology.

This thesis was also a part of the collaboration with UiO and NCCS, an industry driven innovation for fast track CCS deployment, hosted by SINTEF. The available seismic data was provided by Gassnova.

Acknowledgements

Contents

7   Conclusions   **75**

List of Figures

XI

Chapter 1

Introduction

1.1 Background

The Intergovernmental Panel on Climate Change (IPCC) has recognized Carbon Capture and Storage (CCS) as of one the main contributors to manage the ongoing global warming (Metz et al., 2005). By 2020, the Norwegian Government has set a goal to finish a full-scale CCS project, making Norway one of the world's leaders in this new technology (the Ministry of Petroleum and Energy, 2014). Plans to captured and transport CO_2, from three localities onshore Norway to the Smeaheia area east of the Troll Field for CO_2 storage began in 2016 (Halland et al. 2011; Fig. 1.1). Identifying and evaluating such storage sites are essential aspects in CCS (Halland et al., 2011).

The Smeahiea storage site consists of two structural closures, Alpha and Beta, situated at 1250 meters (m) and 980 m depth, respectively, both consisting of late Jurassic reservoir- and caprock formations. These formations are known to work excellent as a petroleum system for the Troll Field, where oil and gas are produced (Mulrooney et al., 2018). Even though the geological setting between Smeaheia and the Troll Field is similar, a different subsidence and uplift history can result in significant effects on rock properties such as porosity and brittleness (Doré and Jensen, 1996; Nygård et al., 2006; Bjørlykke and Jahren, 2010; Henriksen et al., 2011). These properties need to be evaluated, to ensure enough storage capacity and to avoid leakage of CO_2 (Shukla et al., 2010; Hellevang, 2015; Baig et al., 2019). Considering Smeaheias location, between

1

extensive subsidence in Viking Graben and uplift of Norway, reconstructing the Alpha and Beta Structures subsidence and uplift history is important for anticipating the rock properties of the proposed storage site.
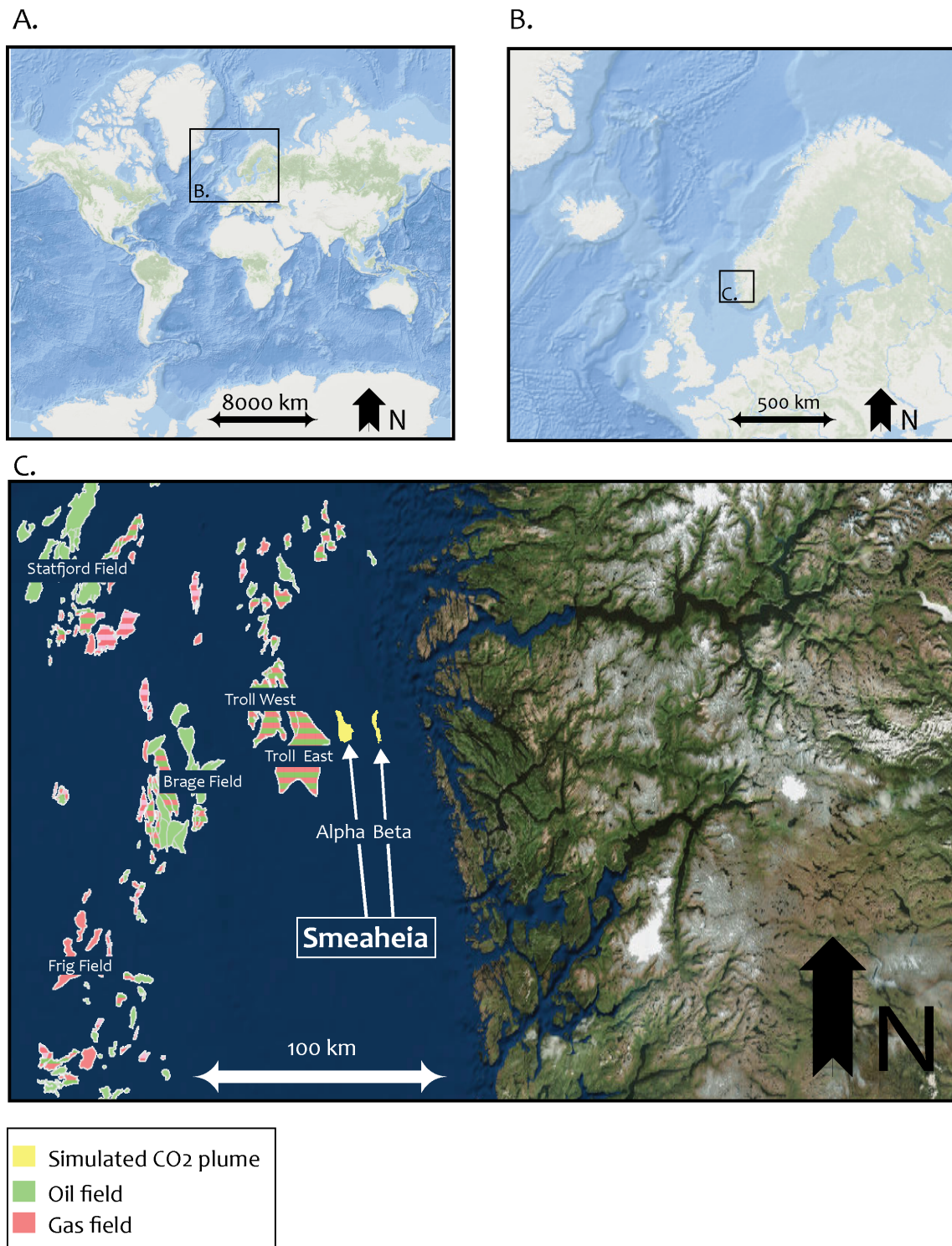
Figure 1.1. A. World map. B. North Atlantic. C. Map of the study area. Red and green polygons outline major oil and gas discoveries, yellow polygons are the simulated CO_2-plume beneath the Alpha and Beta Structures.

Although the subsidence and uplift history for major parts of the North Sea has been investigated and is well understood (McKenzie, 1978; Jordt et al., 1995; Færseth, 1996; Doré and Jensen, 1996; Riis, 1996; Odinsen et al., 2000; Faleide et al., 2002; Baig et al., 2019), the basins response to development of Norway and the development of Norway is still debated (Doré and Jensen, 1996; Eyles, 1996; Riis, 1996; Lidmar-Bergström et al., 2000; Praeg et al., 2005; Stoker et al., 2005; Holford et al., 2008; Anell et al., 2009; Nielsen et al., 2010; Baig et al., 2019). A great deal of the debate concerns when and how the mountains of Norway developed, particularly with respect to the effects of climate and isostasy (Molnar, 2004; Ebbing and Olesen, 2005; Nielsen et al., 2009, 2010) which can create sedimentary signals similar to those generated by tectonic uplift. In addition, the effects of the break-up of the Atlantic Ocean, impingement of the Iceland Plume and far-field stresses related to orogenic events have all been postulated to affect the margins surrounding the North Atlantic (Boldreel and Andersen, 1998; Clift and Turner, 1998; Japsen and Chalmers, 2000; Holford et al., 2008; Anell et al., 2009).

Backstripping is a suitable method for reconstructing the burial history of sedimentary formations. The method has been utilized in the northern North Sea to analyze stretching factors, source rock maturity and hydrocarbon migration (Odinsen et al., 2000; Kjennerud and Sylta, 2001; Kyrkjebø et al., 2001; Faleide et al., 2002; Fjeldskaar et al., 2004; Roberts et al., 1993; Baig et al., 2019; Roberts et al., 2019). This basin modeling tool takes into account important processes in the development of sedimentary basins e.g. rift- and thermal subsidence, compaction, faulting, and structural deformation (McKenzie, 1978; Sclater and Christie, 1980). However, additional constraints are needed to achieve a genuine reconstruction from backstripping, such as paleobathymetries and amount of eroded stratigraphy above major unconformities (Kjennerud and Sylta, 2001; Kyrkjebø et al., 2001; Roberts et al., 1993, 2019).

Net-erosion is the difference in a formations maximum burial depth and its present depth, and it is therefore a good analog to the amount eroded overburden (Henriksen et al., 2011). A common way to estimate net-erosion is to compare measured velocities for a specific lithology, with a calibrated velocity trend for the equivalent lithology (Japsen and Chalmers, 2000; Baig et al., 2016, 2019). This methodology has shown to give comparable net-erosion estimations as other methods such as thermal alteration index, apatite fission track analysis and vitrinite reflectance measurements

(Løseth et al., 1993; Baig et al., 2019). Velocity trends can be constructed from laboratory (Marcussen et al., 2010a), calculated from porosity trends (Japsen et al., 2007) or evaluated from trends observed in well logs (Storvoll et al., 2005). To evaluate velocities of specific lithologies in the subsurface, a common approach is to use different petrophysical well logs to interpret clean lithologies and extract their velocity (Baig et al., 2016, 2019). Seismic stacking velocities has also been used to estimate net-erosion (Løseth et al., 1993; Richardsen et al., 1993). A benefit of utilizing stacking velocities is the more spacious and dense net-erosion estimations compared to sparse estimations obtained from well log data. A challenge with the stacking velocities, is poor lithology control. This has been solved by evaluate a formation whose lithology is well documented (Løseth et al., 1993; Richardsen et al., 1993). However, techniques that are more recent allow for lithology prediction from pre-stack seismic (Whitcombe et al., 2002).

The seismic amplitudes sensitivity to fluid and lithology effects has in the recent decades been understood and utilized to extract the subsequent information from seismic pre-stack data (Smith and Gidlow, 1987; Rutherford and Williams, 1989; Castagna and Swan, 1997; Connolly, 1999; Whitcombe et al., 2002). Newer techniques take advantage of the idea that the seismic amplitude changes with offset (AVO). These AVO signatures can be modeled by elastic parameters such as the P- and S-wave velocity and density (Zoeppritz, 1919). Estimated sections and volumes of these elastic parameters can therefore be obtained indirectly by deriving models that explain acquired seismic pre-stack data (Russell, 1988; Hampson et al., 2005).

1.2   Objectives

This thesis aims to reconstruct the subsidence and uplift history for both the Alpha and Beta Structure at the proposed storage site. The reconstruction is performed using backstripping methodology, incorporating thermal subsidence, decompaction, unfolding, and fault-movement. The fundamental input parameters for the reconstruction model are; (1) horizons and faults from seismic interpretation, (2) lithologies interpreted from well logs, and (3) rock parameters estimated from Sclater and Christie

(1980)'s relations. To constrain the backstripping, we used paleobathymetries for certain time steps adapted from Kyrkjebø et al. (2001). In addition, estimations of net-erosion were obtained utilizing inverted velocity and litholog data from seismic pre-stack data. Where the intention to estimate net-erosion covering the entire study area, above the pronounced Pleistocene unconformity were late Mesozoic and early Cenozoic formations are tilted and eroded, and sub-crop below the Quaternary sediments (Faleide et al., 2002).

From the burial history curve recovered from the reconstruction, Smeaheia's response to the development of Norway, when potential uplift events occurred and maximum burial depth were discussed. The impact the subsidence and uplift history has potentially had on storage capacity and seal integrity is also addressed. Essential aspects that is considered are (1) how rapid the formations were buried, (2) their potential exposure to chemical compaction, (3) maximum temperatures reached, and (4) the extent of uplift (Fig. 1.2).
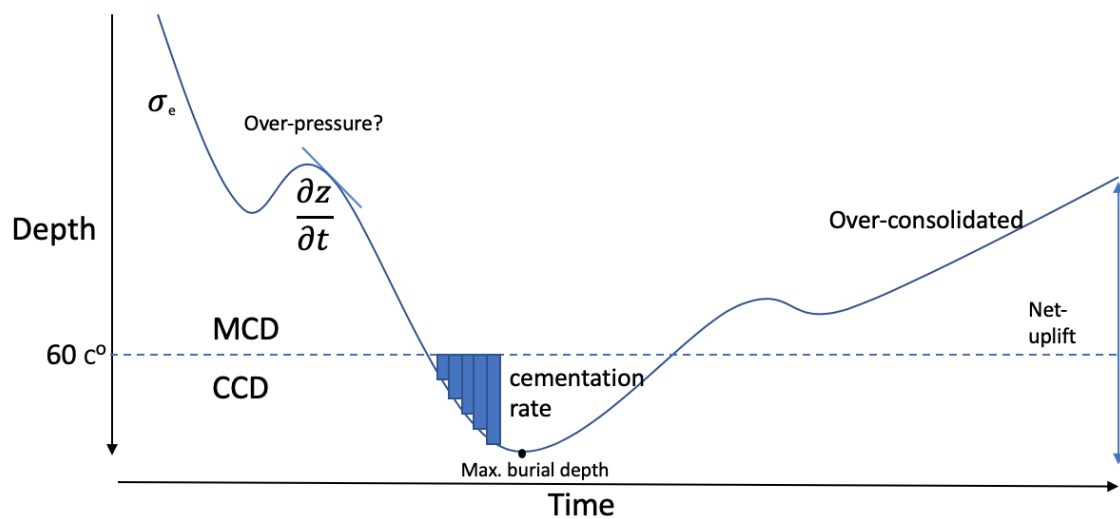
Figure 1.2. Conceptual burial history curve. Outlining different effects on rock property, such as; 1. pore-pressure from rapid subsidence, 2. cementation, and 3. overconsolidation. Modified from Bjørlykke and Jahren (2010). MCD = Mechanical Compaction Domain; CCD = Chemical Compaction Domain.

A short description of each chapter in the thesis is given below:

- **Chapter 2:** The regional and local geological settings for the study area are addressed. The main focus is on the development of the basin, the structural configuration of the Horda Platform, the subsidence and uplift history of the northern North Sea and southern Norway, and the stratigraphy of the storage formations.

- **Chapter 3:** An introduction to CO_2 storage, and the effects of burial and uplift to silica clastic sediments and the implication of the effects on storage of CO_2 are given. Furthermore, the theory behind the methodologies used in the thesis is described, including seismic modeling and inversion.

- **Chapter 4:** Overview of the available data and description of the methods used. The uncertainties regarding both the data and methods are also addressed.

- **Chapter 5:** Description and interpretation of the results, including; seismic interpretation, seismic inversion results, net-erosion estimates, and the reconstruction modeling.

- **Chapter 6:** A short summary of the interpretations, and the strengths and weaknesses of the interpretation are assessed. Furthermore, a comparison of the interpretation of earlier understanding and studies regarding the same topic are discussed. We also discuss how the burial history has affected the rock properties for CO_2 storage. Finally, recommended further work is addressed, how to improve the methods and what aspects to address regarding the storage site.

- **Chapter 7:** The main findings and conclusions of the thesis.

Chapter 2

Geological Setting

Smeaheia is situated on the northeastern edge of the Horda Platform in the northern North Sea (Mulrooney et al. 2018; Fig. 2.1). The northern North Sea has developed through a series of failed rifting events, following the collapse of the Caledonian Orogeny (Faleide et al., 2015). Several provenance areas surrounding the basin have been uplifted and sediment has filled in the accommodation space created by the rift and the following thermal subsidence (Anell et al., 2009; Jordt et al., 1995; Faleide et al., 2015).

In the Palaeozoic, Laurentia, Baltica and Avalonia collided and formed the 2000 km long Caledonian mountain chain, which matched the present day Himalayan mountain chain in length and summit elevation (> 8000 m; Gasser 2014). The orogeny covered areas in the North Atlantic such as the present Greenland, Scandes, British Isle and Svalbard. Devonian basins, which can be found on the present British Isle, contain rocks such as red sandstones, breccia and volcanic rocks, indicating the time of collapse (Norton et al., 1986). The extension related to the collapse of the Caledonian Orogeny formed structures that are believed to have influenced the configuration of younger features developing in later rifting events (Fossen et al., 2017).
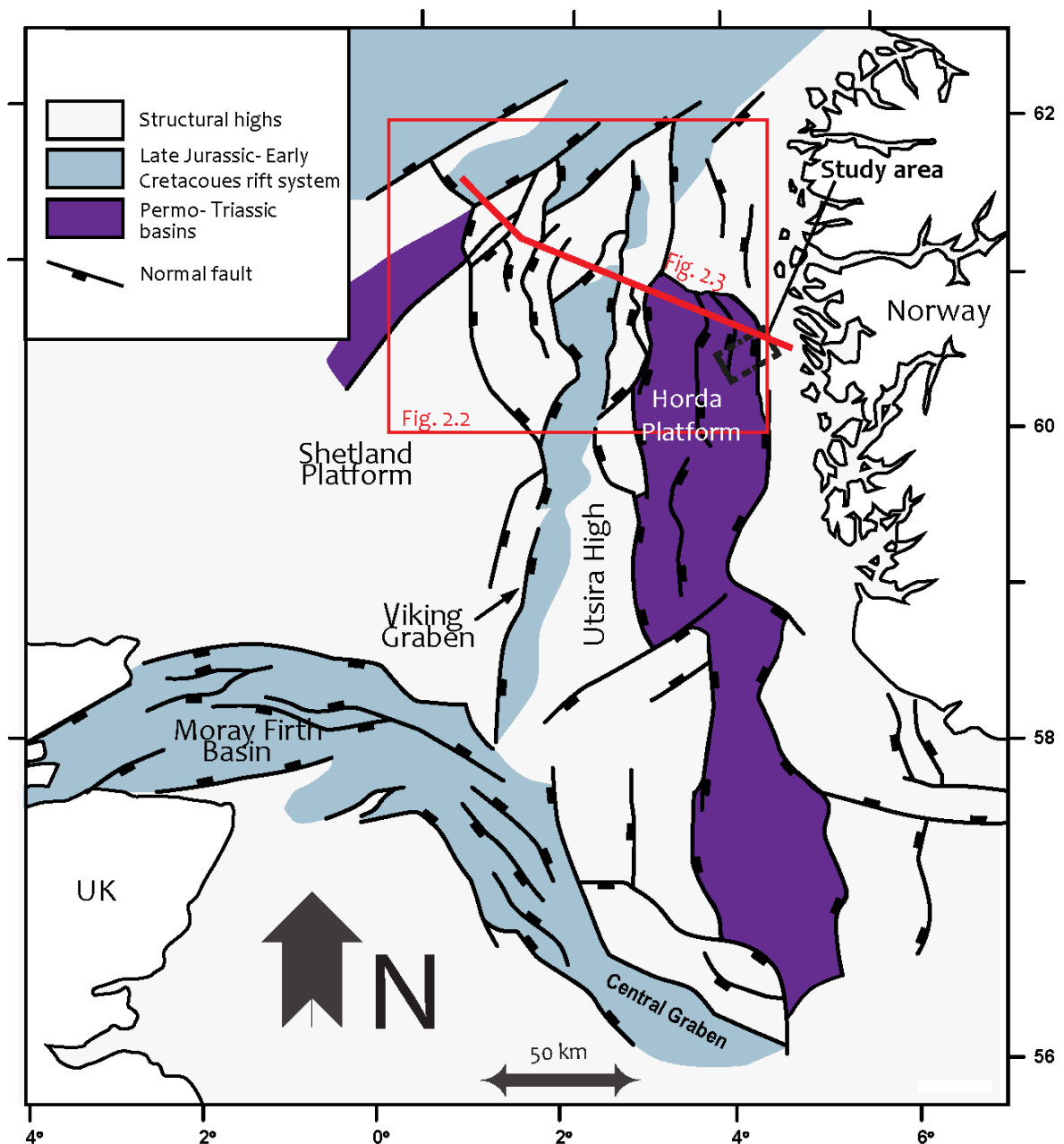
Figure 2.1. Geological map of the North Sea showing the main rift systems, the resulting basins, important geological features, and the location of the study area (dashed box). Adapted from Whipp et al. (2014)

The main rifting events in the northern North Sea occurred during the Permo-Triassic and the late Jurassic to mid Cretaceous. The Permo-Triassic event shaped a 150 km wide basin, with deep-rooted faults, thick syn-rift wedges and was centered below the present Horda Platform (Fig. 2.1). The Late Jurassic to Mid Cretaceous event had a narrower range, 25-40 km, and propagated to the west and thereby weak stretching occurred on the Horda Platform (Fig. 2.2; Roberts et al. 1993; Faerseth 1997; Roberts

et al. 2019). After both rift events followed phases of thermal cooling and subsidence. Using backstripping, Odinsen et al. (2000) found that to explain the present observed subsidence on the Horda Platform, the thermal subsidence from the Permo-Triassic rift must have continued into the onset of the late Jurassic to mid Cretaceous rift. They also found that both rift events and the thermal subsidence which followed, is not enough to explain the total subsidence seen at present, which reflects the presence of a Devonian-Carboniferous rifting event.
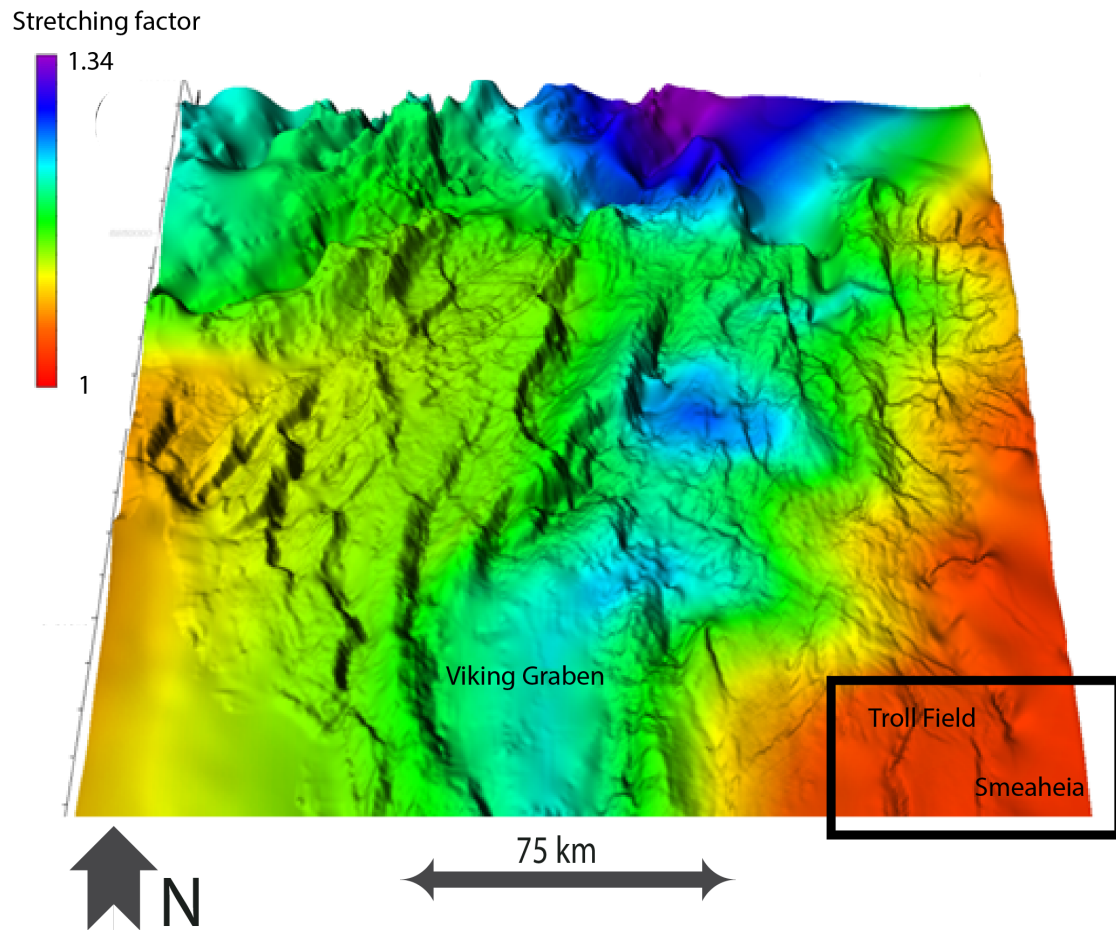
Figure 2.2. Structural map of the northern North Sea, color coded by the stretching factor from the late Jurassic to mid Cretaceous rift phase. Note how, close to no stretching has occurred on the Horda Platform area. Modified from Roberts et al. (2019).

The Horda Platform consists of several approximately 60 km long N-S trending fault blocks, which are believed to be rooted in Caledonian zones of crustal weakness (Fig. 2.3; Whipp et al. 2014). Syn-rift strata can be observed in the Permo-Triassic and in the early to late Cretaceous successions, which indicates periods of active faulting.

This indicates that the late Jurassic to mid Cretaceous rift affected the Horda Platform later than the northern North Sea (Færseth, 1996). Such diachronous sate Mesozoic faulting is recognized throughout the northern North Sea (Rattey and Hayward, 1993).
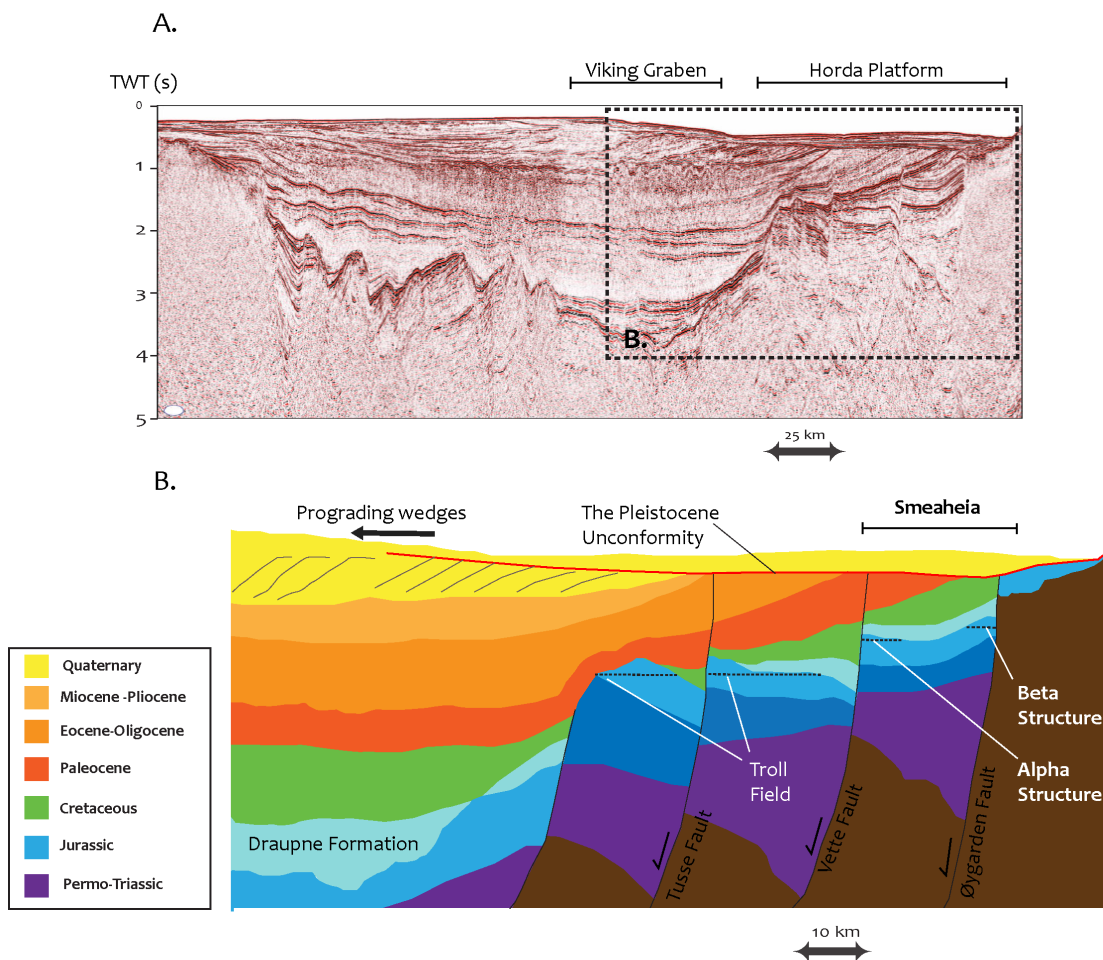
Figure 2.3. A. Regional seismic section across the northern North Sea from Faleide et al. (2015). B. Geological section of the Viking Graben and Horda Platform, highlighting the Pleistocene Unconformity, the Troll Field, and the Alpha and the Beta Structure.

The model for quantifying both rifting- and thermal subsidence was developed by McKenzie (1978) and fits well for most of the development of the northern North Sea, except for an anomalous uplift event in the Paleocene, approximated to be 300-500 m, and followed by an anomalous high rate of subsidence rate in the Eocene (Nadin and Kusznir, 1995). In the transition from the Eocene to the Oligocene, southern Norway is believed to have undergone extensive uplift, which has supposedly continued into the Miocene (Jordt et al., 1995). Together with sea-level fall, the uplift has caused a marked hiatus in the northern North Sea (Clausen et al., 1999; Faleide et al., 2002). Younger

uplift of the eastern flank of the northern North Sea, believed to have occurred in the early parts of the Quaternary (Baig et al., 2019), is reflected in a west to east upwards tilt of the Cenozoic succession pre-Quaternary and has subsequently been eroded, and is known as the Pleistocene Angular Unconformity (PU; Faleide et al. 2002). Japsen and Chalmers (2000) identify two significant uplift episodes along the North Atlantic during the Cenozoic: (1) Palaeogene and (2) late Neogene and Quaternary. The result of the latter one is a basin margin unconformity, present along almost all the margins of the North Atlantic. On the Horda Platform, not only is this tilt readily observed in the Cenozoic stratigraphy, additionally residual oil columns thicken westwards beneath the major hydrocarbon accumulations in the Troll Field (Faleide et al., 2015).

Paleo-bathymetry has been mapped in the northern North Sea by several authors e.g. Kjennerud and Sylta (2001); Kyrkjebø et al. (2001); Roberts et al. (2019). In the early Cretaceous, the sea-level gradually fell, while fluctuating between transgressive episodes. Reversing in the mid Cretaceous, where the water-depths reached $200-500$ m. Whereas in the late Cretaceous the trend was shallowing again. These Cretaceous fluctuations correspond well with eustatic sea-level changes. Moreover, in the Cenozoic deepening trends are observed in Paleocene and from late Miocene to early Pliocene, and shallowing trends in the late Eocene to early Miocene and in the Pliocene (Kyrkjebø et al., 2001).

In the transition from Triassic to Jurassic, both the climate and depositional environment changed from arid and continental, to humid and shallow marine on the Norwegian Continental Shelft (NCS; Johannesen and Nøttvedt 2008). The main reservoir, source, and caprocks on the NCS were deposited in the Jurassic (Johannesen and Nøttvedt, 2008). Low subsidence rates and sandy influx from the west across the shallow platform generated a three sandy delta formations, the Krossfjord, Fensfjord, and Sognefjord formations (Stewart et al., 1995), with locations seemingly linking up with the mouths of Norwegian fjords (Faleide et al., 2015). These deltaic depositions are inter-fingered by the fine-grained Heather Formation, consisting of fine-grained sediments, from the west and thicken eastwards (Stewart et al. 1995; Fig. 2.4). The Sognefjord Formation is the primary reservoir unit in the Troll Field, where it has been classified with excellent reservoir properties and is the target storage formation for Smeaheia (Halland et al., 2011).

AGE	EPOC	STAGE	Northern Viking Graben	Horda Platform
Jurassic		Valangian		
		Ryazanian	Draupne Formaiton	
	Upper	Volgian	Heather Formation	Sognefjord Formaiton / Fennsfjord Formaiton / Krossfjord Formaiton / Tarbret Formation
		Kimmerigan		
		Oxfordian		
	Middle	Callovian		
		Bathonian		
		Bajocian/aalenian	Dunlin Group	Ness Formation / Rannoch/Etive Formation
		Toarcian		

Legend:
- Shallow marine sands
- Terrestiral sands and coal deposits
- Deep marine silt and shales
- Organic rich shale

Figure 2.4. Lithostratigraphy of the mid to late Jurassic, covering the storage formations (Sognefjord, Krossfjord and Fensfjord Formation) and the primary seal formation (Draupne Formation). Modified from Stewart et al. (1995).

The Sognefjord Formation has been thoroughly studied with respect to depositional environment and sequence stratigraphy (Stewart et al., 1995; Dreyer et al., 2005; Patruno et al., 2015). Patruno et al. (2015) interpreted the formation, based on clinoform morphology, as a shallow marine both wave and tide-dominated system, prograding westwards across the Horda Platform.

Chapter 3

Key Concepts

3.1 CO$_2$ storage

Human emissions of greenhouse gases, such as CO$_2$, is believed to be the main cause of recent temperature rise (Metz et al., 2005). The IPCC recognizes CCS as one of the major contributors to handle and constraint the recent warming. CCS is a young technology that comes with high costs and risks, hence, research is needed to make sure it is viable (Hellevang, 2015). CO$_2$ storage involves injecting large amounts of CO$_2$ into suitable geological formations. From the exploration history on the NCS, suitable storage formations, such as saline aquifers and abandoned hydrocarbon fields, have been extensively mapped (Halland et al., 2011). NCS is therefore a potential CO$_2$ storage region for northern Europe.

3.1.1 Storage Capacity

Evaluating the properties, such as storage capacity and seal integrity, of potential storage formations is one of the important research objectives for assessing the success of CCS. Storage capacity (m_{CO_2}) is determined by several factors (Eq. 3.1) (Halland et al., 2011). The bulk volume of the storage formation (V_b) and the Net to Gross (N/G) are the primary controlling factors for the storage capacity. The storage capacity is also greatly affected by the porosity of the storage formation ranging from $0-1$ (Hellevang,

2015). After CO$_2$ is captured from power plants it is compressed to a super-critical fluid. It is important that the storage site has the proper temperature and pressure conditions to maintain this super-critical phase, if not, the CO$_2$ can change to gas phase and the CO$_2$ density (ρ_{CO_2}) is greatly reduced, which again further reduces the storage capacity.

$$m_{CO_2} = V_b \cdot \phi \cdot N/G \cdot \rho_{CO_2} \cdot \chi \tag{3.1}$$

3.1.2   Seal Integrity

Buoyancy forces CO$_2$ to migrate upwards in the sub surfaces, as it is less dense that then the saline water which occupies the pore space. A tight caprock with a trapping configuration is therefore needed to prevent the CO$_2$ to migrate up into the atmosphere (Shukla et al., 2010; Hellevang, 2015). These are classified in terms of structure and configuration, e.g. fault-, anticlinal- and stratigraphic traps (Bjørlykke, 2015b). Potential leakage risks for CO$_2$ are through the pore-throats of the caprock, or along fractures and fault planes. These leakage paths can be further enhanced from reactions between the minerals from the caprock and carbonic acid produced between the CO$_2$ and saline water (Hellevang, 2015).

3.1.3   Secondary Trapping Mechanisms

In addition to being structurally trapped by a caprock, CO$_2$ can over time be immobilized in the subsurface. These so called secondary trapping mechanisms are; residual-, solubility- and mineral trapping (Hellevang, 2015). Residual trapping occurs when CO$_2$ displaces formation water after injection and migration. Silica-clastic sediments are water wet, a thin film of water is present around the sedimentary grains, also after the CO$_2$ is injected and has displaces the formation water. Resulting in tiny bobbles of CO$_2$ being strapped in the pores after the CO$_2$ has passed and the buoyancy force is too small to enter the capillary force of the water film, blocking the pore-throats. When CO$_2$ reacts with water, the product is carbonic acid (Halland et al., 2011). As carbonic acid is denser then the formation water, it subsides and new formation water

is lifted up, further continuing the reaction. Mineral trapping occurs when carbonic acid reacts with metal cations such as; Me^{2+}, Mg^{2+} and Fe^{2+}, and forms carbonate minerals (Hellevang, 2015). These secondary trapping mechanisms will over time immobilize all the stored CO_2, this is roughly estimated to take 10 000 years (Metz et al., 2005).

3.2   Effects of burial, compaction and uplift

Properties of reservoir- and caprocks, including porosity, permeability, ductility, and pore pressure are important factors that govern storage capacity, phase behavior, and the potential for leakage in relation to CO_2 sequestration (Hellevang, 2015). These properties can be significantly perturbed by uplift and the burial of the target formations (Nygård et al., 2006). From burial, sediments undergo mechanical compaction which is driven by the effective pressure. This modifies the sediment by brittle fracturing, deforming, re-orientating, and frictional sliding of the grains (Bjørlykke and Jahren, 2010). At 70 ^{o}C ($\sim$ 2.5 km depth), chemical compaction becomes the primary mechanism of compaction, because high temperatures enable quartz cement dissolution and precipitation (Bjørlykke and Jahren, 2010).

Uplift induces tensile failure of sedimentary rocks (Doré et al., 1997; Nygård et al., 2006; Henriksen et al., 2011). These tensile fractures can significantly increase the permeability of sedimentary rocks and can allow for previously high pore pressure, if present, to re-equalize to hydrostatic, or drop to under-pressure (Doré and Jensen, 1996; Henriksen et al., 2011). It is recognized that the effects of burial and uplift is controlled by many external factors (Bjørlykke, 2015b). Generally, reservoir quality is reduced as a function of burial depth, whereas seal integrity increases (Doré and Jensen, 1996). Uplifted caprocks generally have a higher risk of leakage, on the other hand, reservoir quality increases in deeply buried uplifted rocks (Henriksen et al., 2011).

3.2.1   Diagenesis

Diagenesis is defined as the processes altering sediments from deposition to meta-morphism. It is mainly controlled by: (1) Provenance, transport mechanism, and depositional environment. These control mineralogy, sediment configuration and -distribution. (2) Near-surface diagenesis processes in open systems, where meteoric water flushing will keep the system in thermodynamic disequilibrium alternating the composition. (3) Mechanical compaction, where the main processes are crushing, deforming, sliding and re-orientating grains, which is a function of the composition, mineralogy, grains size, grain shape, sorting and portion, and it is controlled by the effective stress (Eq. 3.2). (4) Chemical compaction occurs due to diagenetic processes controlled by temperature, pressure, time and mineral composition (Walderhaug, 1996; Worden and Burley, 2003; Bjørlykke and Jahren, 2010).

3.2.1.1   Mechanical Compaction

From deposition to approximately 2.5 km depth, compaction is driven by effective stress (σ_e; Wq. 3.2), where σ_t is the total stress from the overburden, and P_p is the pore pressure (Bjørlykke and Jahren, 2010).

$$\sigma_e = \sigma_e - P_p \tag{3.2}$$

Causes of mechanical compaction are; crushing of brittle grains, deformation of ductile grains, sliding, and reorientation of grains (Bjørlykke and Jahren, 2010). Compaction curves alter for individual sediments compositions (example in the next paragraph), where controlling factors are; mineralogy, grain size, grain shape, sorting, and the distribution of sedimentary fraction (Fawad et al., 2011). Elastic properties of different mineralogy vary, determining if crushing or deformation of grains are favored. Larger grains have lesser grain-to-grain contact, resulting in less distribution of stress and more compaction. Likewise, angular grains fracture more easily than those that are well rounded (Fawad et al., 2011).

Mechanical compaction behavior fits well regarding soft sediments located in the lower

sections of sedimentary basins, however, the presence of shallow carbonates and chemical alternations can complicate predictions (Bjørlykke and Høeg, 1997). Mechanical compaction trends are vastly different for sandstones and mudstones. The critical porosity of clay minerals ranges from $0.6-0.8$, whereas the critical porosity of sands usually ranges from $0.38-0.5$. Figure 3.1 demonstrates how this is caused by the different shapes of the grains. In shallower sections, clay porosity is significantly reduced, caused by the collapse of the grain configuration to a more efficient packing. Sands compact more evenly except in the chemical compaction domain.
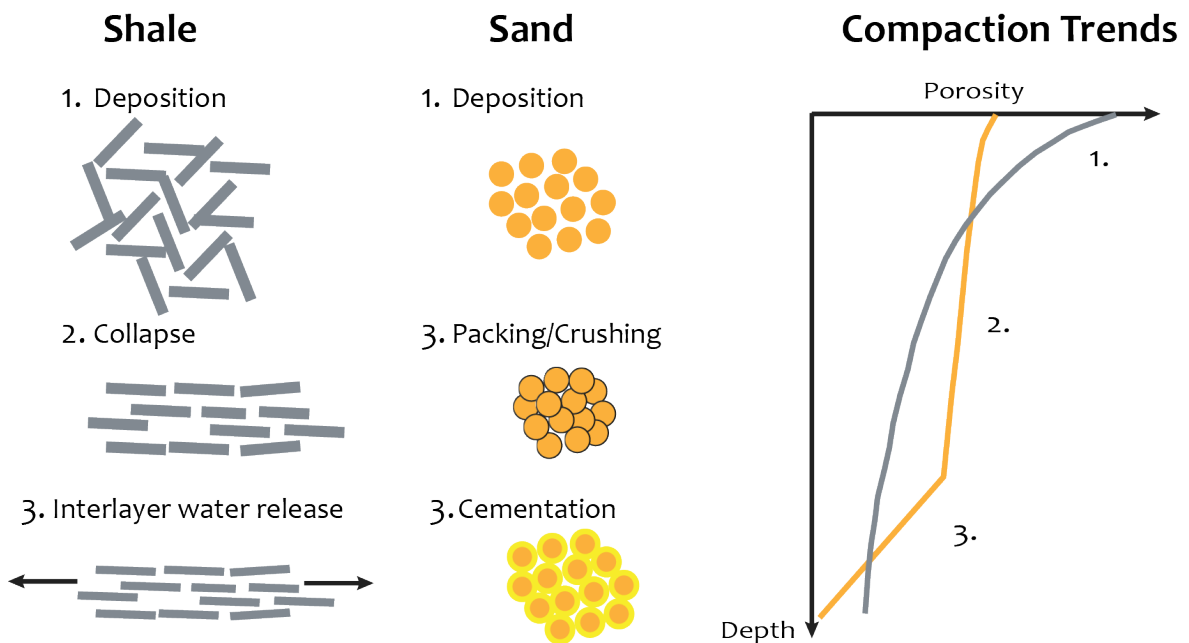
Figure 3.1. Cartoon demonstrating the difference in compaction behavior of shales and sands. Note the grain structure of the clay particles forms high initial porosity (1.), vs the sand which is more efficiently packed at deposition. Also, the kick in compaction, when sandstones enters the chemical compaction, from quartz cement dissolution and precipitation (3.). Adapted from Marion (1991).

3.2.1.2   Chemical Compaction

In temperatures above approximately 70 ^{o}C chemical alternation of minerals e.g. transformation of clay minerals and formation of stylolites occurs. Both resulting in precipitation (growth of crystals) of quartz cement onto fresh quartz grain surfaces. This is considered to be the primary contributor to porosity reduction in sandstones (Bjørlykke and Jahren, 2010). Walderhaug (1996) showed how the dissolution of quartz cement and the following porosity loss in quartzose sandstones can be simulated as a function of

temperature history. In progressively subsiding basins quartz cementation transforms sandstones to quartzite where the porosity is close to zero (Bjørlykke and Jahren, 2010). At intermediate depths the dissolution from stylolites stops if the pore-water gets supersaturated by silica. This occurs when there are no fresh grain surfaces available for precipitation. If burial continues, the confining pressure will induce grain fracturing and fresh quartz surfaces will become exposed again (Bjørlykke and Jahren, 2010).

Mudstones consolidates when skeleton structures of micro-quartz are precipitated locally within the mud (Thyberg et al., 2010). This observation has been related to the smectite to illite reaction, where silica is a bi-product and has been identified at approximately $80-85$ C^o (Thyberg et al., 2010). The reaction relies on the amount of potassium (K$^+$), which can dissolve from K-feldspar. In addition to silica dissolution, illite has a wool-like grain structure, which is permeability reducing by itself and causes a significant reduction in reservoir quality. Marcussen et al. (2010a) demonstrated how sensitive basin modeling is to clay mineralogy by analyzing compaction behavior of smectite and kaolinite. Where smectite has a higher porosity at shallower depths than kaolinite hence a higher compaction rate.

3.2.1.3 Porosity Preservation

As mentioned, effective stress drives the porosity reduction in the mechanical compaction domain. Effective stress decreases with increasing pore pressure (Eq. 3.2), which can occur from over-pressure and gas-emplacement. Early strengthening of the rock framework (e.g. calcite cementation) increases the rocks resistance to the overburden stress and reduces the mechanical compaction. In the chemical compaction domain precipitation of quartz cement only occurs at exposed quartz grain surfaces, if the grain is coated by e.g.; chlorite, illite, smectite, micro-quartz, or iron-oxides, precipitation is prevented (Fig. 3.2). At further burial, mechanical compaction can take place at abnormal depths because the rock framework is weakened (Oye et al., 2018).

3.2.2   From ductile to brittle behavior

Exposing unconsolidated sand- and mudstones to chemical compaction increases their brittle behavior (Doré et al., 2002; Bjørlykke and Jahren, 2010; Thyberg et al., 2010). This gradual transition is therefore controlled by depth and the geothermal gradient, but also the mineralogy and textural relationship. Without shallow carbonate cementation shales and sandstones may be only slightly cemented down to 2-3 km depth (Bjørlykke and Høeg, 1997). The chemical diagenesis is the driving force that embrittles the sediments (Doré et al., 2002).
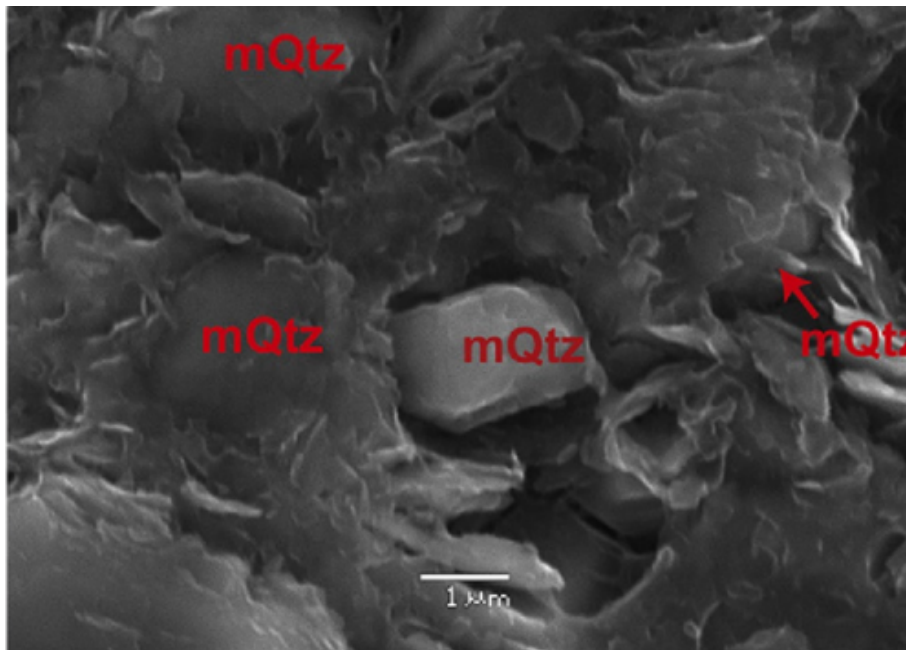
Figure 3.2. SEM picture of micro-quartz within a shale, where several micro-quartz are surrounded by clay minerals, from Thyberg et al. (2010). Micro-quartz is a product of chemical compaction. If they build a framework with in a shale, it makes it more brittle.

From tri-axial stress measurements, Nygård et al. (2006), found the brittle to ductile transition for several mudstones and they noticed that processes such as uplift, diagenesis, and over-pressure build-up make mudstones overconsolidated (Fig. 3.3). In this form, mudrocks respond in a more brittle manner to applied load and stress, which leads to fracture in a lower stress regime compared to in higher confining pressure scenarios (Nygård et al., 2006). Fractures may be induced to uplifted shales due to tectonic activity or from exposure to lateral variations in uplift and subsidence rates (Doré et al., 2002). For unconsolidated sediments, fractures will close without over-

19

pressure, and/or high effective pressure (Bjørlykke and Høeg, 1997). In deeply buried rocks the confining pressure is normally too high for fractures to stay open, this results in over-pressure build up and hydro-fracturing. Open fractures are time-limited features, where closing from either mechanical deformation or chemical compaction will occur (Bjørlykke and Høeg, 1997).
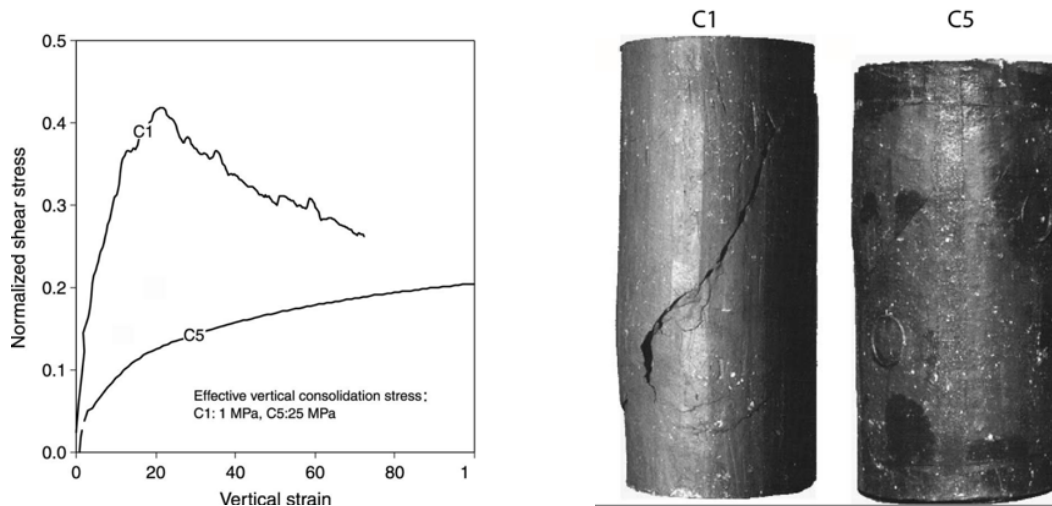
Figure 3.3. Tri-axial test on the same shale in different confining pressure scenarios. Left: Graph showing the stress-strain response from the two samples. Right: Picture of the samples after the test, showing the C1, exposed to lower confining pressure, has fractured (brittle deformation), whereas the C5 has shrunk. Modified from Nygård et al. (2006)

3.2.3   Implications for CO_2 Storage

Injection of CO_2 will induce compressional stress, chemical weathering, and initiation of fractures from changes in the stress field caused by injection pressure. The cap rock needs to withstand these factors for some thousands of years until all the CO_2 is precipitated as minerals and safely stored (Shukla et al., 2010).

As previously mentioned, shales become more compacted with increased burial. Hence, uplifted shales are tighter than normal compacted shales at equal depths. With higher tensile strength and reduced pore-throats these uplifted seals might be superior as CO_2 seals, compared to normally compacted once (Doré et al., 2002). However, if the shale has been embrittled before the uplift event, i.e. from micro-quartz precipitation, it will fracture more easily when exposed to stress (Doré et al., 2002). Whereas, if the shale has not been uplifted it's more likely to behave in a ductile fashion to applied

stress and not fracture, because the confining pressure is higher (Nygård et al., 2006). Uplifted seals generally have increased risk of leakage (Doré et al., 2002). Makurat et al. (1992) modeled fracture development for a caprock in the Barents Sea, and recognized that fractures are usually initiated in caprocks uplifted more than 1600 m. They also stressed that local lateral differences in uplift and subsidence can induce extensional fractures.

As reservoir quality decreases with burial, uplifted reservoir rocks will have lower primary porosity and permeability than expected (Doré et al., 2002). Deep burial might enhance reservoir quality from uplift events if the consolidated rock is fractured, and permeability increases. Sandstones down to $2000-2500$ m depth will behave in a ductile fashion during uplift. Interbedded low permeable shale beds acting as reservoir baffles can fracture, and connect vertically separated reservoir units (Ogata et al., 2014). If the system is closed and the framework does not deplete or fracture during uplift, under-pressure conditions are induced, risking super-critical stability of the CO_2. The ductility is generally significantly higher for shales than sandstones, so uplift of deeply buried storage systems might increase the reservoir quality without lowering the seal integrity, but it is dependent on the degree the rock has been cemented (Doré et al., 2002).

3.3   Quantitative Seismic Interpretation

Seismic reflection data has been used for a century now to study structures under the subsurface (Simm et al., 2014). The technology has evolved rapidly mainly due to commercial mapping for hydrocarbon exploration. In recent decades the seismic amplitudes sensitivity to parameters such as; lithology, porosity, fluid content and pore-pressure has become well defined and understood, and allows for quantitative interpretation of these parameters from the seismic data (Avseth et al., 2010). Techniques like; Amplitude vs Offset (AVO), impedance inversion and seismic forward modeling have made it possible to turn the seismic interface measurements to absolute interval properties (Simm et al., 2014).

Seismic data is acquired by emitting acoustic waves from a source into the subsurface. At hardness (*impedance*) contrasts in the earth's interior the waves get reflected back. These reflected waves are recorded by several receivers (Simm et al., 2014). Resolving the energy associated with these bed reflections (distinct from seismic noise e.g.; direct waves, multiples and ghosts) from raw seismic data requires seismic processing. The foremost step to enhance reflected energy and to minimize noise is stacking. Stacking refers of sorting the seismic traces with approximately the same reflection point into gathers. When these traces are stacked together, will the consistent trace to trace reflection signals be enhanced, whereas the random noise signals are reduced (Simm et al., 2014).

A simple and robust way of explaining the seismic trace is the *convolution model* (Eq. 3.3). Where t is time, $s(t)$ is the seismic trace, $R(t)$ is the earths reflection coefficient series, W is the source wavelet, $*$ is the convolution operator and $n(t)$ is noise (Russell, 1988).

$$s(t) = R(t) * W + n(t) \tag{3.3}$$

Hence, by assuming the noise has been removed in the data processing, the trace can be modeled by super-imposing each reflection coefficient convolved (scaled) with the wavelet. This is illustrated in Figure 3.4. Each reflection coefficient in $R(t)$ can be

estimated by Equation 3.4, after Russell (1988), where Z_i refers to the impedance of the bed above the reflection and Z_{i+1} to the bed below.

$$R_i = \frac{Z_{i+1} - Z_i}{Z_{i+1} + Z_i} \tag{3.4}$$

The wavelet can be thought of as a result of super-imposing sinuous waves of every frequency in the seismic band. Hence in theory, if all frequencies are recovered in the acquisition, the wavelet would be a perfect spike. In conventional seismic data the frequency band usually stretches from $10-80$ Hz limiting the vertical resolution (Simm et al., 2014). Assumptions regarding the convolution model that needs to be accessed are; (1) assumes all the noise is eliminated from the data processing, (2) non-offset incidence reflections and (3) a constant wavelet (Russell, 1988).

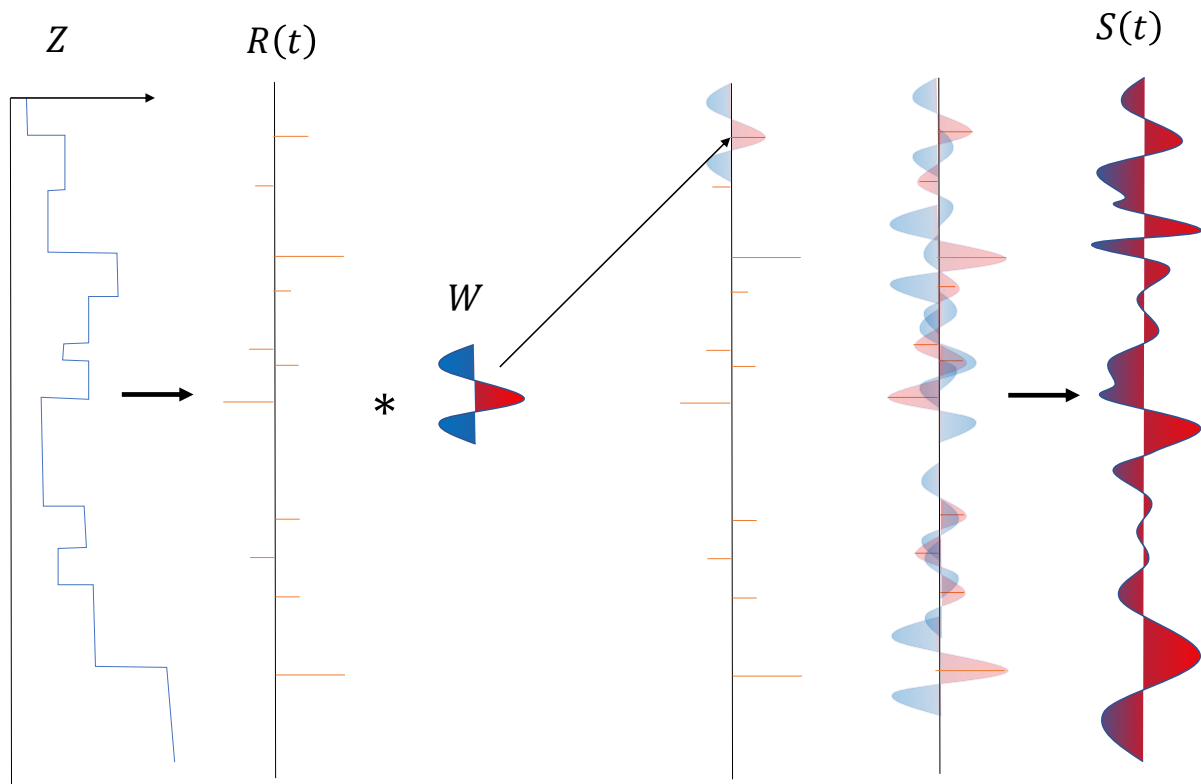**Figure 3.4.**   Illustration the demonstrates the basic idea of the convolution model. From left a blocky impedance log, transformed to a reflection coefficient series. Further, the wavelet is draped on each reflection coefficient and scaled by the reflection coefficients dimension. Finally, all the scaled wavelets are added together to a synthetic seismic trace. Re-drawn from Russell (1988)

3.3.1 Seismic Trace Inversion

The motivation for inverting seismic data is to extract rock property information masked in the amplitude data and increase the vertical resolution by removing the wavelet (Latimer et al., 2000). Early attempts of seismic inversion were performed by rearranging Equation 3.4 to Equation 3.5. However, as an effect of the band limitation in the seismic data and not accessing the wavelet, only wiggly shaped, relative impedance data was recovered. To remove the effects of the wavelet, attempts of *deconvolving* the seismic has been made (e.g. Russell 1988). These attempts have failed in recovering absolute impedance, due to the band limitation, where the low-frequencies are essential. To recover absolute impedance an external low-frequency source is needed e.g.; seismic velocities and/or impedance extracted from sonic and density logs. A *Low-Frequency Model* (LFM) can be constructed by guiding the low-frequency sources with interpreted horizons and faults (Simm et al., 2014).

$$Z_{i+1} = Z_i \left[\frac{1 + r_i}{1 - r_i} \right] \tag{3.5}$$

3.3.2 Wavelet Extraction

There are three main approaches for extracting the wavelet from the seismic data (from Gelius and Johansen 2010):

1. **Statistically**: Screening through each trace within a given window and auto-correlating.

2. **Well-seismic tie**: A reflection coefficient series is derived from a well log, then a least-square shaping filter is calculated by performing the convolution model.

3. **Deterministic**: Measuring the wavelet directly from the source.

The first approach is robust because it uses the entire seismic volume, but it struggles in recovering both the phase and polarity of the wavelet which must be assigned. From the second approach, both the phase and the polarity are obtained, but it is only

performed at the well location, and it is assumed that both the seismic data and well logs can be relied on.

3.3.3   Model-based Inversion

When the LFM and the wavelet is estimated, it can be merged with the relative impedance recovered from the bandlimited inversion to get the absolute impedance. A more common and robust algorithm is the Model-based inversion, introduced by Russell (1988). Absolute impedance is recovered by iteratively updating the LFM so that its synthetic seismic matches the original seismic. This is performed by extracting reflection coefficient series from the LFM, applying Equation 3.3, convolving each reflection coefficient with the extracted wavelet, and deriving the least-square error from the seismic trace. The error information is then used to update the LMF (Fig. 3.5).

There are infinite impedance solutions to any given seismic data. Hence, the inversion needs to be constrained. The LFM is one constraint, moreover, how much the LFM is allowed to be changed during the process can be controlled be either hard boundaries or soft constraints (Simm et al., 2014). For the hard boundaries, an upper and lower percentage value for how much the LFM model is allowed to change. Whereas for the soft boundaries, a factor is introduced weighing the errors produced from the synthetic data vs. the LFM, and the synthetic data vs. the seismic data.
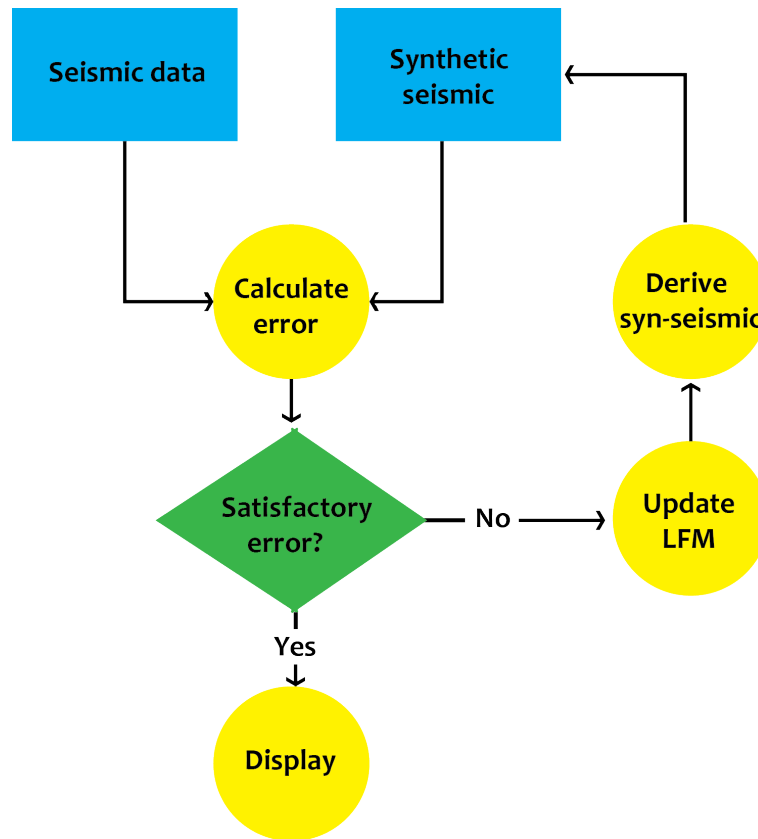
Figure 3.5. Workflow for the model based inversion algorithm. The process starts by deriving synthetic seismic from the LFM model and the calculate the least-square error between the synthetic and the seismic data. If the errors are to high, the LFM is updated. This loop iterates until the error is satisfactory. Adapted from Russell (1988).

3.3.4 Extended Elastic Impedance

Connolly (1999) introduced the concept of elastic impedance, with the motivation of generalizing impedance for all incidence angles (θ). The main application for this expression was to invert pre-stack data and to be able to calculate impedances from well-logs at different incidence angles which makes the method robust (Simm et al., 2014). One problem with this approach is that the dimensions of the calculations would vary with incidence angle, and not work when $\theta > 30^o$ (Connolly, 1999).

Whitcombe et al. (2002) introduced the Extended Elastic Impedance (EEI), which normalizes the elastic impedance to acoustic impedance dimensions. Also, by replacing the incidence angle $= \sin^2\theta$ with chi $= \tan^2\chi$ extends the range of the computable angle-interval from -90° to 90°. The χ-angle represents a rotation within the inter-

cept gradient cross-plot, relating to different projections of the cross-plot and has been shown to correlate well with different petrophysical properties effecting pre-stack seismic (Simm et al., 2014). By cross-correlating petrophysical logs of interest with EEI spectrum derived for all chi-angles, high correlation coefficients are associated with the similarity between the two (Whitcombe et al., 2002).

EEI-reflectivity corresponding to the impedance at a certain chi angle can be extracted from seismic pre-stack data (Whitcombe et al., 2002). There are several ways of performing this, e.g. an intercept and a gradient volume can be weighted by the chi angle of interest applying Equation 3.6. Where I is volume/section of the intercept value and G is the gradient of the pre-stack amplitude.

$$R(\chi) = I cos(\chi) + G sin(\chi) \tag{3.6}$$

With a LFM created from EEI-logs for the chi angle of interest, and a derived reflectivity weighted by the same chi angle, the model-based inversion scheme can be performed using the relation between the reflectivity and the EEI in Equation 3.7.

$$R(\chi) = \frac{EEI_{i+1} - EEI_i}{EEI_{i+1} + EEI_i} \tag{3.7}$$

3.3.5   Normal Velocity Trends (NVT)

In general, as sediments get compacted the porosity is reduced and the acoustic velocity increases as a result (Japsen, 1998). How the velocity changes with depth can be estimated for different sedimentary compositions, e.g. from lab experiments, analyzing wells penetrating normal compacted sediments, or calculated from porosity-depth trends. The motivation for deriving these trends is to identify deviations from the measured velocities. Negative deviations are assumed to indicate overpressure, and positive deviations uplift. Figure 3.6 demonstrates how measured velocities that deviates from the NVT can indicate uplift or overpressure (Japsen, 1998). Rock units that have been chemically compacted will give overprediction if an NVT based on mechanical compaction is used.
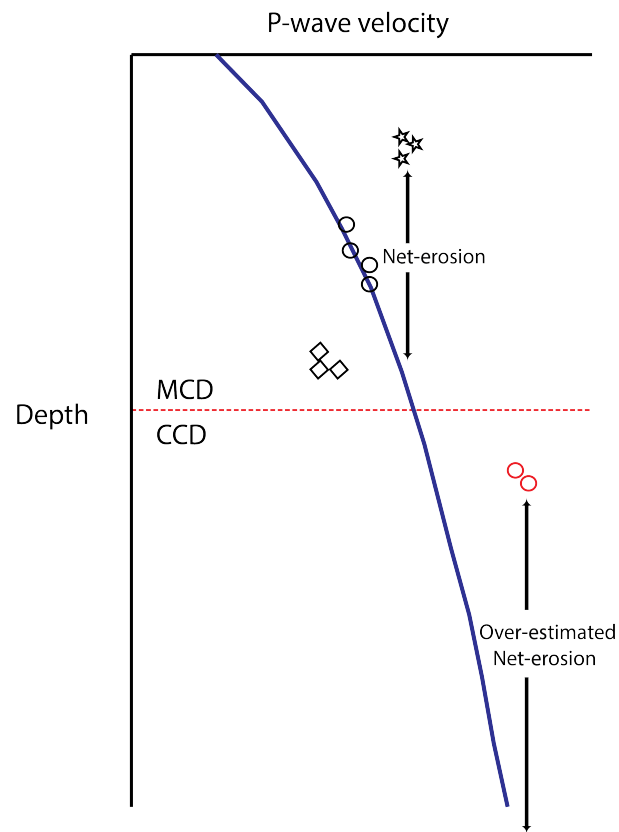
Figure 3.6.   Blue curve represents a velocity trend. Measured velocities that plot on top of the velocity trend indicate normal burial (black circles). Measurements below the trend (black diamonds) indicate overpressure or gas saturation, and measurements above indicates net-erosion. Note how sediments that have been chemically compacted well give overestimation in net-erosion, whereas the velocity trend only considers mechanically compacted sediments. Adapted from Japsen (1998).

Chapter 4

Data and Methods

The available data for this thesis is summarized in Table 4.1 and cover the area shown in Figure 4.1. The methods used and the workflow are summarized in Figure 4.2. The methods are separated into two sections; (1) seismic inversion and estimation of net-erosion, and (2) reconstruction modeling. Several software packages were utilized: Petrel 2018 (Schlumberger Ltd.) − for interpretation of both seismic and well log data. Hampson Russell (CGG Company) − for seismic inversion. Move^{TM} (Midland Valley) − for structural restoration and backstripping.

Table 4.1: Available data.

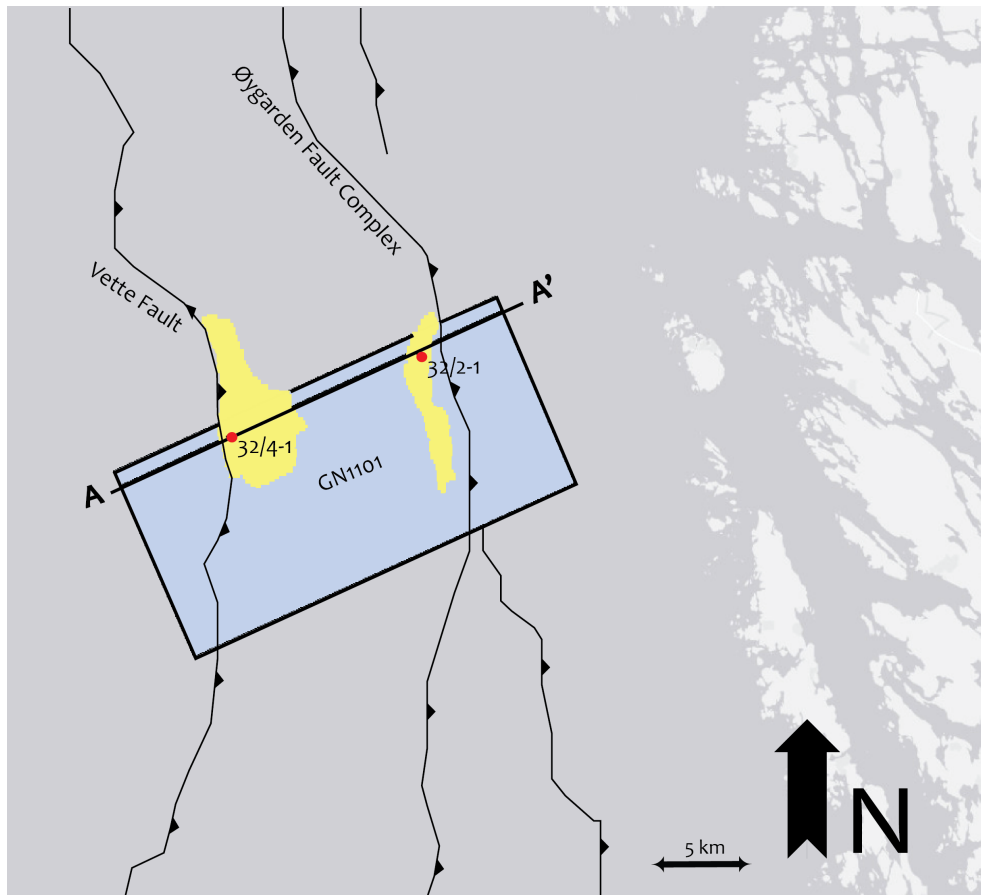| Data	Label	Acquired	Operator	Total depth
Seismic amplitude (post-stack)	GN1101	2011	Gassnova	5000 ms (TWT)
Seismic amplitude (pre-stack)	GN1101	2011	Gassnova	5000 ms (TWT)
Velocity Model (Stacking velocity)	GN1101	2011	Gassnova	5000 ms (TWT)
Well logs	32/2-1	2008	Talisman Energy	1300 m (TVD)
Well logs	32/4-1	1996	Phillips Petroleum	3158 m (TVD)

Figure 4.1. Map of the Smeaheia storage site and the available data. Note how the seismic data does not cover the entire extent of the simulated CO_2 plume (yellow polygon). Line A−A' corresponds to most of the figures in Chapter 5.
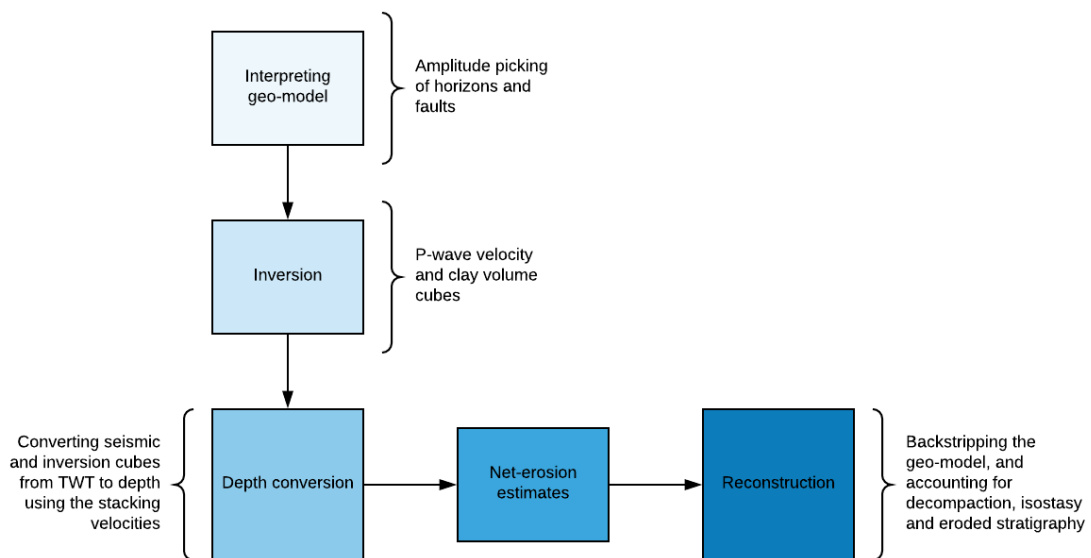
Figure 4.2. Rough, step by step, scheme of the methods used in this thesis. A brief description is also given for each step.

A raw seismic inline from the GN1101 cube is displayed in Figure 4.3. For most of the section the strong reflectors are clear, separated from each other, and continuous. To the east below approximately 500 milliseconds (ms) the data become chaotic. Resolution in general decreases with depth. The most dominant reflectors are peaks (black), indicating hard boundaries, except for top Draupne Formation.
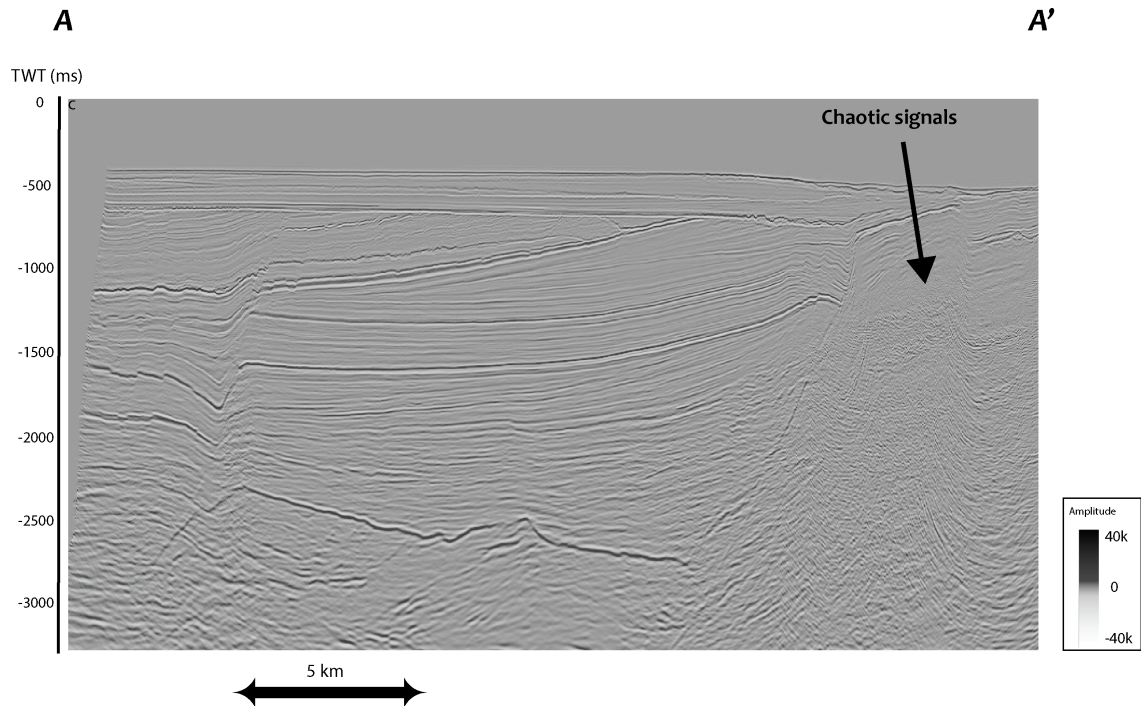
Figure 4.3. Inline from the GN1101 cube, not showing the entire depth. The data has normal polarity so black amplitudes values are associated with hard boundaries (peaks).

Velocity data from both interval velocities (from stacking velocities) and well log data are compared in Figure 4.4. The velocities from well 32/2-1 and the interval velocities show a fairly good correlation. Whereas a poorer correlation is observed between well 32/4-1 and the velocity model. The caliper log indicates collapse of the borehole corresponding to the misfit intervals (Fig. 4.8). Velocities within the Sognefjord Formation is higher in well 32/4-1 compared to well 32/2-1. In the interval velocity model it is similar, hence the velocities are increasing laterally to the east.
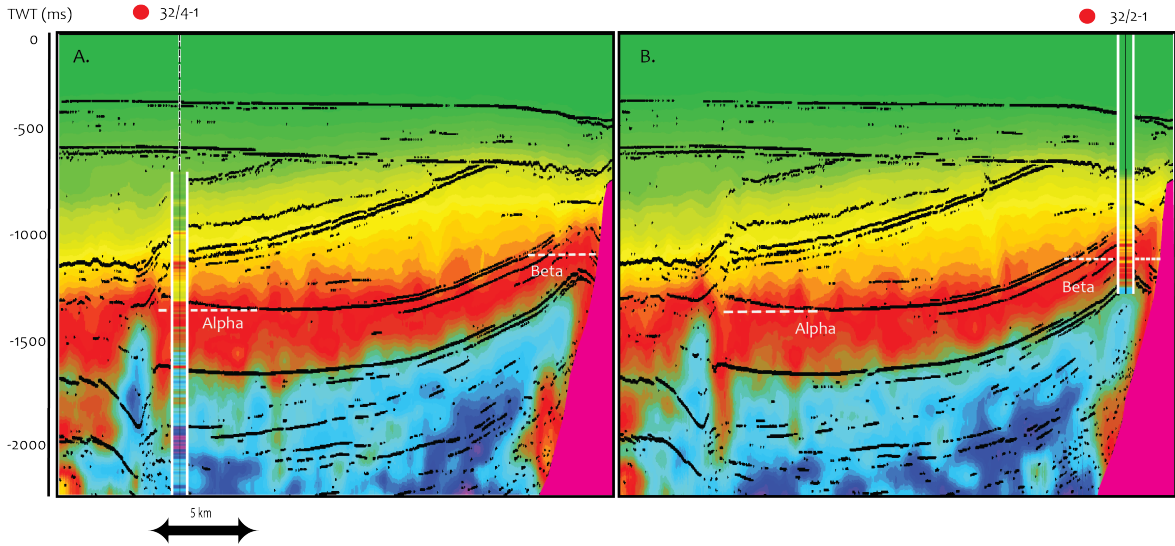
Figure 4.4. Comparison of P-wave logs and the interval velocity model (from stacking velocity). Each in-line (A and B) corresponds to the location of the wells. The black lines are the major peak reflectors from the seismic.

4.1 Seismic Inversion and Net-Erosion Estimation

4.1.0.1 P-wave Inversion Methodology

Because of the observed uncertainties and the sparse well control, the well logs are excluded from the Low-frequency Model (LFM). They are rather used for quality checking the inversion results. The LFM is obtained by transforming the stacking velocity volume to interval velocities, which was obtained using the Dix equation (Dix 1955). Then, applying Gardner's relation to estimate impedance (Gardner et al., 1974), from where synthetic seismic can be derived.

The seismic wavelet was extracted statistically from the seismic data in a search window between 500 and 2000 ms (Fig. 4.5 A.). Prior to the extraction, the software parameters were modified so that the wavelet was in zero phase with normal polarity and lasted for 200 ms. There is a frequency gap from approximately $4-12$ Hz between the seismic data and the stacking velocities (Fig. 4.5 B.). As a consequence, the inversion result has the corresponding uncertainties in absolute values.

To constrain the inversion, upper and lower boundaries were set allowing the impedance

values of the LFM to change by ± 100 % (Tab. 4.2). The inversion ran for 50 iterations, giving a satisfactory error between the impedance data and the seismic.

A.

B.
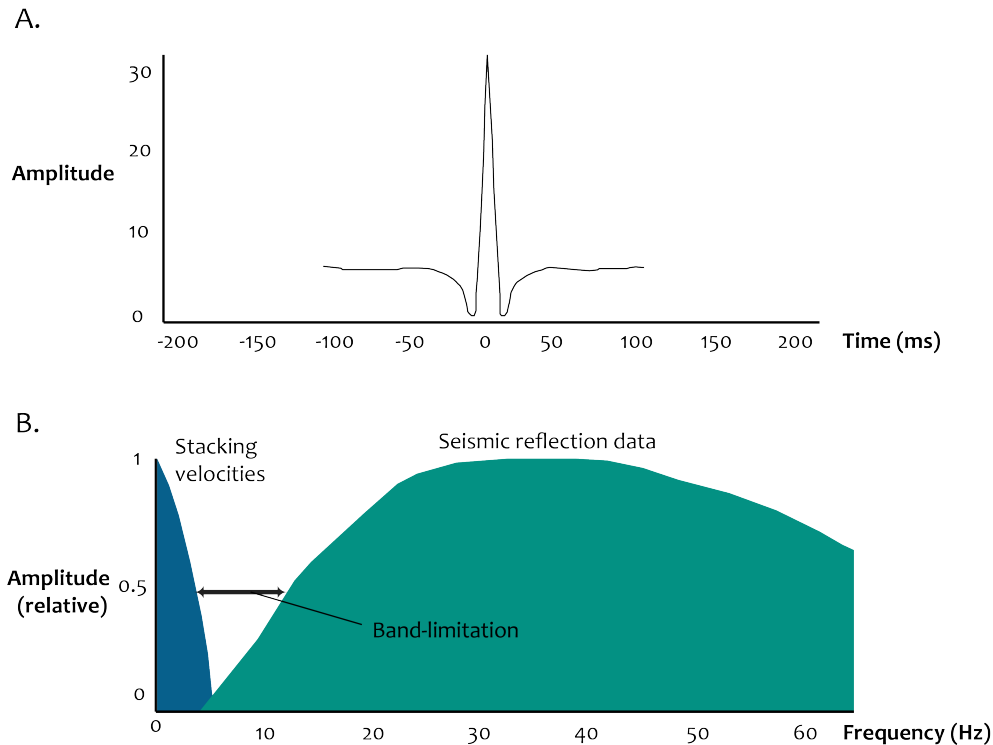
Figure 4.5.   A. Shows the estimated wavelet in time domain and B. the frequency band for both the seismic data and the stacking velocities. Note in B. where amplitudes are greater than 0.5 these is a frequency gap between the two datasets.

4.1.0.2   Volume of Clay Inversion Methodology

The Extended Elastic Impedance (EEI) spectrum was correlated with the V_{cl} log, which was derived from the Gamma Ray (GR) log. This gave a satisfying correlation value of 0.78. Figure 4.6 compares the estimated EEI log at 30° and the original V_{cl} log. From the pre-stack data both intercept and gradient volumes were created. From these, a seismic volume corresponding to the impedance at the same chi angel were calculated. A LFM was then constructed guiding the impedance values with interpreted horizons throughout the seismic volume. With the LFM and the representative scaled seismic, the same scheme as the model-based post-stack inversion algorithm was followed to invert for both V_{cl}.

Table 4.2: Parameters used for reconstruction modelling include fraction of sand and shale, sediment grain density, porosity depth coefficient and critical porosity.

Inversion Parameters	Input
Constraints option	Hard constraints
Max. impedance change (upper)	100 %
Max. impedance change (lower)	100 %
Average block size	3 ms
Pre-whitening factor	1 %
Iterations	50
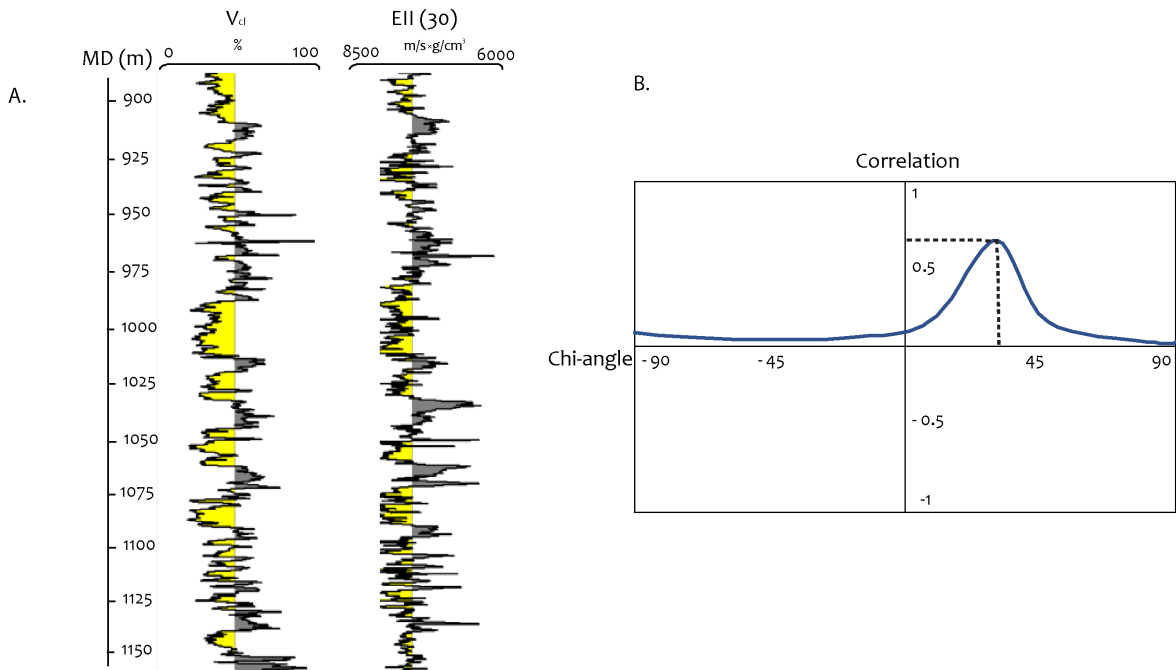
Figure 4.6. A. Comparison of derived V_{cl} log (left) and EEI log calculated at $\chi = 30^o$ (right), note the good match between the longer wavelength trends. Yellow and grey intervals indicate sand and shale units, respectively. B. Cross correlation with derived EEI logs for all the chi-angles -90 to 90 degrees. Best correlation occurs at 30 degrees with an 78% correlation.

The workflow for quantifying the net-erosion is illustrated in Figure 4.7. Clean sand units (less than 5 %) are filtered out 15 m below the PU. The velocity is extracted from the sand units and compared with a normal velocity for clean, mechanically compacted sands (Eq. 4.1; from Marcussen et al. 2010b; Equation 4.1 was not published in the paper, but estimated from the results). By solving the equation for the depth and

subtracting the depth from where the velocities are measured, dense estimates of net-erosion are obtained. These measurements were then gridded on to the PU surface, and a low-frequency filter was applied to eliminated anomalies. These anomalies can be e.g.; carbonates, calcite-cemented- and overpressured sands. The net-erosion values were then added to the surfaces depth values, resulting in a surface of the estimated eroded stratigraphy.
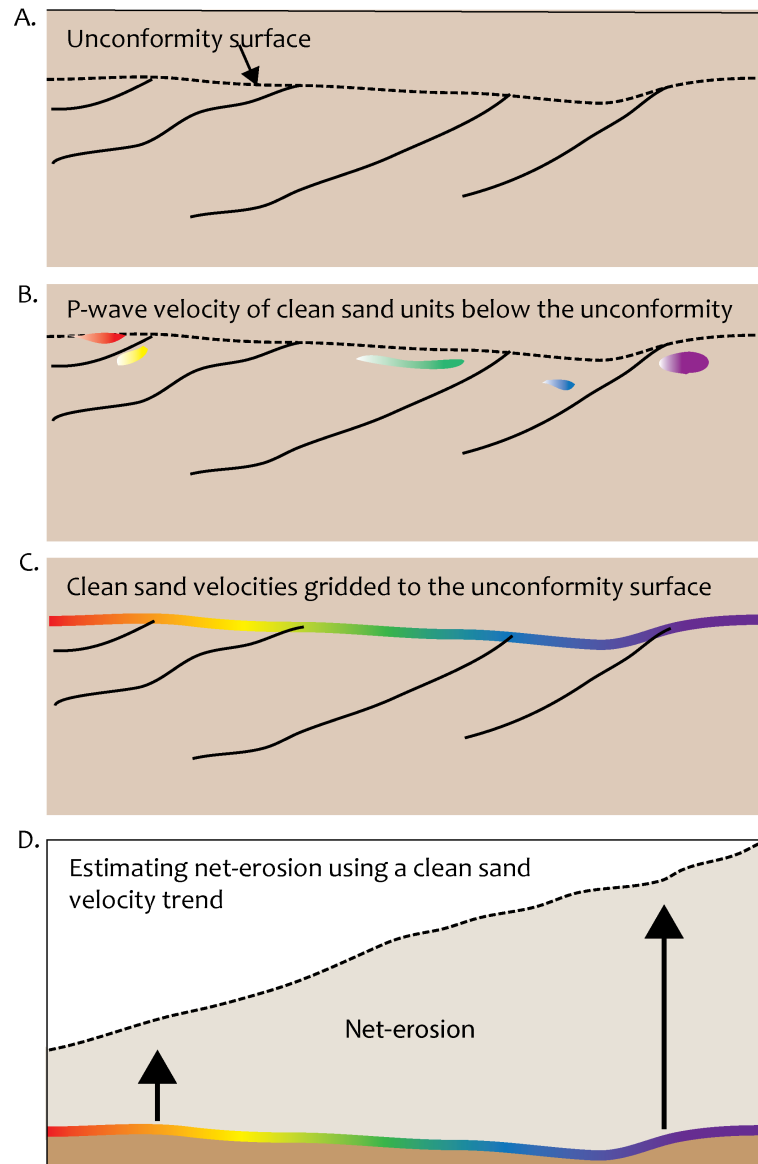
Figure 4.7. Illustrating the workflow for quantifying net-erosion: A. Finding sands from a lithology cube. B. filtering out the units with less than 5% shale. C. extracting the velocity to the sand units. D. Interpolating the velocity patches on to the surface of interest, then smoothing the surface attribute with a low-frequency filter. E. Solving for net-erosion using an NVT for sand, and adding these measurements to the depth values of the surface.

$$V_{p(Cleacsands)} = 1520 + 0.56z \tag{4.1}$$

4.2   Reconstruction Modeling

2D backstripping is a technique for modeling the geological evolution of cross-sections from a sedimentary basin by sequentially stripping of formations and restoring structural deformation. After a formation is stripped off, the algorithm accounts for thermal subsidence, decompaction of older formations and the lithospheres isostatic rebound. Move^{TM} has built-in algorithms that handle these processes. In addition, eroded stratigraphy is restored back based on the net-uplift estimated. The stratigraphy is then moved back to the recorded paleo-bathymetry. By performing these steps and recording and plotting the depth values for the formations of interest through each step, the uplift and subsidence history is estimated.

Move^{TM} assigns default gross lithological properties depending on the compositional description input. Each formation was assigned a lithology composition from silica clastic sediments, i.e. sand vs. shale (Fig. 4.8). Parameters include initial porosity, porosity decay constant, and sediment grain density (Tab. 4.3). The processes that are included in the reconstruction are:
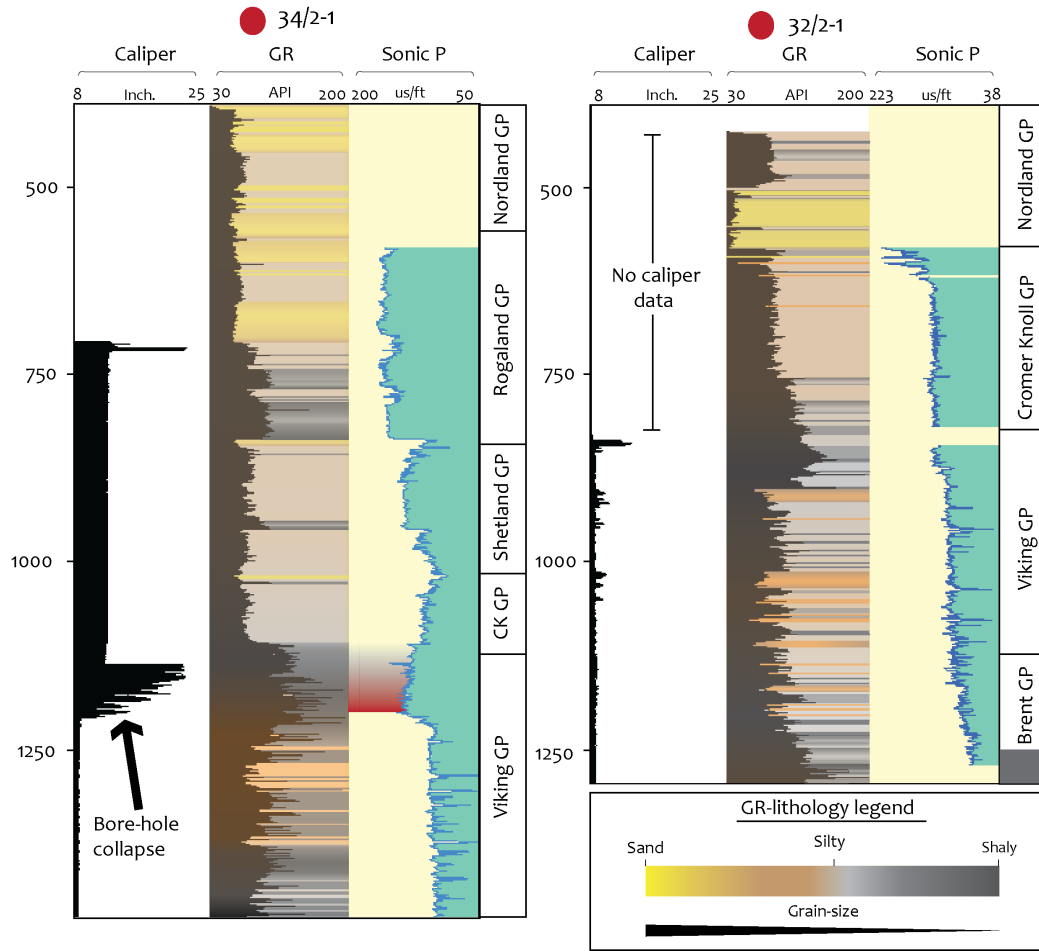
Figure 4.8. Lithology interpretation based on the GR log from each well. This interpretation is utilized to get the reconstruction parameters in Table 4.3. Collapse in in the bore-holes are observed frequently in each well limiting the certainty of the logs. Note the wide collapse in well 32/4-1 corresponding with a drop in velocity (marked din red).

1. **Thermal subsidence**: The algorithm accounting for thermal subsidence in Move^{TM} is based on the work by McKenzie (1978). When the lithosphere is thinned from rifting, hot mantle rises up to form equilibrium. Gradually, the denser rheology cools, resulting in subsidence of the lithosphere.

2. **Decompaction**: As outlined in Chapter 3., sediment porosity decreases as a function of burial depth. When the porosity is reduced, the entire formation volume also decreases, resulting in subsidence. This effect is allowed for in Move^{TM} by implementing Equation 4.2 based on Sclater and Christie (1980):

$$\phi = \phi_0 e^{-cz} \tag{4.2}$$

3. **Isostasy**: By loading or unloading sediments, water or ice, the lithospheres isostatic response is to sink or rise, respectively. Isostasy is therefore important to account for while performing backstripping, as it effects both the restored shapes of horizons and faults. Airy isostasy is used in this thesis, which assumes only local vertical movement. Lateral flexural isostatic readjustment is not accounted for here, because the model is too small to capture this effect.

Table 4.3: Parameters used for reconstruction modeling including; the fraction of sand and shale, sediment grain density(ρ), porosity depth coefficient (C), and the initial porosity (ϕ_o). S = Sognefjord Formation, F = Fennsfjord Formation, K = Krossfjord Formation and H = Heater Formation.

Formation/Group	Sand (frac.)	Shale (frac.)	ρ (g/cm^3)	C (1/km^{-1})	ϕ_o (frac.)
Nordland	0.87	0.13	2.65	0.30	0.51
Sele	0.33	0.67	2.69	0.43	0.58
Lista	0.30	0.70	2.67	0.44	0.59
Shetland	0.82	0.18	2.66	0.31	0.52
Cromer Knoll	0.20	0.80	2.71	0.46	0.60
Draupne	0.10	0.90	2.71	0.49	0.62
S, F, K and H	0.55	0.45	2.68	0.38	0.55
Brent	0.50	0.50	2.69	0.39	0.56
Permor-Triassic	0.50	0.50	2.69	0.39	0.56

4.2.1 Backstripping Constraints

After inserting the eroded sediments, the model needs to be moved to a paleo-marker/surface. Paleobathymetry estimates are such markers and have in recent times been estimated in 3D for the main periods in the northern North Sea (e.g. Roberts et al. 2019). Paleobathymetry for Neogene sediments in the Horda Platform area has not been estimated. Therefore, the most recent paleobathymetry data, from the Eocene, has been used for the Neogene as well.

4.3   Methodological Limitations and Uncertainties

4.3.1   Net-erosion Estimation

The net-erosion estimates above the PU impact the following reconstructed maximum burial depths and net-uplifts for the storage site. Therefore, it is critical to access how genuine the net-erosion result is. There are three factors impacting the net-erosion estimates; (1) the absolute values of the inverted V_p data, (2) that actual clean sand units have been successfully extracted from the EEI volume, and (3) that the velocity trend used to estimate net-erosion is representative for clean sands.

4.3.1.1   Absolute Velocities

Since the well logs were excluded from the LFM, the V_p inversion result is potentially affected by the missing frequency gap between the seismic data and stacking velocity model, from $4-12$ Hz. This affect is demonstrated in Figure 4.9, where a high frequency cut filter is applied to the sonic log at 4 HZ (red) and 12 HZ (blue). Notice the mid-frequency trend the red curve is lacking. These intermediate velocities add uncertainties to the absolute V_p results. V_p from the 32/2-1 well is generally lower than the stacking velocity model at the same location. Well logs are commonly considered to be more robust than seismic velocities, however, observed frequent collapse of the bore-hole (Fig. 4.8) introduces uncertainties to the well log data as well.
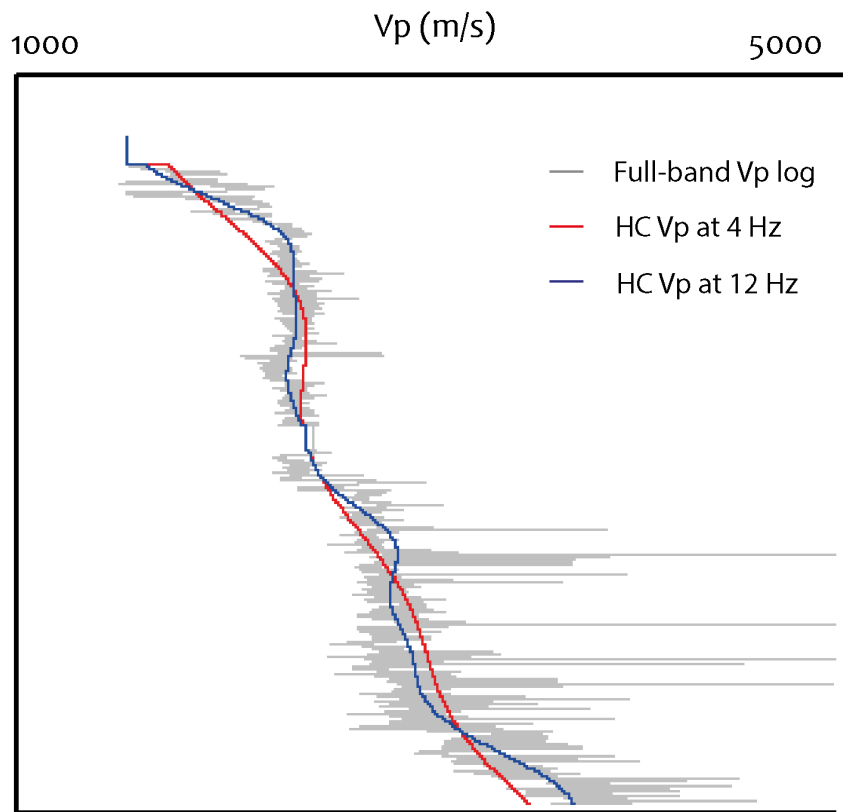
Figure 4.9. High cut frequency filters, 4 (red) and 12 Hz (blue) applied to the Vp log, visualizing the effect of the frequency gap between the seismic data and the stacking velocity model. Note how the blue curve captures intermediate velocity trends. Similar trends will be missing in the seismic inversion results as a result of the band-limitation (Fig. 4.5).

4.3.1.2 Clean Sandstone Extraction

The correlation between the EEI log calculated with $\chi = 30^o$ and the V_{cl} was 0.78. This factor alone gives a 28 percent uncertainty for the V_{cl} inversion result. Also, the V_{cl} has been derived from the GR log, where low radioactivity measurements are not directly related to sand intervals, but an indication of the presence of sand. Hence, lithologies as carbonate and chalks, which gives similar GR readings as sand, is most likely interpreted as sand as well. If the velocity of these lithologies are compared to a velocity trend for clean sand, the net-erosion estimates will be wrong. Furthermore, the LFM is only constructed using data from one well log (32/2-1), which again is extrapolated using the interpreted horizons. Thereby, the LF trends for the entire volume are not that robust.

4.3.1.3   Velocity Trends

Fawad et al. (2011) demonstrates how the textural configuration of sands, such as; grain size, sorting and shape, effects the resulting mechanical compaction signature. Thus, even if clean sand units are successfully extracted from the EEI data, the sands textural compositions gives a range of different velocity trends. The quantification of this uncertainty has not been performed.

4.3.2   Lack of Data Coverage

Since the data only covers a smaller part of the flank of the basin, important features such as the interior graben and younger stratigraphy are not included in the modeling. This leads to a poorer constrained model, as it is not accounting for the thermal subsidence and flexural subsidence from the Viking Graben, and partitioning of the younger succession to the west.

Chapter 5

Results

5.1 Seismic Interpretation

5.1.0.1 Description

Sedimentary packages have been mapped by correlating seismic reflectors with well tops (Fig. 5.1). Three prominent reflectors have been mapped, that either truncate reflectors below or are onlapped by reflectors above. These reflectors represent the Pleistocene Unconformity (PU), Mid. Cretaceous Unconformity (MCU) and Base Cretaceous Unconformity (BCU). The sedimentary package observed on top of the basement high (Fig. 5.1) is not age constrained and is speculatively interpreted as late Jurassic. The formations below the PU are characterized by westwards dipping reflectors. Figure 5.2 shows the ages of the formations sub-cropping the Quaternary package, which increase from west to east. Two major faults are observed and are interpreted as, from west to east; the Vette and Øygarden Fault (Whipp et al., 2014). Both faults can be tracked from the acoustic basement to the PU. No fault displacement is observed in the Quaternary package.

The Quaternary package pinches out to the east above the basement high, whereas to the west its thickness is constant. The Upper Cretaceous package is seemingly onlapping the Lower Cretaceous reflector. The Lower Cretaceous package can be divided in two, above and below the MCU (Fig. 5.3). Reflectors within the package below the

MCU terminate, whereas reflectors within the package above the MCU onlap. The pre MCU Lower Cretaceous package pinches out towards both the western and eastern crest of the fault block. Moreover, the thickness of the Jurassic packages is fairly even, thickening slightly westwards from the Øygarden and to the Vette Fault. At the western fault crest, the reflectors within the Draupne Formation terminate and are in contact with Upper Cretaceous sediments (the BCU). The package interpreted to be of Permo-Triassic age thickens significantly towards the Øygarden Fault. On the hanging wall of both faults, reflectors from top Triassic to top Draupne, have a folded anticlinal shape.

5.1.0.2   Interpretation

The westwards dip of the sub PU formations and the eastwards increase in age reflects a major tilting event with increasing uplift to the east. The tilting is credited to the Cenozoic uplift of southern Norway (Doré and Jensen, 1996; Riis, 1996; Lidmar-Bergström et al., 2000; Japsen and Chalmers, 2000; Anell et al., 2009). Early Cretaceous tilting is also evident seeing that the Upper Cretaceous package appears to onlap the Lower Cretaceous package, however, this interpretation is only valid when assuming the Lower Cretaceous package was flat in the early Cretaceous, which some authors believe to be the case (e.g. Lidmar-Bergström et al. 2000). Reactivation of the Øygarden and Vette Fault is interpreted to have occurred in the early Cretaceous, from erosion of Lower Cretaceous pre-rift strata and by the syn-rift wedge. During faulting, the roll-over structure is interpreted to have developed in the same manner as similar structures in the Barents Sea (e.g. the Goliat Field; Mulrooney et al. 2017). As a result of both the fault block rotation, and roll-over development, the western and the eastern crests of the fault block are interpreted to have been uplifted and eroded, which is reflected in the thickness distribution of the Lower Cretaceous pre-rift strata. Further, as faulting continued, accommodation space was formed and deposition of the Lower Cretaceous syn-rift strata took place. Considering the seemingly consistent thickness of the Upper Jurassic package, this strata is interpreted to be pre-rift. The reason the Jurassic package thickens slightly to the west, from Øygarden to Vette, similar observation is seen west of Vette, and is speculated to be effects of the differential compaction.
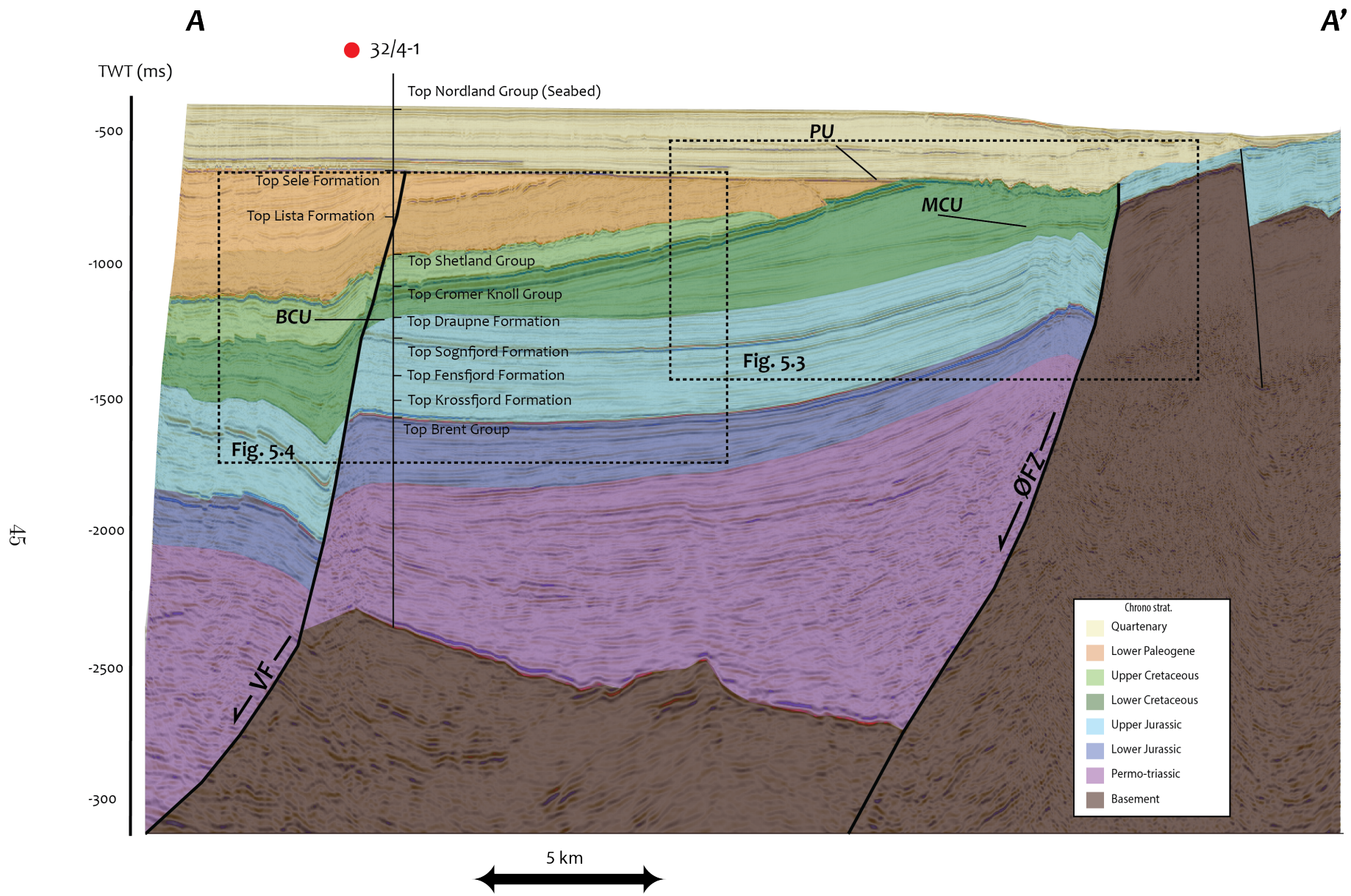
Figure 5.1. Cronostrategraphic interpretation of the seismic reflectors whose correlated with well tops.
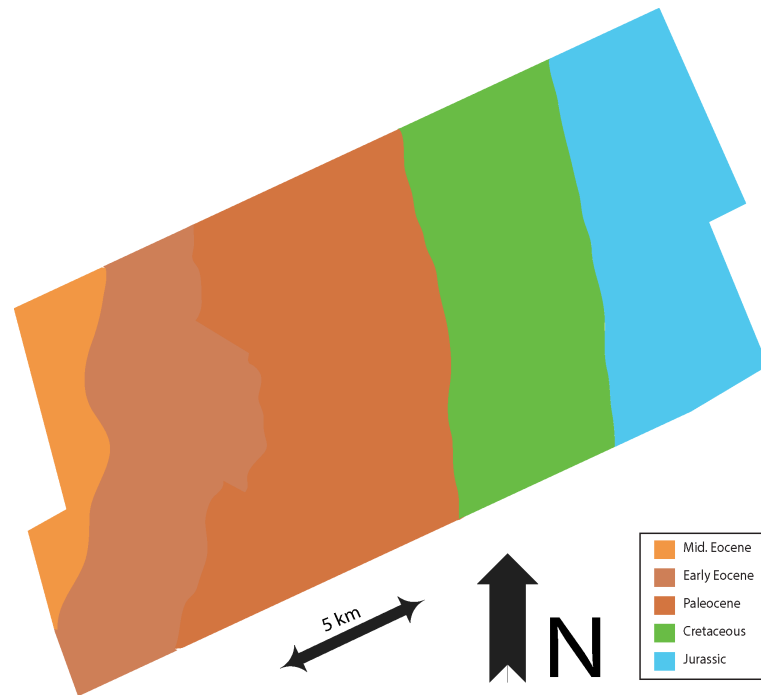
Figure 5.2. Stratigraphy just below the Pleistocene angular unconformity. showing that eastward progressively older sediments are in direct contact with the Quaternary sediments above the unconformity.
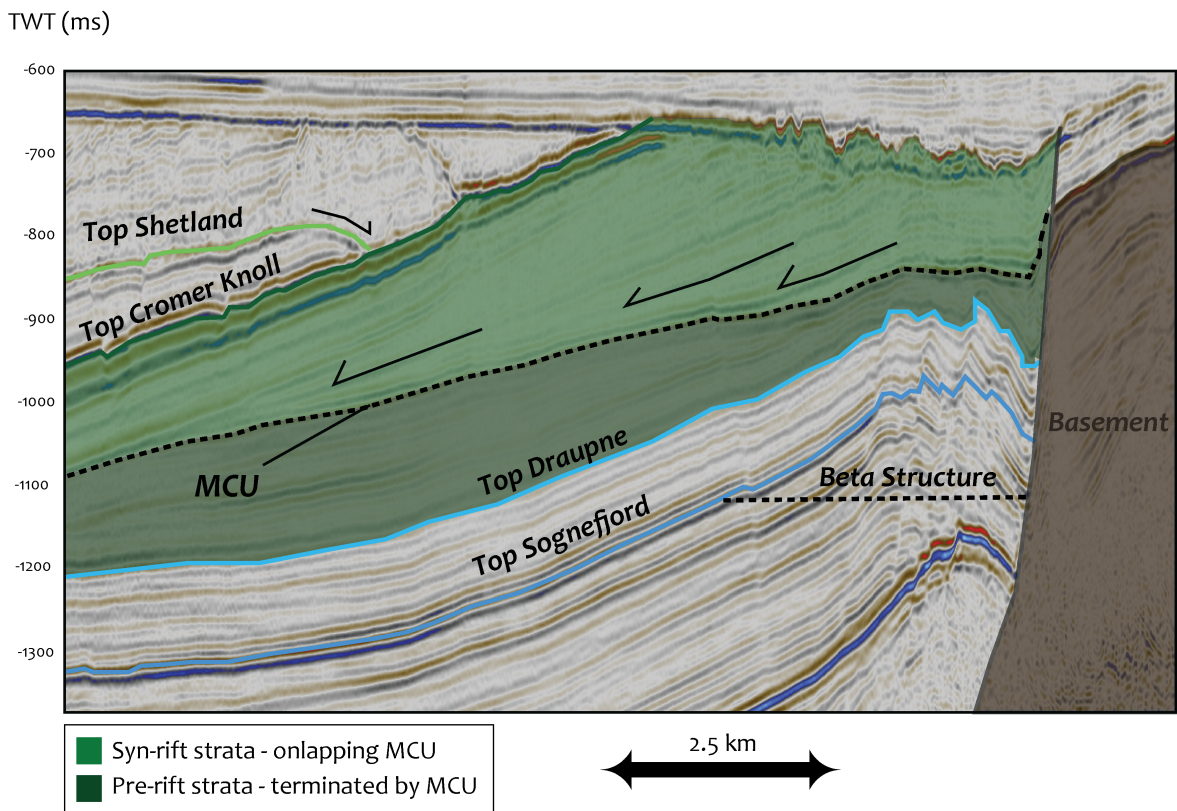
Figure 5.3. Seismic interpretation of pin-pointing the transition from pre- to syn-rift sedimentation. Note the correlation with the rollover forming the Beta Structure and the pinch-out of the Lower Cretaceous pre-rift strata. See Figure 5.1 for location.

46

TWT (ms)
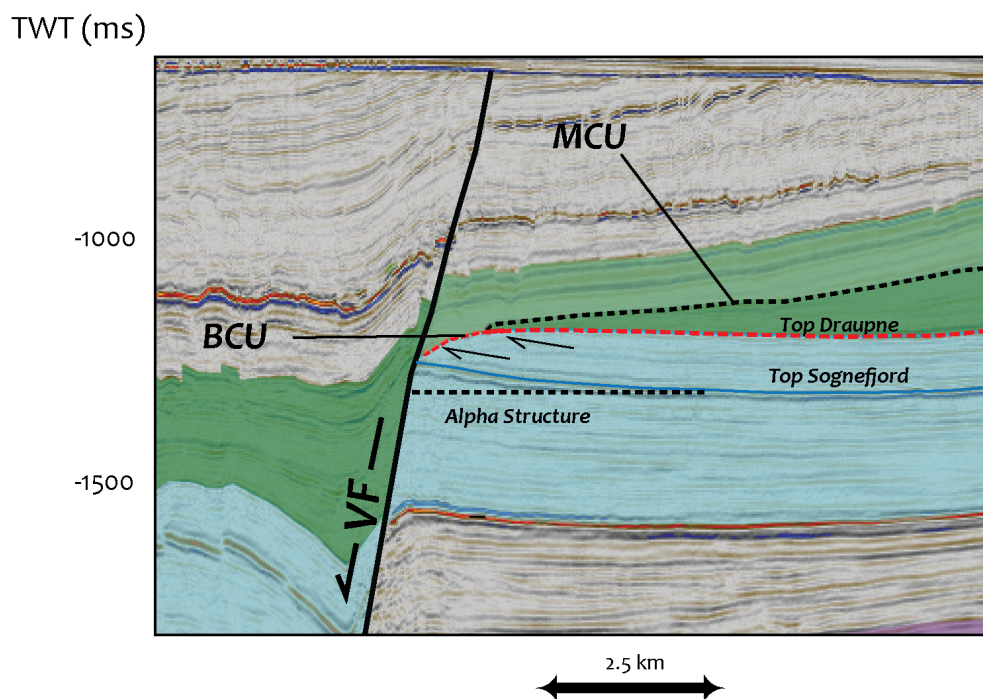
Figure 5.4. Interpretation of the fault block crest. The Lower Cretaceous pre-rift strata is also pinching out, over the Alpha Structure. Here, the Upper Cretaceous strata is in contact with Upper Jurassic. Terminations of the reflectors within the Draupne Formation, beneath the BCU.

5.1.1 Depth conversion

The GN1101 3D seismic survey was depth converted using stacking velocities provided by Gassnova (Fig. 5.5). As a quality control, the resulting depth converted data was compared to the well tops, mainly to assess the quality of the stacking velocities. Down to 800 m the correlation is fairly good, but gets exponentially poorer with depth. The depth difference was used to approximate the corresponding error in the stacking velocities. Within the depth interval (marked in orange) where velocities are later used to estimated net-erosion, the interval velocities are overestimated by 24 m/s and 178 m/s at well 32/4-1 and 32/2-1, respectively. The consequences of this are discussed in Chapter 6.
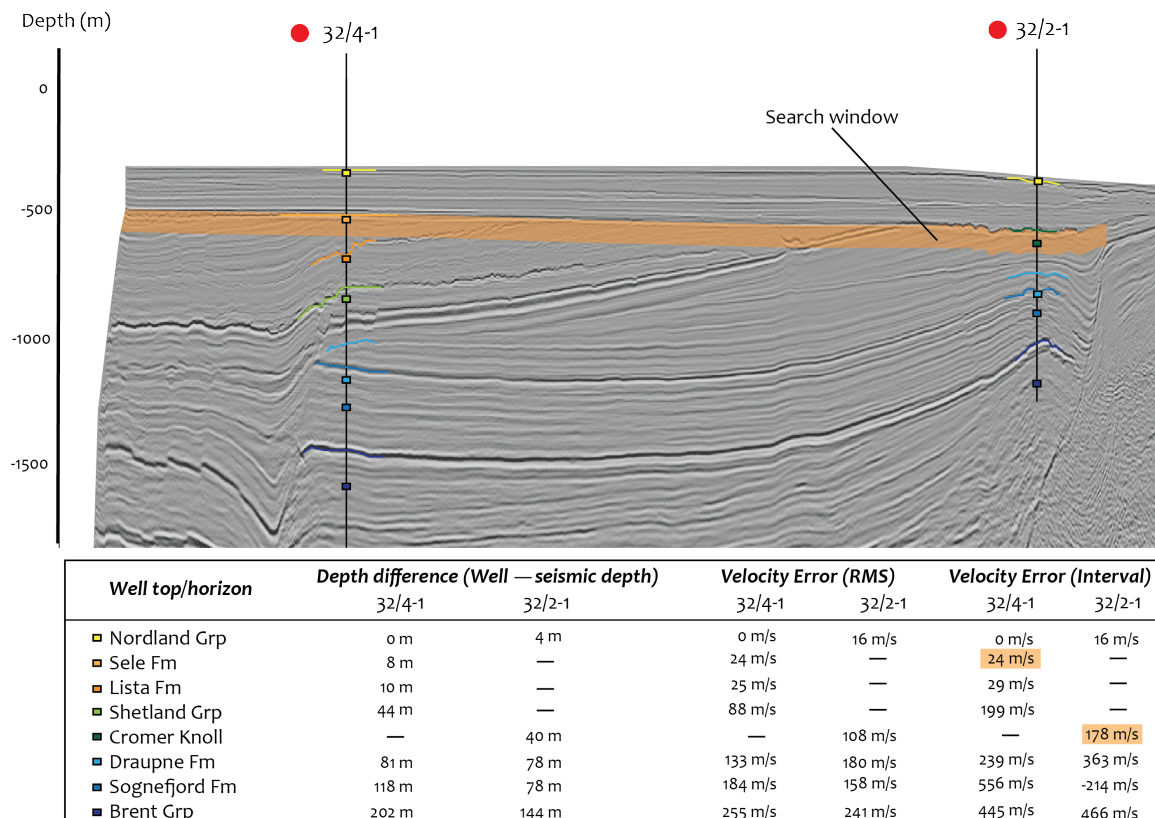
Figure 5.5. Comparison of depth converted seismic and well tops from both the wells. Note how the correlation gets poorer with depth. The difference in depth is summarized in the table below. The corresponding errors in velocity are also derived, for RMS and interval velocity, using the Dix equation. Orange area, both in the seismic and in the table, indicates the interval where the net-erosion measurements are performed.

| Well top/horizon	Depth difference (Well — seismic depth)		Velocity Error (RMS)		Velocity Error (Interval)	
	32/4-1	32/2-1	32/4-1	32/2-1	32/4-1	32/2-1
Nordland Grp	0 m	4 m	0 m/s	16 m/s	0 m/s	16 m/s
Sele Fm	8 m	—	24 m/s	—	24 m/s	—
Lista Fm	10 m	—	25 m/s	—	29 m/s	—
Shetland Grp	44 m	—	88 m/s	—	199 m/s	—
Cromer Knoll	—	40 m	—	108 m/s	—	178 m/s
Draupne Fm	81 m	78 m	133 m/s	180 m/s	239 m/s	363 m/s
Sognefjord Fm	118 m	78 m	184 m/s	158 m/s	556 m/s	-214 m/s
Brent Grp	202 m	144 m	255 m/s	241 m/s	445 m/s	466 m/s

5.2 Seismic Inversion and Net-erosion Estimates

5.2.1 P-wave Velocity Inversion

5.2.1.1 Description

Following the model-based inversion scheme, the LFM (Fig. 5.6) was iteratively updated so that the synthetic seismic and the original seismic within a satisfactory range of error. The resulting P-wave velocity (V_p) inversion is higher resolved than the LFM (Fig. 5.7), whereas, the same absolute velocity trends are similar. Above the BCU the velocities do not reach 3000 m/s, whereas for the Sognefjord Formation the velocities for some chunks extend 3000 m/s. The velocities below the PU laterally increase to

the east (Fig. 5.8).

5.2.1.2   Interpretation

The velocities shallower than the BCU does not reach 3000 m/s, which indicates that these sediments are only mechanically compacted (personal com. Nazmul Haque Mondol). Patches of velocities extend 3000 m/s within the Sognefjord Formation, which indicates that these sediments have become slightly chemically compacted or the presence of calcite cement. This implies that the sediments below the BCU cannot be used to estimate net-erosion by utilizing Eq. 4.1, which only applies to clean and mechanically compacted sands. As determined from seismic interpretation, the ages of the sub-cropping formations below the PU increase eastwards. From the V_p inversion it is apparent that the velocities increase laterally in the same manner. Based on these observations it is evident that these formations have been buried deeper, compacted more, later uplifted and eroded.
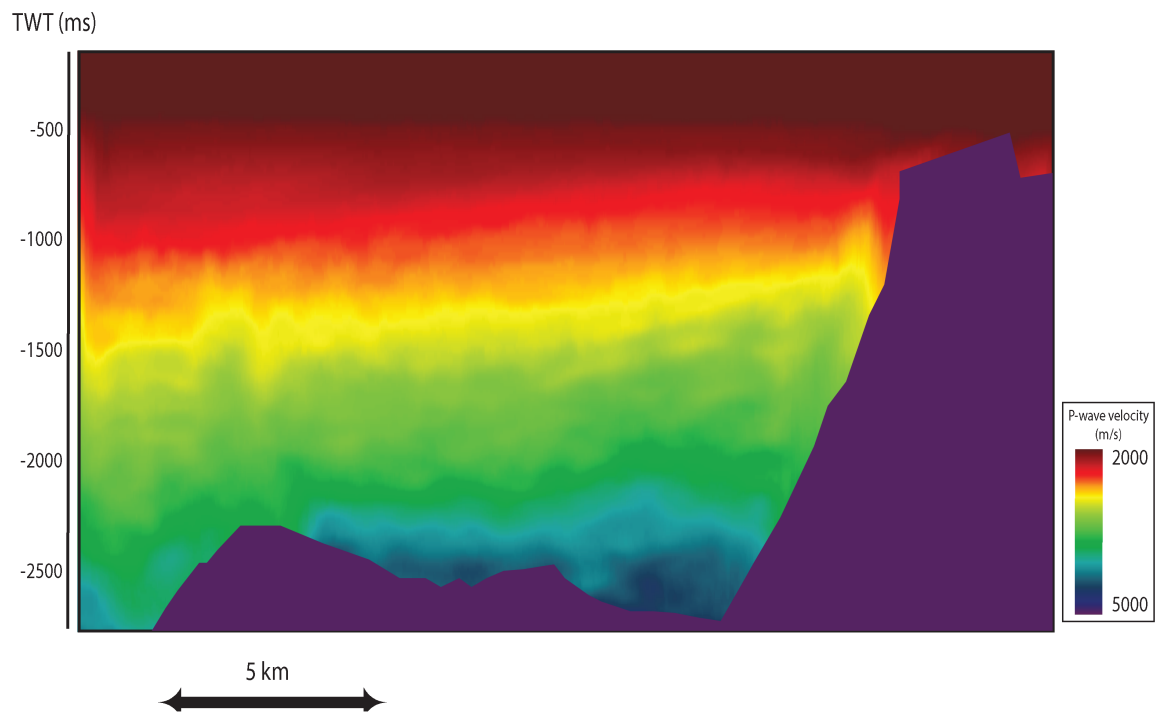
Figure 5.6.   LFM used as an initial model for the P-wave inversion, which results is displayed in Figure 5.7.
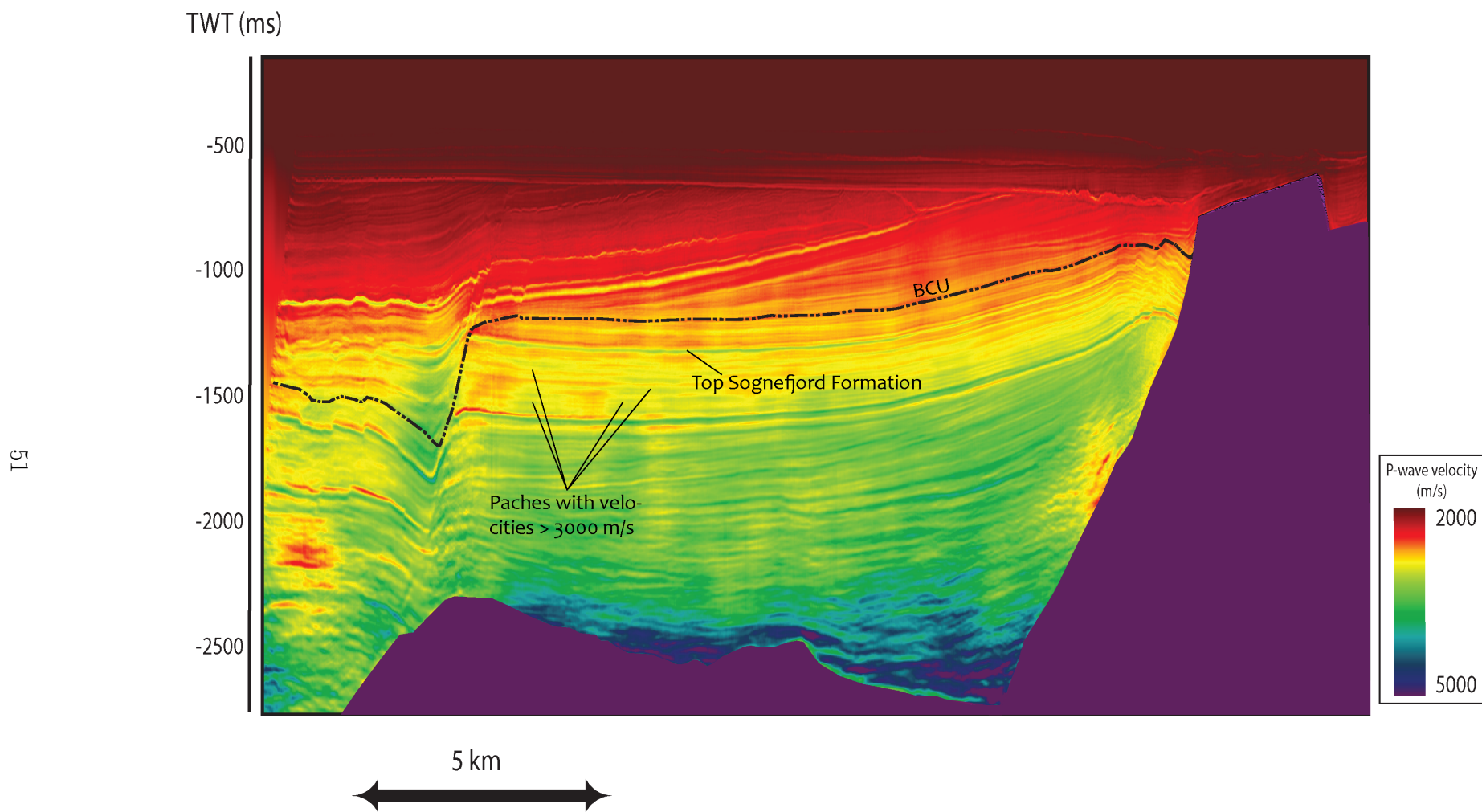
Figure 5.7. V_p inversion result. Note how the velocities above the BCU are less than 3000 m/s, suggesting that the sediments are only mechanically compacted. Beneath Top Sognefjord Formation, patches of sediments with velocities higher than 3000 m/s are observed. This indicates a modest degree of chemical compaction or presence of calcite cement.

TWT (ms)
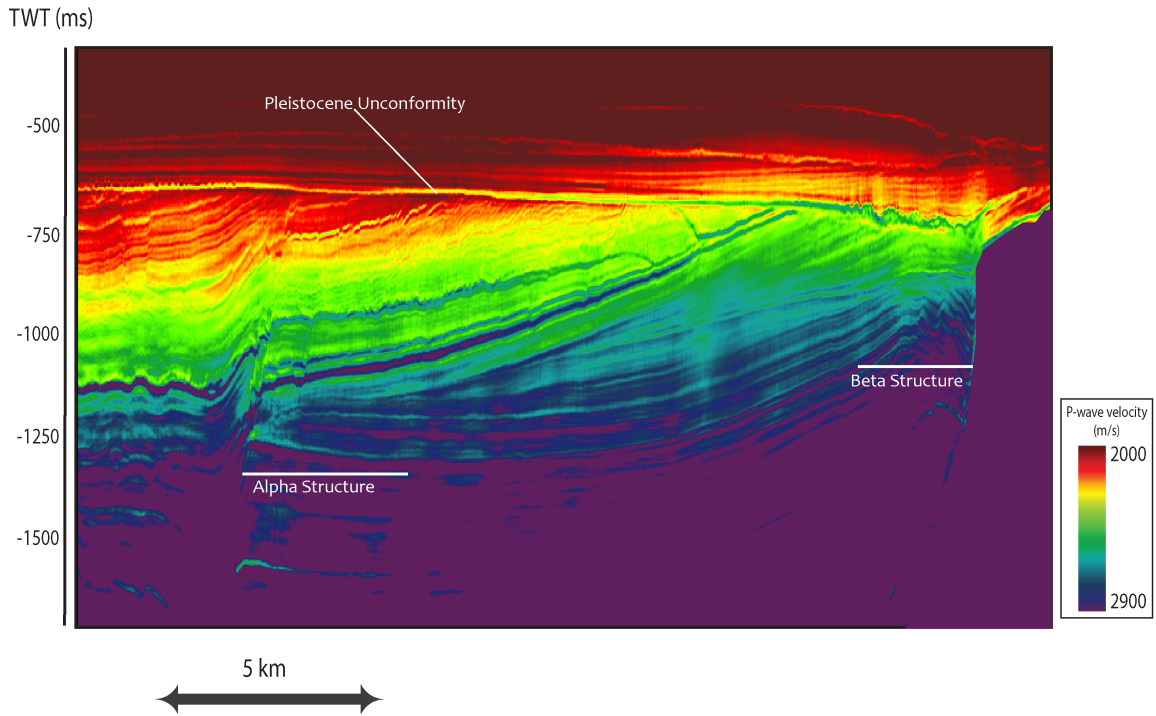
Figure 5.8. P-wave inversion at the shallower section with a narrower color scale to observe the differences. Notice the lateral increase in velocity from E-W beneath the PU.

5.2.2 V_{cl} Inversion

5.2.2.1 Description

The V_{cl} data is estimated by applying the regression line found from cross plotting the EEI log where $\chi = 30^o$ and the derived V_{cl} log (Fig. 4.6) to the inverted EEI volume (Fig. 5.9). The data ranges from 0 to 100 %, where 0 % is estimated clean sand and 100 % is estimated clean shales. Due to lack of shallow amplitudes in the pre-stack derived reflectively, the V_{cl} data starts right above the PU, and most of the Quaternary package is missing.

Down to -1100 m several lateral extending and alternating sand/shale bodies cover most of the cross-section and share a similar signature in the data. There is an abrupt increase in sand content from approximately -1250 m and below. Within the Sognefjord Formation two clinothem features that are high in sand content down-lap on a more horizontal sand unit. These clinothems are capped by finer-grained sediments. Smaller order features within these clinothems are not observed. A horizon-slice (Fig. 5.10)

52

through these features indicates that they extend N-S, and are slightly curved (concave to the west).

5.2.2.2   Interpretation

The data is very noisy in the shallow section. The horizontal reflectors are interpreted as multiple energy. There is a potential risk of mistaking noise for clean sandstones. The clinothems are interpreted as the Sognefjord Formation and have apparently prograded from east to west. This progradation suggests a provenance to the east, which likely correlates with late Jurassic uplift of southern Norway. The curvature of the clinothems, with regards to the progradation direction, has been interpreted as evidence of a wave-dominated delta system (Patruno et al., 2015). The fine-grained sediments that inter-finger the clinothems are consistent with laterally varying depositional environments.
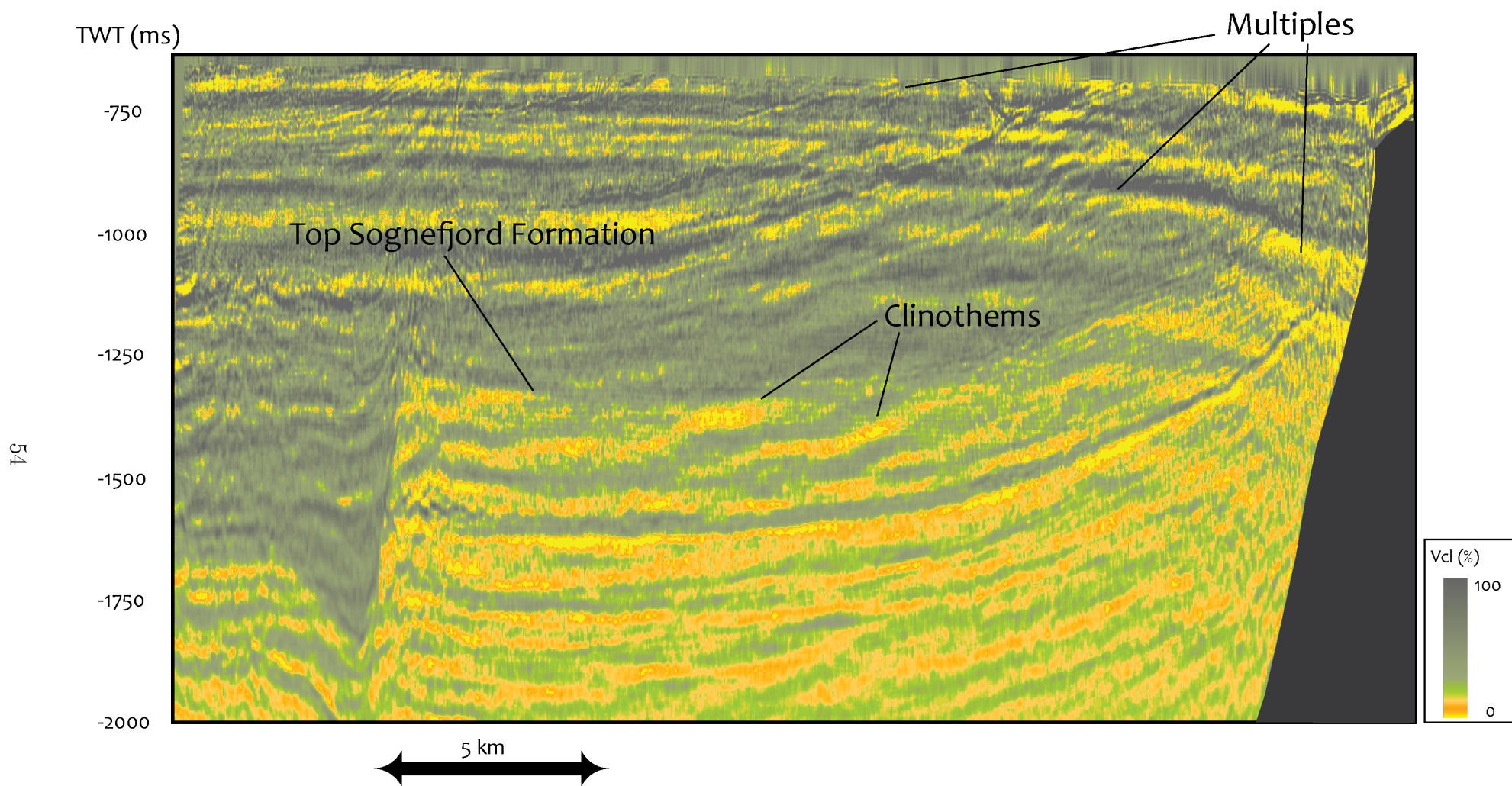
Figure 5.9. V_{cl} inversion result. Some of the multiples are highlighted, also the Westwards prograding clinothems. Note how these clinothems is not present in the post-stack reflection seismic (Fig. 5.1) and how cross cuts all the sandy delta formations in the Viking Group.
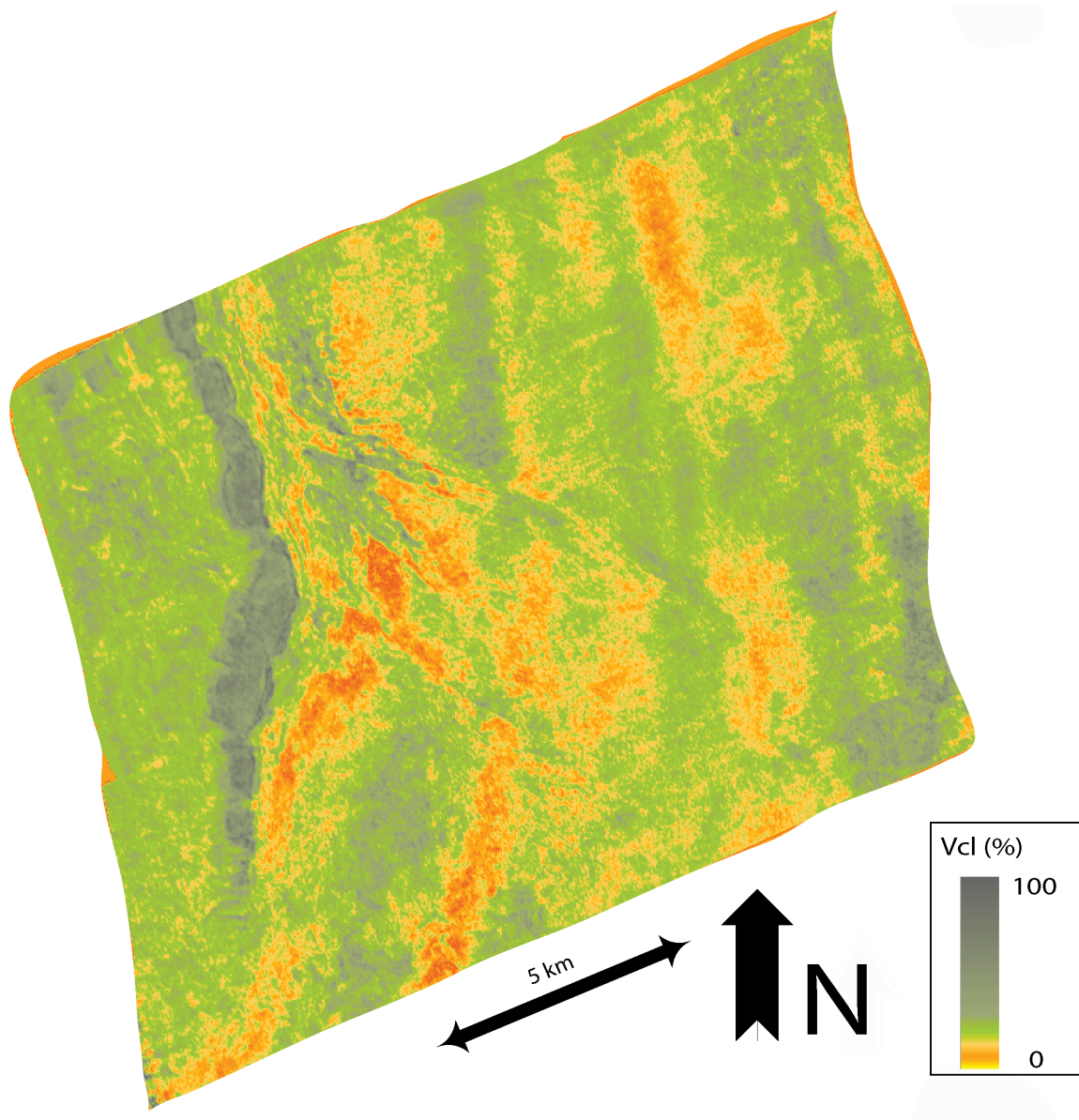
Figure 5.10. Horizon-slice through approximately mid Sognefjord Formation in the V_{cl} cube. Note how the sandy clinothems are continuing N-S slightly concaving to the west.

5.2.3 Net-erosion Estimates

The following results are estimated using the two inverted seismic volumes presented in the previous subsections.

5.2.3.1   Description

The interpolated estimation of clean-sand velocities below the PU increase eastwards (Fig. 5.11 A.). However, minor fluctuating changes are also observed in the net-erosion estimates (Fig. 5.11 B.). The highest velocities are in the north-east corner of the study area, above the Beta Structure, and reach 2800 m/s. Above the Alpha Structure and the Beta Structure, the net-erosion is approximately 900 and 1700 m, respectively. The surface reconstructed in Figure 5.11 C. is an estimation of all sediments eroded between the Quaternary and the PU. Generally, the erosion consistently increases eastwards and reaches its peak above the Beta Structure.

5.2.3.2   Interpretation

As the velocities don't reach 3000 m/s, we can assume that no chemical compaction has occurred in these sediments. Therefore, the net-erosion estimate is valid in the sense that the NVT is predicting only mechanically compacted clean sands, assuming the V_{cl} volume is realistic. Increase in net-erosion towards the east coincides with more uplift towards southern Norway. Also, these results seem reasonable regarding that older formations are sub-cropping beneath the PU in the same direction and the measured velocities are increasing.
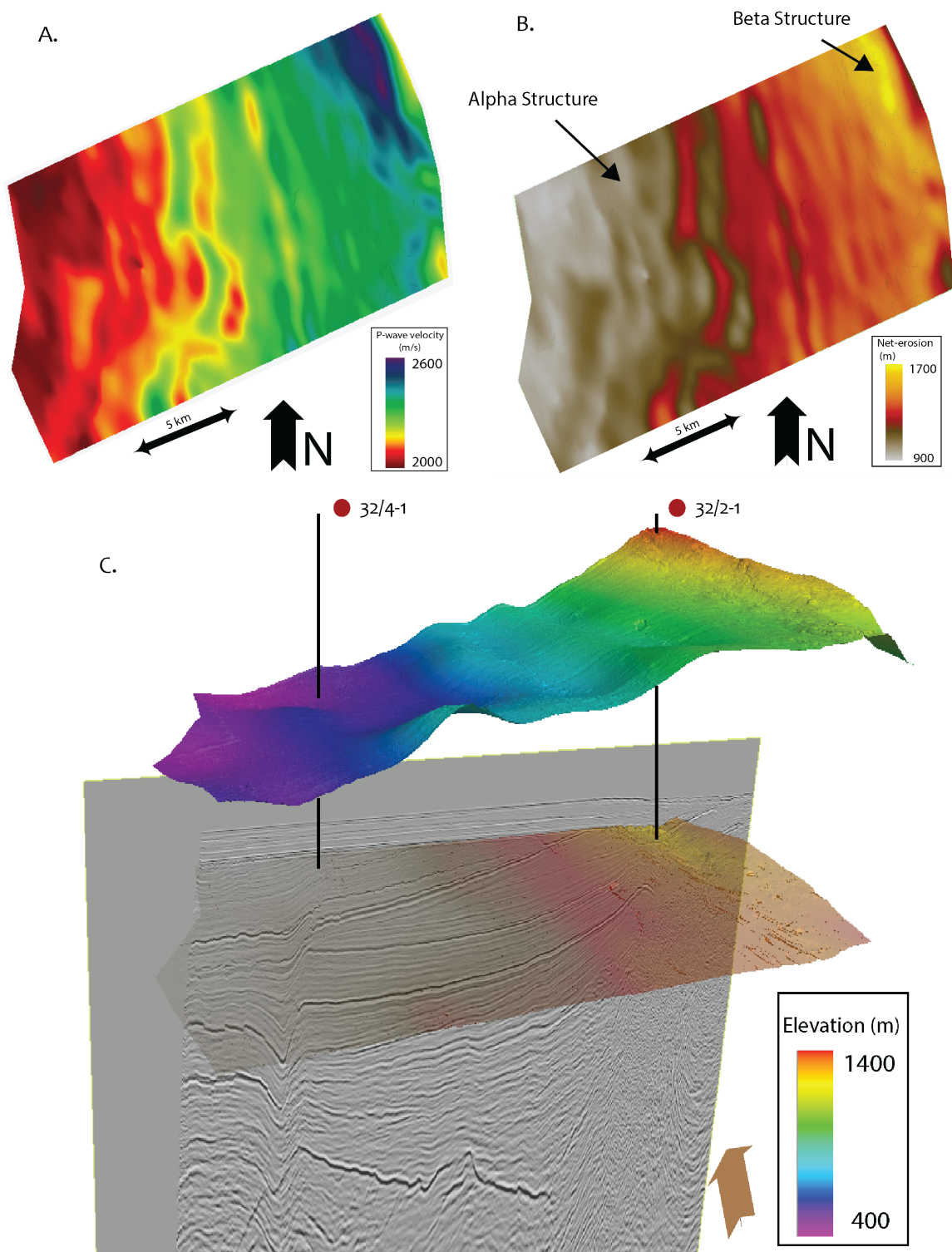
Figure 5.11. Estimated net-erosion above the Pleistocene angular unconformity. A. The angular unconformity surface draped with, interpolated and smoothed, V_p measurements of clean sand. B. The same surface draped with net-erosion estimates from comparing A. with the NVT presented in Eq. 4.1. C. A surface of the estimated eroded stratigraphy. Obtained from the values of B. added to the depth values of the Pleistocene angular unconformity surface.

5.3   Structural Restoration and Backstripping

In this section, a step-by-step backstripping, decompaction and structural restoration of the Smeaheia geomodel based on seismic interpretation is presented (Fig. 5.12). Each seismic unit is assigned reconstruction parameters and ages, based on lithology interpretation from the petrophysical well logs, and well tops (NPD).
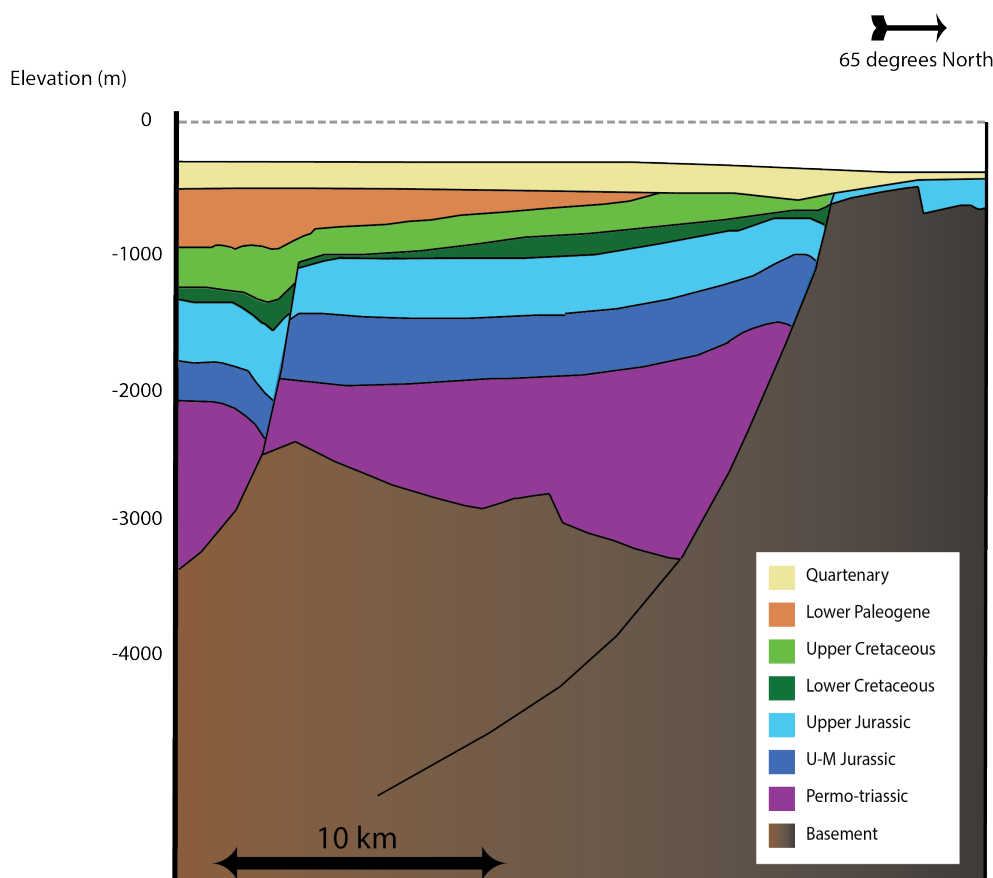
Figure 5.12.   Cross-section of the interpreted geo-model created in Move. The seismic units are assigned decompaction parameters from Table 4.3

5.3.0.1   Description

The restoration process involves removing successions sequentially (youngest – oldest), decompacting the underlying strata, and shifting the underlying strata back to the depositional paleobathymetry (See Section 4.2 for a detailed account of the method). The first step of this process removed the entire Quaternary succession, restoring the geomodel to the time of major erosion and tilting (Fig. 5.13 A.). Then, the estimated

eroded sediments were generated in the model (Fig. 5.13 B.) and the configuration of Late Paleogene was restored by shifting the successions back to the Eocene paleo-obathymetry (Fig. 5.13 C.). Note the impact to the fault block configuration, the Beta Structure is situated deeper than the Alpha Structure. In the reconstructed late Jurassic, the Alpha and Beta Structures are situated at the same depths (Fig. 5.14).

The burial history, for both the Alpha and Beta Structures in for the proposed Late Jurassic storage formation, was estimated by recording the depth value for each recon-struction phase (Fig. 5.15). The reservoir interval in the Alpha and Beta Structures reached maximum burial depths of 1648 and 2213 m, respectively. At 30 Ma both structures were uplifted to 720 m and 410 m depth, and as such the Beta Structure was uplifted 1800 m and became shallower than the Alpha Structure. The errors observed in the stacking velocities were also considered as a minimum for the Beta Structure.
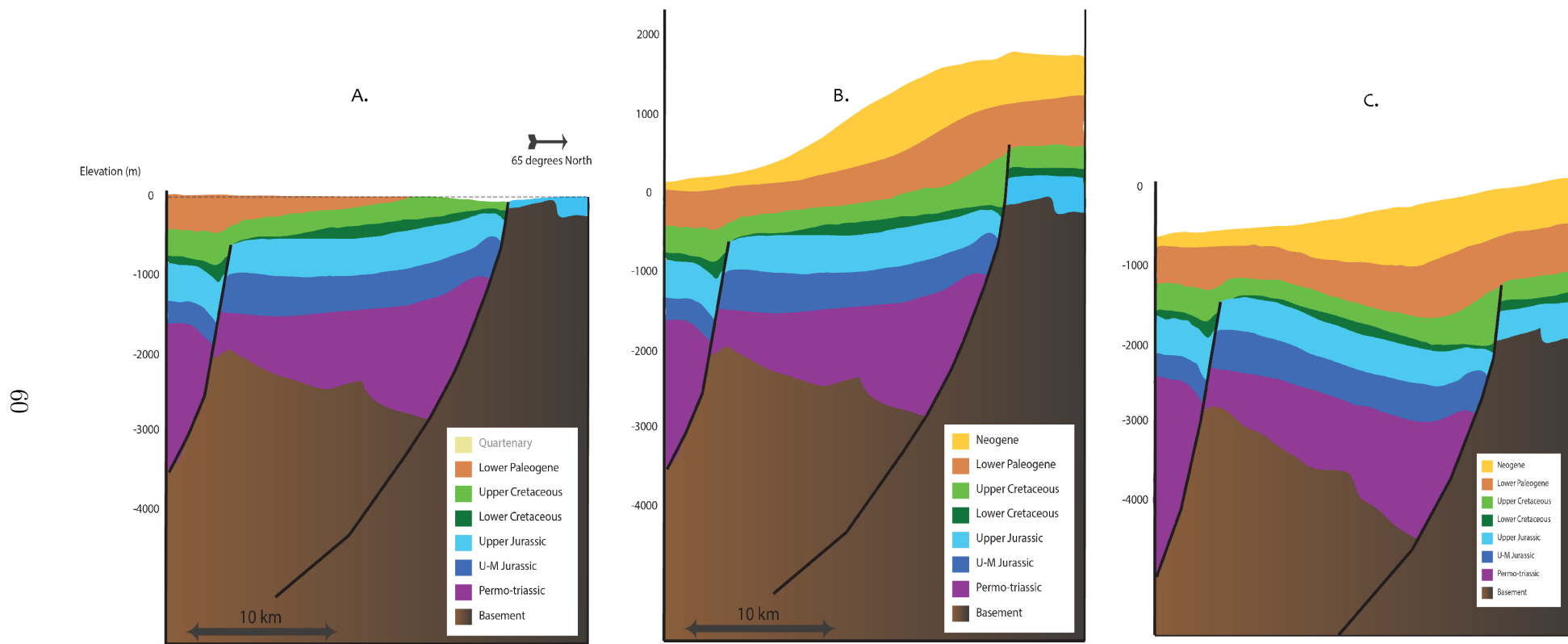
Figure 5.13. First steps of the reconstruction: A. stripping off the Quaternary, then restoring the effects of compaction and isostasy. B. The eroded stratigraphy estimated in section 5.2.3 is restored. C the section is shifted back the paleobathymetry recorded at this time.

Elevation (m)
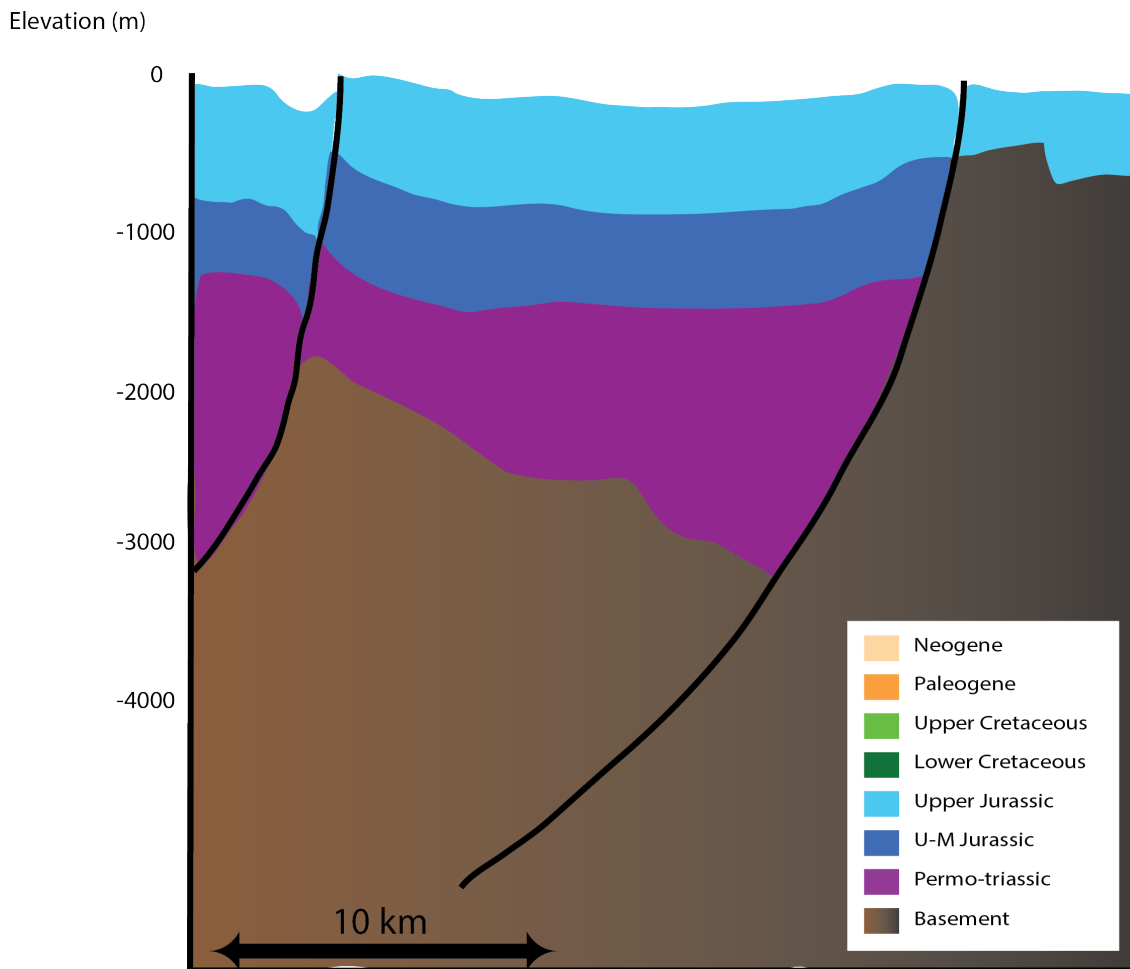
Figure 5.14. The reconstructed configuration of late Jurassic.

5.3.0.2 Interpretation

Observing the reconstruction of the geomodel incrementally back to late Jurassic, (Fig. 5.12−5.14), significant changes to the fault black configuration are apparent. At present, the Alpha Structure is situated at a greater depth than the Beta structure, whereas, during most of the geological evolution of the study area it is the Beta structure that has been situated the deepest. The reconstruction then reveals that the Beta Structure has a deeper maximum burial depth and has undergone greater uplifted (Fig. 5.15).
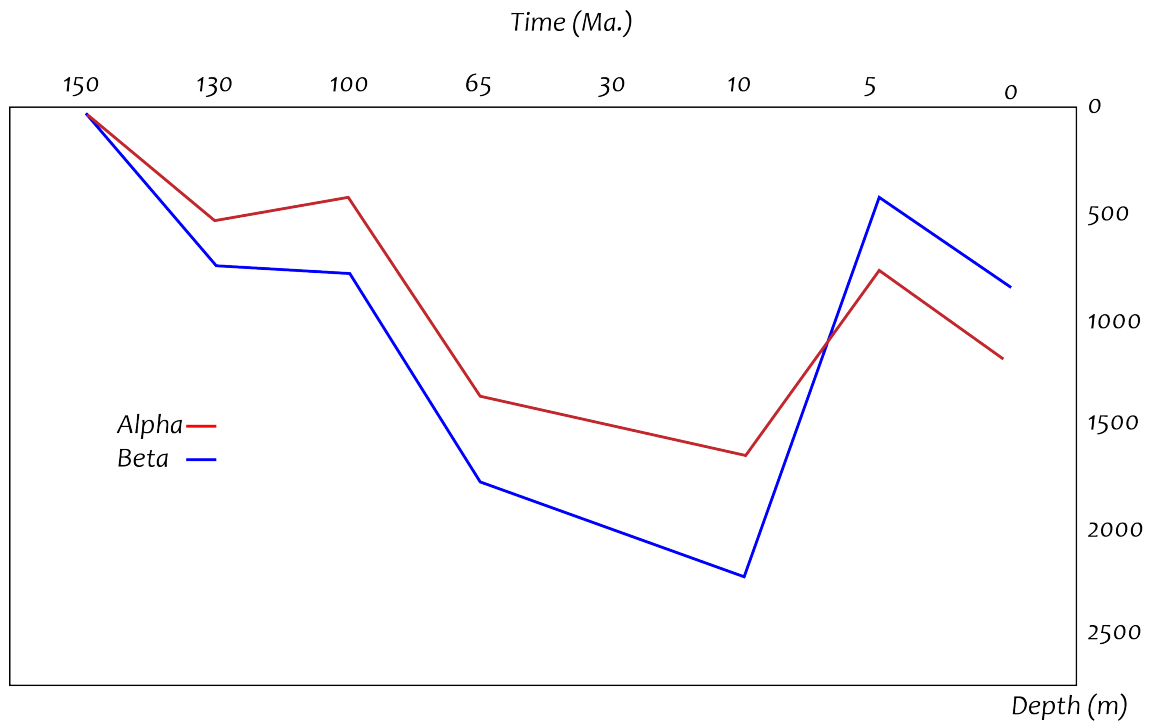
Figure 5.15. Burial history curves for the Alpha (red) and Beta (blue) Structures, determined from the backstripping. The curves indicate subsidence from the late Jurassic to the Cretaceous. At time of fault reactivation ($130-100$ Ma) the Alpha Structure is uplifted and the Beta Structure subsidence rate is reduced. Both the structures rapidly subside from mid to late Cretaceous. The subsidence rate decreases into the Cenozoic, where both structures reach their maximum burial depths. $10-5$ Ma both structures are uplifted.

Chapter 6

Discussion

6.1   Geological Evolution

From the results of the incremental restoration of Smeaheias stratigraphy, we have documented the subsidence and uplift history of the proposed storage site. One of the main elements in the reconstruction was to estimate the eroded stratigraphy above the PU. The resulting net-erosion estimates suggest a high rate of erosion which increases westwards, from 900 m over Alpha and 1700 m over Beta. We suggest two constraints on the timing of this uplift event; (1) pre 1 Ma, as the reflectors within the late Quaternary package horizontal, and (2) after early Eocene, which is the youngest tilted strata within the study area. The eastwards increase in erosion is also evident in the westwards dip of the formations. After inserting the estimated eroded stratigraphy into the geomodel and shifting it back to an estimated paleobathymerty, the fault block configuration is turned and the Beta Structure is situated deeper than the Alpha Structure. This has been the configuration throughout the burial history pre-uplift. The recorded maximum burial depths occurred at approximately 10 Ma and was 2213 m for Beta and 1540 m for Alpha. From 10 to 5 Ma the results suggest that the study area was uplifted; 1800 m and 800 m for Beta and Alpha, respectively.

As addressed in Chapter 4 the methodology and data for estimating net-erosion contain several factors of uncertainty, such as the absolute velocities in the v_p data, the success of extracting clean sandstone bodies from the V_{cl} data and the robustness of the clean

sandstone NVT.

The depth conversion result utilizing the stacking velocities, revealed significant errors in the stacking velocities. Especially at the interval where velocities were extracted to estimate net-erosion over the Beta Structure. Taking these errors into account the maximum burial depth of the Beta Structure is reduced to 1800 m instead of 2213 m, which is more similar to the Alpha Structure's maximum burial depth of 1624 m. A range of depth intervals for the Beta Structure's burial history are therefore proposed (Fig. 6.1). This range also includes quantified uncertainty from the band-limitation between the stacking velocities and the seismic reflection data (Fig. 4.9). The inversion result is estimated to lack mid to low velocity trends oscillating $\pm$ 100 m/s, further giving a $\pm$ 200 m uncertainty to the entire net-erosion result.
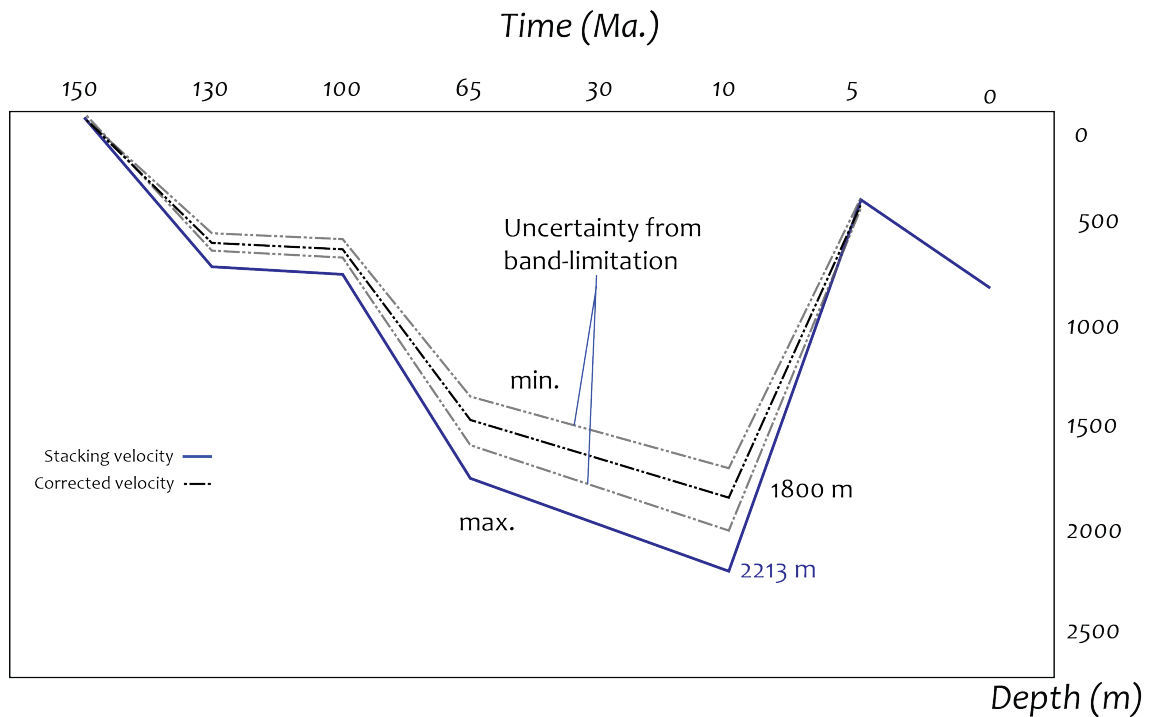
Figure 6.1. The proposed burial histories for the Beta Structure, from evaluating the uncertainties form the stacking velocities and band-limitation, see Figure 4.9 and 5.5.

Compared to the V_p data which was inverted with the post-stack seismic, the V_{cl} data was derived from the pre-stack seismic. Pre-stack data acquire higher quality data compared to post stacked data (Simm et al., 2014). This is reflected in the amount of noise present in the inversion result. The noise is interpreted as multiples, and has potentially been misinterpreted as sand units and used in the net-erosion estimates.

Another potential source of error in the net-erosion estimates is the possibility of mixing clean sandstone bodies for carbonate or chalks, as both of these lithologies have low readings in the GR log (Mondol, 2015). This lithology mix-up could potentially create significant overestimation of the net-erosion, as carbonates have much higher seismic velocities in shallow sections (Bjørlykke, 2015a). Furthermore, even if 100 % clean sandstone bodies have been extracted from the pre-stack inversion, compaction behavior and subsequent the velocities will still vary as a function of rock properties such as; grain size, shape, sorting and packing (Fawad et al., 2010, 2011). The effects on of the uncertainties discussed in this paragraph, to the burial histories have not been quantified.

Net-erosion estimates are compared to previous publications (Riis, 1996; Doré and Jensen, 1996; Baig et al., 2019), where both the magnitude and rate of increase in uplift to the east are significantly higher in this study (Fig. 6.2). Doré and Jensen (1996) and Riis (1996) both extrapolated offshore terminated reflectors to corresponding onshore morphology. The extrapolation is > 50 km, with no guided net-erosion estimates above Smeaheia. Baig et al. (2019)'s conclusions are supported by the variety of the net-erosion estimates performed including shale compaction trends, thermal measurements, and vitrinite reflection. These results were considered robust as the different net-erosion estimations corresponded well. However, these results were obtained from well data, which is spatially limited compared to seismic attribute data utilized in this study. Also, well 32/2-1 is the well closest to onshore Norway in the northern North Sea, and frequent sidewall collapse occurred in the borehole from drilling (Fig. 4.8). As a large degree of uncertainty has been recognized in both the data and methods used to estimate net-erosion in this study and from comparing the results to other studies, indicates that the lower section of the range of burial histories proposed for the Beta Structure are more realistic (Fig. 6.1).

The net-erosion results from this thesis suggest more local subsidence, erosion and uplift compared with Doré and Jensen (1996), Riis (1996) and Baig et al. (2019), who suggest a regional scale dynamic. Where the latter is more realistic in terms of an offshore response to uplift of southern Norway. However, reactivation of basement faults such as Vette and Øygarden has in some cases been credited sediment loading and advancing ice sheets (Mulrooney et al. 2017 and references therein). These mechanisms

can potentially have induced considerable local variations in subsidence, erosion and uplift, as the result in this thesis suggests.
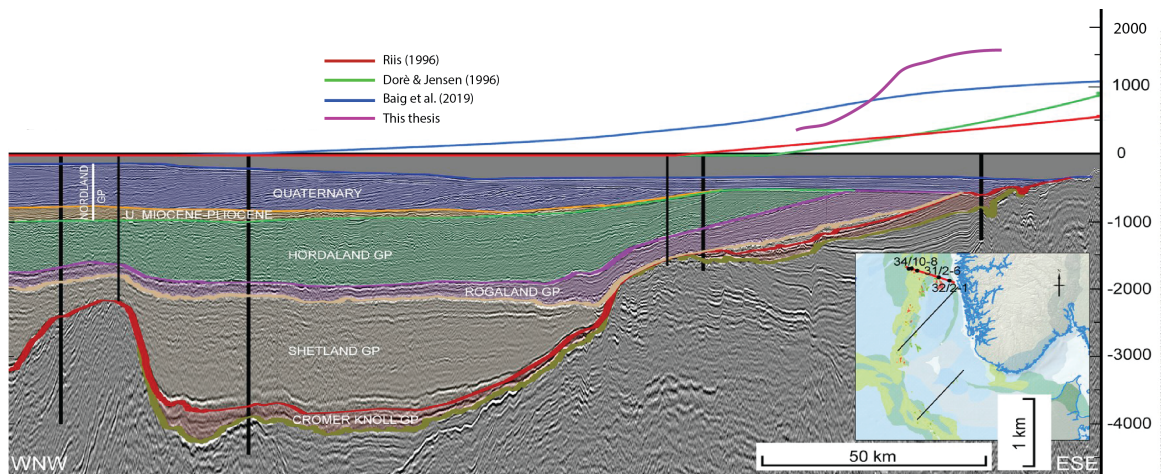

Figure 6.2. Comparison of net-erosion estimations with other studies. Note the much higher the rate of increase in net-erosion results is in this thesis compared to the earlier studies, which suggest more local erosion and uplift. Adapted from Baig et al. (2019)

There has been a great debate concerning the presence of mountains surrounding the North Atlantic passive margin, including areas such as southern and northern Scandes, and Greenland (Riis, 1996; Jordt et al., 1995; Japsen and Chalmers, 2000; Lidmar-Bergström et al., 2000; Nielsen et al., 2009, 2010). One theory is that roots from the Caledonian mountain range have remained since collapsing in the Devonian, and that climatic effects have led to erosion and isostatic uplift (Nielsen et al., 2010). This would explain the presence of deep metamorphic rocks found in summits of Norway, however, the theory struggles to explain the absence of a Caledonian crustal root beneath present day Norway (Anell et al. 2009 and references therein). In addition, during the mid Cretaceous, thick deposition of clean chalk occurred with little to no influx of silica clastics. This is explained by limited surrounding topography. If the mountains of Norway were present at this time, one would expect influx of silica clastic sediments. It is therefore speculated that the mountains of Norway have been uplifted post the Cretaceous (Riis, 1996; Jordt et al., 1995; Japsen and Chalmers, 2000; Lidmar-Bergström et al., 2000).

Cenozoic uplift of the North Atlantic passive margins is supported by the presence of several high elevated peneplains in Norway (Doré and Jensen, 1996; Riis, 1996;

Lidmar-Bergström et al., 2000). Furthermore, Cenozoic progradational packages have been mapped in the offshore basins suggesting recent uplift of provenances to the east (Jordt et al., 1995; Faleide et al., 2002; Anell et al., 2012; Jarsve et al., 2015). Also indicative of post Cretaceous uplift of Norway is the termination of tilted Cenozoic successions at the eastern basin margin of the North Sea, which is common situation at the passive margins for the entire North Atlantic (Japsen and Chalmers, 2000; Baig et al., 2019). Yet, the driving mechanism, magnitude, and timing of this uplift are still under debate (Anell et al., 2009). Some suggest that changes in climate and subsequent erosion and isostatic uplift are enough to explain the magnitude, as erosion and isostatic uplift enhance each other (Nielsen et al., 2010). Whereas others argue tectonic processes are needed to explain the uplift, especially as certain major uplift events i.e. Eocene-Oligocene, correspond with non-glacial periods, prohibiting erosion (Jordt et al., 1995). Suggested tectonic mechanisms resulting in uplift include intra-plate stress from the Atlantic break-up and/or the Alpine orogeny, development of the Icelandic Plume, and underplating and volcanism (Jordt et al., 1995; Boldreel and Andersen, 1998; Clift and Turner, 1998; Japsen and Chalmers, 2000; Faleide et al., 2002; Holford et al., 2008; Jarsve et al., 2015).

Several elevated peneplain surfaces/scarps have been mapped in Norway, and from studying offshore progradational packages and using fission track analysis these surfaces have been tentatively dated (Lidmar-Bergström et al., 2000). Peneplains are believed by some to form times of little vertical movement where lateral erosion down to base-level forms a flat surface, which later is uplifted and preserved at higher elevations (Anell et al., 2012). The steep eastwards increase in the net-erosion result suggest that the study area has been responded to uplift of southern Norway. To analyze this on a regional scale the net-erosion results were extrapolated to the peneplain with the present elevation corresponding to the highest net erosion estimates to the east. This peneplain is tentatively estimated to be formed in the Paleocene (Lidmar-Bergström et al., 2000). The net-erosion estimates were also extrapolated to the corresponding truncated reflector in the offshore basin (Fig. 6.3).

Figure 6.3 illustrates the results of the reconstruction in a regional setting at important geological time periods. In the late Cretaceous the sea level dropped approximately 200 m (Haq et al., 1987), resulting in exposure of southern Norway, initiating erosion and

isostatic rebound (Anell et al., 2009). This exposure implies that Norway was situated relatively high compared to surrounding areas. An indication of this is the westward progradational clinothems observed in the Upper Jurassic suggesting a provenance to the east at the time (Dreyer et al., 2005; Patruno et al., 2015). Hay and Southam (1977) estimated the resulting isostatic uplift of the mountain peaks from 200 m exposure and ensuing erosion, to be 400−600 m. Figure 6.3 A.−B. demonstrate the mid to late Cretaceous rebound of southern Norway into the Paleocene, forming early topography from fluvial incision down to base-level. From a following time of quiescence, lateral erosion has then potentially formed the later uplifted Paleocene peneplain.

Extrapolating the net-erosion results to both offshore and onshore Paleocene surfaces implies that the reconstructed regional setting in Figure 6.3 B. must have been significantly tilted post-Paleocene i.e. uplift of southern Norway and subsidence in the interior basin. This contradicts earlier mentioned speculations, that the mountains of Norway are eroded remains of the Caledonian (Nielsen et al., 2009). The apparent regional tilt is suggested to have occurred in the Eocene to Oligocene transition (Fig. 6.3 C.). This is reflected by high relative sea-level measurements in the Viking Graben at the time (Kjennerud and Sylta, 2001; Kyrkjebø et al., 2001), caused by abnormal high subsidence rates (Jordt et al., 1995; Nadin and Kusznir, 1995; Jarsve et al., 2015). Also reflecting Eocene Oligocene tilt, is observed late Oligocene sedimentary units prograding in to the North Sea, from what is tied to hinterlands where southern Norway is today (Jarsve et al., 2015).

Note how the reconstruction suggests that the Troll Field was an island in the Cretaceous, and that the Smeaheia fault block was buried deeper (Fig. 6.3 A.). The setting is similar in the Paleocene except for further burial and deposition (Fig. 6.3 B.). As ongoing thermal subsidence from the late Jurassic to mid Cretaceous rift generated accommodation space centered in the Viking Graben (Gabrielsen et al., 2001; Færseth, 1996), the main Paleocene depocenters where situated close to the shore-line at the mouth of the Sognefjord (Lidmar-Bergström et al., 2000), close to the study area. This is a possible explanation to why the reconstructed thickness of the Paleocene package is seemingly constant, and not thickening towards the Viking Graben where thermal subsidence occurs.

The Eocene-Oligocene uplift of southern Norway is credited tectonism, as the period was non-glacial, high sea-level isolates a large degree of erosion and isostatic uplift (Jordt et al., 1995). A shift from western to eastern sedimentary influx in the early Quaternary is evident from deposition of thick clastic wedges prograding to the east, suggesting a new phase of tectonic uplift to the east (Fig. 6.3 D.; Faleide et al. 2002). As these early Quaternary wedges are also eroded, a final early to mid Quaternary erosion phase is suggested (Baig et al., 2019) corresponding to the glacial times (Fig. 6.3 E.).
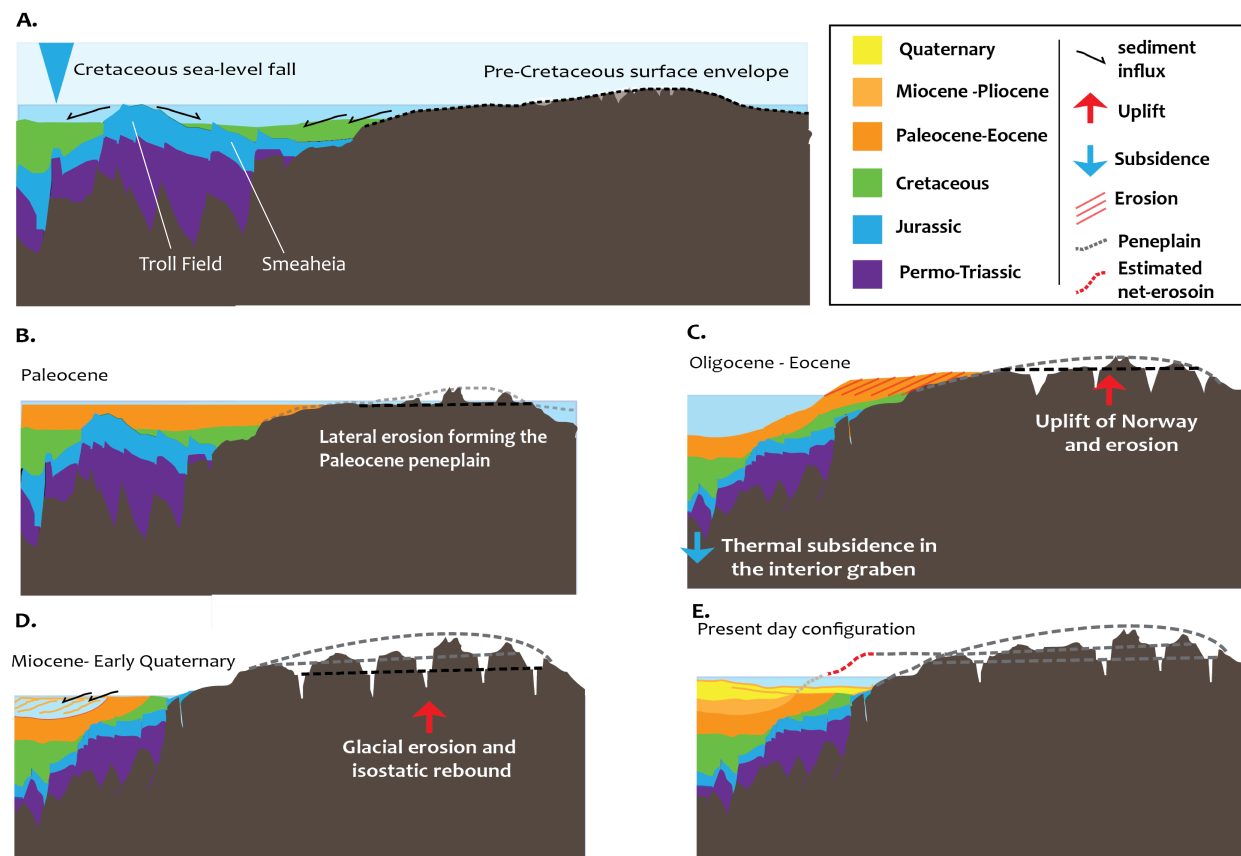
Figure 6.3. A cartoon reconstruction of the results. Note that the horizontal scale of Norway is understated. A. At late Cretaceous, sea-level fall exposes Norway and erosion starts. B. Late Cretaceous to Paleocene erosion formed early Norwegian topography, which later matured to lateral erosion, forming the Paleocene peneplain. C. Oligocene-Eocene uplift of Norway and high subsidence rates in the Viking Graben results in tiling and erosion of the basin margin successions. D. Further erosion results in uplift of Norway and inducing more erosion of the offshore successions. E. Present day configuration with inserted net-erosion estimates, connected to the Top Paleocene truncated reflector and a peneplain in Norway formed in the Paleocene. These figures are re-drawn from Faleide et al. (2015) and Lidmar-Bergström et al. (2000), timings of geological events are based on Hay and Southam (1977); Haq et al. (1987); Jordt et al. (1995); Faleide et al. (2002); Anell et al. (2009); Nielsen et al. (2010).

6.2   Implications for CO$_2$ Storage

Given a significant difference in the reconstructed subsidence and uplift history of the Alpha and Beta Structures, their reservoir and sealing properties should also differ. The results suggest that the Beta Structure has been buried deeper than the Alpha Structure. The Beta Structure has therefore been mechanically compacted faster, and been exposed to higher temperatures. Well 32/4-1 which is penetrating the Alpha Structure, recorded a thermal gradient of 34 ^{o}C/km. Considering the maximum burial depth for the Alpha Structure which is recorded to be 1614 m, the maximum temperature the Alpha Structure has reached is therefore estimated to be 54 ^{o}C.

Assuming that chemical compaction starts at 70 ^{o}C (Bjørlykke and Jahren, 2010) the Alpha Structure will be limited to mechanical compaction. As for the Beta Structure, different burial histories have been proposed (Fig. 6.1). The thermal gradient from well 32/2-1 that penetrates the Beta Structure is estimated to be 43 ^{o}C/km. Figure 6.4 illustrates the variation of possible spans the Beta Structure has been exposed to chemical compaction. The maximum interval spans for 60 million years, where the highest temperature reached is 95°C. This suggests that the formation should be well consolidated (Walderhaug, 1996). Whereas for the minimum burial history, the Beta Structure reaches 70 ^{o}C for a few of million years. The deepest reconstructed burial history for the Beta Structure is based on the net-erosion estimates calculated without addressing the observed overestimated values in the stacking velocities. Considering the estimated errors from the stacking velocities (Fig. 5.5) and the significant higher net-erosion estimates compared to earlier studies, we suggest a higher certain towards the lower reconstructed burial histories.

Another aspect to consider is that the reconstruction results suggested that the structures were uplifted from 10 to 5 Ma. As discussed in the previous section, the uplift is rather believed to be initiated in the Eocene-Oligocene transition. Hence, the structures exposure to chemical compaction will be reduced if the uplift started earlier.
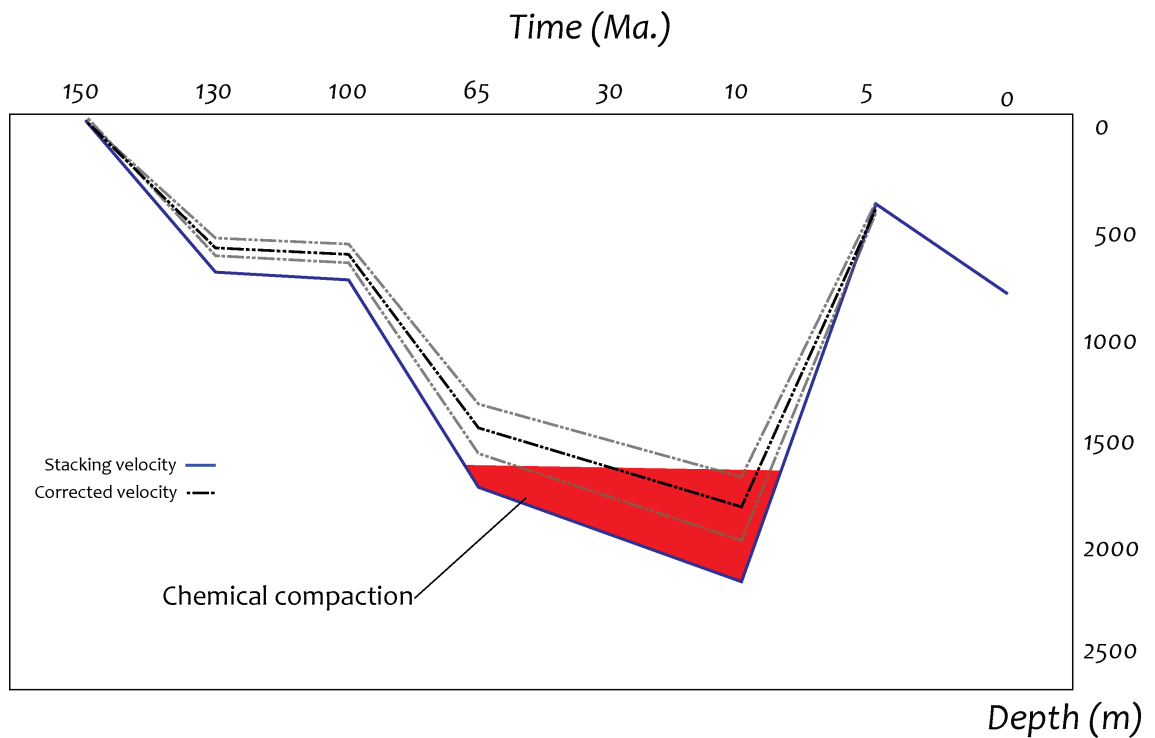
Time (Ma.)

Figure 6.4. Evaluation of the potential chemical compaction for the different burial histories proposed for the Beta Structure. Note the significant difference in the chemical compaction span for the minimum and the maximum burial history.

When CO$_2$ is injected into the storage formation and the CO$_2$ plume reaches the reservoir- caprock interface the caprock is exposed to vertical stress (Shukla et al., 2010). As caprocks are uplifted, they are more prone to a brittle response to this stress and will more easily fracture (Doré et al., 1997; Nygård et al., 2006; Henriksen et al., 2011). Makurat et al. (1992) recognized a correlation between hydrocarbon leakage and caprock uplifted more than 1600−1700 m. The Alpha Structure is estimated to be uplifted 1128 m, which is under this recognized limit. Uplift of the Beta Structure is dependent on which burial history, where the minimum is uplifted 1200 m and the maximum is uplifted 1800 m. As addressed earlier we suggest there is more confidence in the lower burial history. Hence, the uplift of the Beta Structure is less than Makurat et al. (1992) recognized as potentially fracture inducing.

6.3   Recommended Further Work

The method used to estimate net-erosion in this thesis has proven to have limitations. The V_p data generated from seismic inversion, has uncertainty in its absolute values. This is caused by a frequency gap between the stacking velocities and the seismic data. In addition, the stacking velocities have been shown to overestimate the true low-frequency velocities, especially above the Beta Structure. We therefore recommend using a higher resolution and better calibrated velocity model. By using new broadband seismic, which is recently acquired in the northern North Sea and covers the study area, together with Full Waveform Inversion (FWI), the frequency gap can be filled providing more robust absolute velocities (Fig. 6.5; Routh et al. 2016).

The pre-stack data used to estimate the V_{cl} data should be conditioned to limit the amount of noise contaminating the data. Then the risk of extracting velocities of random noise instead of clean sandstones is reduced. Furthermore, properly migrated and scaled amplitudes at long offset, post the critical angle can be used to invert for density (Hampson et al., 2005). Density data provide better lithology control, especially for separating carbonates and chalks from sandstones in shallow sections (Simm et al., 2014).

To constrain the net-erosion estimates further we recommend to also evaluate different lithologies such as shale and chalk, whose net-erosion estimates should correspond. Also, assessing the range of compaction trends within each clean lithology, which varies based on texture and mineralogy (Mondol et al., 2007; Fawad et al., 2011). Another aspect that has not been addressed in this thesis is the vertical and horizontal resolution of the seismic inversion results, and if certain lithologies are more prone to appear in these scales than others are. But applying the method to shallow depths, as done in this thesis, will increase the seismic resolution and thereby reduce the volume needed of a certain clean lithology.

As discussed earlier the data only covers a small part of the northern North Sea. Important features of the basin and their impact on the basin development are therefore not quantified. Utilizing a data set that covers the most important features of the basin will provide a more robust reconstruction. Studying stratigraphic features on a large

data set can reveal regional drainage directions, which in turn can provide information of timing and centers of large scale vertical movements.

To assess the porosity and brittleness for the storage site more quantitatively, we recommend analyzing core samples of the storage formations. Core samples are available for well 32/4-1 and/or drill cuttings which are available for both the wells.
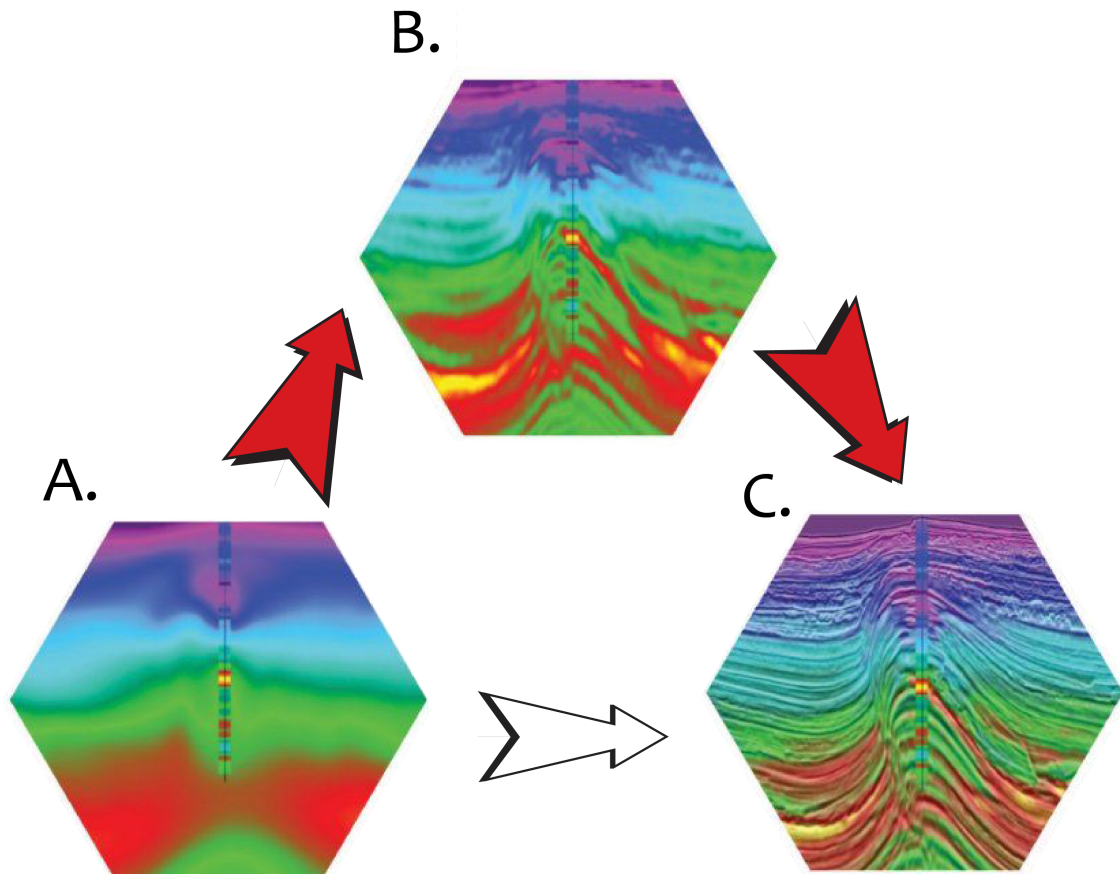

Figure 6.5. A. Stacking velocity model. B. Velocity model after FWI. C. Inversion result using B. as an initial model. The red arrows show the inversion workflow to obtain more robust velocity model, compared to the workflow used in this thesis indicated with the white arrow. Adapted from Routh et al. (2016)

Chapter 7

Conclusions

Essential aspects of the burial history for a proposed CO_2 storage site (Smeaheia) have been investigated. The extensive subsidence to the west and uplift to the east of the study area were assessed, in order to quantify the burial history. The results provide insight to the storage capacity and seal integrity of the proposed reservoir-caprock system, and to the offshore study areas response to the development of Norway. The main findings and concluding remarks from this thesis are given below:

- Net-erosion estimations above the marked Pleistocene unconformity increases rapidly eastwards, towards Norway. This is interpreted to be a response of post Paleocene uplift of Norway. The timing of this uplift has been further constrained from the results to have occurred post early Eocene, continued into the early Quaternary and stopped in some time pre 1 Ma.

- A reconstruction of the development of the North Sea and southern Norway based on the net-erosion estimations and the performed reconstruction, suggests that the Top Paleocene reflector connects to a proposed Paleocene peneplain. The peneplain has been uplifted and incised and the reflector tilted and eroded. The postulated timing of the main uplift is suggested around the Eocene-Oligocene transition.

- The reconstructed maximum burial depths for the Alpha and Beta Structure are 1648 m and 2213 m, respectively, whereas net-uplift is calculated to be 888 m and

1803 m, respectively. The methods and data utilized to estimate net-erosion contains a number of uncertainties. Some of these uncertainties have been quantified and have resulted in a range of possible burial histories for the Beta Structure. The minimum scenario is similar to the burial history reconstructed for the Alpha Structure, which suggests mainly mechanical compaction and relatively low net-uplift in terms of overconsolidation. Whereas the maximum scenario suggest 60 million years of chemical compaction and high enough net-uplift values for the storage formations to be overconsolidated.

Bibliography

Anell, I., Thybo, H., and Artemieva, I. (2009). Cenozoic uplift and subsidence in the north atlantic region: Geological evidence revisited. *Tectonophysics*, 474(1-2):78–105. DOI: https://doi.org/10.1016/j.tecto.2009.04.006.

Anell, I., Thybo, H., and Rasmussen, E. (2012). Asynthesis of cenozoic sedimentation in the north sea. *Basin Research*, 24(2):154–179. DOI: 10.1111/j.1365-2117.2011.00517.x.

Avseth, P., Mukerji, T., and Mavko, G. (2010). *Quantitative seismic interpretation: Applying rock physics tools to reduce interpretation risk*. Cambridge university press. DOI: .

Baig, I., Faleide, J. I., Jahren, J., and Mondol, N. H. (2016). Cenozoic exhumation on the southwestern barents shelf: Estimates and uncertainties constrained from compaction and thermal maturity analyses. *Marine and Petroleum Geology*, 73:105–130. DOI: https://doi.org/10.1016/j.marpetgeo.2016.02.024.

Baig, I., Faleide, J. I., Mondol, N. H., and Jahren, J. (2019). Burial and exhumation history controls on shale compaction and thermal maturity along the norwegian north sea basin margin areas. *Marine and Petroleum Geology*. DOI: https://doi.org/10.1016/j.marpetgeo.2019.03.010.

Bjørlykke, K. (2015a). Compaction of sedimentary rocks: Shales, sandstones and carbonates. In *Petroleum Geoscience*, pages 351–360. Springer. DOI: https://doi.org/10.1007/978-3-642-34132-8_13.

Bjørlykke, K. (2015b). Introduction to petroleum geology. In *Petroleum Geoscience*, pages 1–29. Springer. DOI: https://doi.org/10.1007/978-3-642-34132-8_1.

Bjørlykke, K. and Høeg, K. (1997). Effects of burial diagenesis on stresses, compaction and fluid flow in sedimentary basins. *Marine and Petroleum Geology*, 14(3):267–276. DOI: https://doi.org/10.1016/S0264-8172(96)00051-7.

Bjørlykke, K. and Jahren, J. (2010). Sandstones and sandstone reservoirs. In *Petroleum Geoscience*, pages 113–140. Springer. DOI: .

Boldreel, L. and Andersen, M. (1998). Tertiary compressional structures on the Faroe–Rockall Plateau in relation to northeast Atlantic ridge-push and Alpine foreland stresses. *Tectonophysics*, 300(1-4):13–28. DOI: https://doi.org/10.1016/S0040-1951(98)00231-5.

Castagna, J. P. and Swan, H. W. (1997). Principles of AVO crossplotting. *The leading edge*, 16(4):337–344. DOI: https://doi.org/10.1190/1.1437626.

Clausen, J., Gabrielsen, R., Reksnes, P., and Nysaether, E. (1999). Development of intraformational (Oligocene–Miocene) faults in the northern North Sea: influence of remote stresses and doming of Fennoscandia. *Journal of Structural Geology*, 21(10):1457–1475. DOI: https://doi.org/10.1016/S0191-8141(99)00083-8.

Clift, P. D. and Turner, J. (1998). Paleogene igneous underplating and subsidence anomalies in the Rockall-Faeroe-Shetland area. *Marine and Petroleum Geology*, 15(3):223–243. DOI: https://doi.org/10.1016/S0264-8172(97)00056-1.

Connolly, P. (1999). Elastic impedance. *The leading edge*, 18(4):438–452. DOI: https://doi.org/10.1190/1.1438307.

Dix, C. H. (1955). Seismic velocities from surface measurements. *Geophysics*, 20(1):68–86. DOI: https://doi.org/10.1190/1.1438126.

Doré, A., Corcoran, D., and Scotchman, I. (2002). Prediction of the hydrocarbon system in exhumed basins, and application to the NW European margin. *Geological Society, London, Special Publications*, 196(1):401–429. DOI: https://doi.org/10.1144/GSL.SP.2002.196.01.21.

Doré, A. and Jensen, L. (1996). The impact of late Cenozoic uplift and erosion on hydrocarbon exploration: offshore Norway and some other uplifted basins. *Global and Planetary Change*, 12(1-4):415–436. DOI: .

Doré, A., Lundin, E., Fichler, C., and Olesen, O. (1997). Patterns of basement structure and reactivation along the NE Atlantic margin. *Journal of the Geological Society*, 154(1):85–92. DOI: .

Dreyer, T., Whitaker, M., Dexter, J., Flesche, H., and Larsen, E. (2005). From spit system to tide-dominated delta: integrated reservoir model of the Upper Jurassic Sognefjord Formation on the Troll West Field. In *Geological Society, London, Petroleum Geology Conference series*, volume 6, pages 423–448. Geological Society of London. DOI: https://doi.org/10.1144/0060423.

Ebbing, J. and Olesen, O. (2005). The Northern and Southern Scandes—structural differences revealed by an analysis of gravity anomalies, the geoid and regional isostasy. *Tectonophysics*, 411(1-4):73–87. DOI: https://doi.org/10.1016/j.tecto.2005.09.002.

Eyles, N. (1996). Passive margin uplift around the North Atlantic region and its role in Northern Hemisphere late Cenozoic glaciation. *Geology*, 24(2):103–106. DOI: https://doi.org/10.1130/0091-7613(1996)024⟨0103:PMUATN⟩2.3.CO;2.

Færseth, R. (1996). Interaction of Permo-Triassic and Jurassic extensional fault-blocks during the development of the northern North Sea. *Journal of the Geological Society*, 153(6):931–944. DOI: https://doi.org/10.1144/gsjgs.153.6.0931.

Faerseth, R. (1997). Interaction of Permo-Triassic and Jurassic extensional fault-blocks during the development of the northern North Sea. *Oceanographic Literature Review*, 7(44):710. DOI: .

Faleide, J. I., Bjørlykke, K., and Gabrielsen, R. H. (2015). Geology of the Norwegian continental shelf. In *Petroleum Geoscience*, pages 603–637. Springer. DOI: https://doi.org/10.1007/978-3-642-34132-8_25.

Faleide, J. I., Kyrkjebo, R., Kjennerud, T., Gabrielsen, R. H., Jordt, H., Fanavoll, S., and Bjerke, M. D. (2002). Tectonic impact on sedimentary processes during Cenozoic evolution of the northern North Sea and surrounding areas. *Special Publication-Geological Society of London*, 196:235–270. DOI: https://doi.org/10.1144/GSL.SP.2002.196.01.14.

Fawad, M., Mondol, N. H., Jahren, J., and Bjørlykke, K. (2010). Seismic velocities from experimental compaction: New porosity and velocity-depth relations for sands

with different textural and mineralogical composition. In *SEG Technical Program Expanded Abstracts 2010*, pages 2480–2485. Society of Exploration Geophysicists. DOI: https://doi.org/10.1190/1.3513353.

Fawad, M., Mondol, N. H., Jahren, J., and Bjørlykke, K. (2011). Mechanical compaction and ultrasonic velocity of sands with different texture and mineralogical composition. *Geophysical Prospecting*, 59(4):697–720. DOI: doi:10.1111/j.1365-2478.2011.00951.x.

Fjeldskaar, W., Ter Voorde, M., Johansen, H., Christiansson, P., Faleide, J., and Cloetingh, S. (2004). Numerical simulation of rifting in the northern viking graben: the mutual effect of modelling parameters. *Tectonophysics*, 382(3-4):189–212. DOI: https://doi.org/10.1016/j.tecto.2004.01.002.

Fossen, H., Khani, H. F., Faleide, J. I., Ksienzyk, A. K., and Dunlap, W. J. (2017). Post-caledonian extension in the west norway–northern north sea region: the role of structural inheritance. *Geological Society, London, Special Publications*, 439(1):465–486. DOI: https://doi.org/10.1144/SP439.6.

Gabrielsen, R. H., Kyrkjebø, R., Faleide, J. I., Fjeldskaar, W., and Kjennerud, T. (2001). The cretaceous post-rift basin configuration of the northern north sea. *Petroleum Geoscience*, 7(2):137–154. DOI: 10.1144/petgeo.7.2.137.

Gardner, G., Gardner, L., and Gregory, A. (1974). Formation velocity and density—the diagnostic basics for stratigraphic traps. *Geophysics*, 39(6):770–780. DOI: https://doi.org/10.1190/1.1440465.

Gasser, D. (2014). The caledonides of greenland, svalbard and other arctic areas: status of research and open questions. *Geological Society, London, Special Publications*, 390(1):93–129. DOI: https://doi.org/10.1144/SP390.17.

Gelius, L.-J. and Johansen, T. A. (2010). Petroleum geophysics. *UniGEO as*.

Halland, E. K., Gjeldvik, I., Johansen, W., Magnus, C., Meling, I., Pedersen, S., Riis, F., Solbakk, T., and Tappel, I. (2011). Co2 storage atlas norwegian north sea. *Norwegian Petroleum Directorate, PO Box*, 600. DOI: .

Hampson, D. P., Russell, B. H., and Bankhead, B. (2005). Simultaneous inversion of pre-stack seismic data. In *SEG Technical Program Expanded Abstracts 2005*, pages 1633–1637. Society of Exploration Geophysicists. DOI: https://doi.org/10.1190/1.2148008.

Haq, B. U., Hardenbol, J., and Vail, P. R. (1987). Chronology of fluctuating sea levels since the triassic. *Science*, 235(4793):1156–1167. DOI: 10.1126/science.235.4793.1156.

Hay, W. W. and Southam, J. R. (1977). Modulation of marine sedimentation by the continental shelves. *The Fate of Fossil Fuel CO2 in the Oceans*, pages 569–604. DOI: DOI:10.1007/978-1-4899-5016-1_29.

Hellevang, H. (2015). Carbon capture and storage (ccs). In *Petroleum Geoscience*, pages 591–602. Springer. DOI: https://doi.org/10.1007/978-3-642-34132-8_24.

Henriksen, E., Bjørnseth, H., Hals, T., Heide, T., Kiryukhina, T., Kløvjan, O., Larssen, G., Ryseth, A., Rønning, K., Sollid, K., et al. (2011). Uplift and erosion of the greater barents sea: impact on prospectivity and petroleum systems. *Geological Society, London, Memoirs*, 35(1):271–281. DOI: https://doi.org/10.1144/M35.17.

Holford, S., Green, P., Hillis, R., Duddy, I., Turner, J., and Stoker, M. (2008). Regional uplift episodes along the ne atlantic margin constrained by stratigraphic and thermochronologic data. In *AGU Fall Meeting Abstracts*. DOI: .

Japsen, P. (1998). Regional velocity-depth anomalies, north sea chalk: a record of overpressure and neogene uplift and erosion. *AAPG bulletin*, 82(11):2031–2074. DOI: .

Japsen, P. and Chalmers, J. A. (2000). Neogene uplift and tectonics around the north atlantic: overview. *Global and Planetary Change*, 24(3-4):165–173. DOI: .

Japsen, P., Mukerji, T., and Mavko, G. (2007). Constraints on velocity-depth trends from rock physics models. *Geophysical Prospecting*, 55(2):135–154. DOI: 10.1111/j.1365-2478.2007.00607.x.

Jarsve, E., Eidvin, T., Nystuen, J., Faleide, J., Gabrielsen, R., and Thyberg, B. (2015). The oligocene succession in the eastern north sea: basin development and deposi-

tional systems. *Geological Magazine*, 152(4):668–693. DOI: https://doi.org/10.1017/S0016756814000570.

Johannesen, E. and Nøttvedt, A. (2008). Norway encircled in coastal plains and deltas. *The Making of a Land: Geology of Norway. Norsk Geologisk Forening, Trondheim*, pages 356–383. DOI: .

Jordt, H., Faleide, J. I., Bjørlykke, K., and Ibrahim, M. T. (1995). Cenozoic sequence stratigraphy of the central and northern north sea basin: tectonic development, sediment distribution and provenance areas. *Marine and Petroleum Geology*, 12(8):845–879. DOI: https://doi.org/10.1016/0264-8172(95)98852-V.

Kjennerud, T. and Sylta, Ø. (2001). Application of quantitative palaeobathymetry in basin modelling, with reference to the northern north sea. *Petroleum Geoscience*, 7(4):331–341. DOI: 10.1144/petgeo.7.4.331.

Kyrkjebø, R., Kjennerud, T., Gillmore, G., Faleide, J., and Gabrielsen, R. (2001). Cretaceous-tertiary palaeo-bathymetry in the northern north sea; integration of palaeo-water depth estimates obtained by structural restoration and micropalaeontological analysis. In *Norwegian Petroleum Society Special Publications*, volume 10, pages 321–345. Elsevier. DOI: https://doi.org/10.1016/S0928-8937(01)80020-5.

Latimer, R. B., Davidson, R., and Van Riel, P. (2000). An interpreter's guide to understanding and working with seismic-derived acoustic impedance data. *The leading edge*, 19(3):242–256. DOI: https://doi.org/10.1190/1.1438580.

Lidmar-Bergström, K., Ollier, C., and Sulebak, J. (2000). Landforms and uplift history of southern norway. *Global and Planetary Change*, 24(3-4):211–231. DOI: https://doi.org/10.1016/S0921-8181(00)00009-6.

Løseth, H., Lippard, S., Sættem, J., Fanavoll, S., Fjerdingstad, V., Leith, T., Ritter, U., Smelror, M., et al. (1993). Cenozoic uplift and erosion of the barents sea—evidence from the svalis dome area. In *Norwegian Petroleum Society Special Publications*, volume 2, pages 643–664. Elsevier. DOI: https://doi.org/10.1016/B978-0-444-88943-0.50042-3.

Makurat, A., Torudbakken, B., Monsen, K., Rawlings, C., et al. (1992). Cenezoic uplift and caprock seal in the barents sea: fracture modelling and seal risk evaluation. In

SPE Annual Technical Conference and Exhibition. Society of Petroleum Engineers. DOI: .

Marcussen, Ø., Faleide, J., Jahren, J., and Bjørlykke, K. (2010a). Mudstone compaction curves in basin modelling: A study of mesozoic and cenozoic sediments in the northern north sea. *Basin Research*, 22(3):324–340. DOI: 10.1111/j.1365-2117.2009.00430.x.

Marcussen, Ø., Maast, T. E., Mondol, N. H., Jahren, J., and Bjørlykke, K. (2010b). Changes in physical properties of a reservoir sandstone as a function of burial depth–the etive formation, northern north sea. *Marine and Petroleum Geology*, 27(8):1725–1735. DOI: https://doi.org/10.1016/j.marpetgeo.2009.11.007.

McKenzie, D. (1978). Some remarks on the development of sedimentary basins. *Earth and Planetary science letters*, 40(1):25–32. DOI: .

Metz, B., Davidson, O., De Coninck, H., et al. (2005). *Carbon dioxide capture and storage: special report of the intergovernmental panel on climate change.* Cambridge University Press. DOI: .

Molnar, P. (2004). Late cenozoic increase in accumulation rates of terrestrial sediment: How might climate change have affected erosion rates? *Annu. Rev. Earth Planet. Sci.*, 32:67–89. DOI: .

Mondol, N. H. (2015). Well logging: Principles, applications and uncertainties. In *Petroleum Geoscience*, pages 385–425. Springer. DOI: https://doi.org/10.1007/978-3-642-34132-8_16.

Mondol, N. H., Bjørlykke, K., Jahren, J., and Høeg, K. (2007). Experimental mechanical compaction of clay mineral aggregates—changes in physical properties of mudstones during burial. *Marine and Petroleum Geology*, 24(5):289–311. DOI: https://doi.org/10.1016/j.marpetgeo.2007.03.006.

Mulrooney, M., Osmond, J., Skurtveit, E., Wu, L., and Braathen, A. (2018). Smeaheia, a potential northern north sea co2 storage site: Structural description and de-risking strategies. In *Fifth CO2 Geological Storage Workshop*.

Mulrooney, M. J., Leutscher, J., and Braathen, A. (2017). A 3d structural analysis of the goliat field, barents sea, norway. *Marine and Petroleum Geology*, 86:192–212. DOI: https://doi.org/10.1016/j.marpetgeo.2017.05.038.

Nadin, P. and Kusznir, N. (1995). Palaeocene uplift and eocene subsidence in the northern north sea basin from 2d forward and reverse stratigraphic modelling. *Journal of the Geological Society*, 152(5):833–848. DOI: https://doi.org/10.1144/gsjgs.152.5.0833.

Nielsen, S., Clausen, O., Jacobsen, B. H., Thomsen, E., Huuse, M., Gallagher, K., Balling, N., and Egholm, D. (2010). The ice hypothesis stands: how the dogma of late cenozoic tectonic uplift can no longer be sustained in the light of data and physical laws. *Journal of Geodynamics*, 50(2):102–111. DOI: https://doi.org/10.1016/j.jog.2010.02.002.

Nielsen, S. B., Gallagher, K., Leighton, C., Balling, N., Svenningsen, L., Jacobsen, B. H., Thomsen, E., Nielsen, O. B., Heilmann-Clausen, C., Egholm, D. L., et al. (2009). The evolution of western scandinavian topography: a review of neogene uplift versus the ice (isostasy–climate–erosion) hypothesis. *Journal of Geodynamics*, 47(2-3):72–95. DOI: https://doi.org/10.1016/j.jog.2008.09.001.

Norton, M., Coney, P., Davis, G., et al. (1986). Collapse of the caledonian orogen and the old red sandstone. *Nature*, 323(6084):147. DOI: https://doi.org/10.1038/323147a0.

Nygård, R., Gutierrez, M., Bratli, R. K., and Høeg, K. (2006). Brittle–ductile transition, shear failure and leakage in shales and mudrocks. *Marine and Petroleum Geology*, 23(2):201–212. DOI: https://doi.org/10.1016/j.marpetgeo.2005.10.001.

Odinsen, T., Reemst, P., Van Der Beek, P., Faleide, J. I., and Gabrielsen, R. H. (2000). Permo-Triassic and Jurassic extension in the northern North Sea: results from tectonostratigraphic forward modelling. *Geological Society, London, Special Publications*, 167(1):83–103. DOI: https://doi.org/10.1144/GSL.SP.2000.167.01.05.

Ogata, K., Senger, K., Braathen, A., Tveranger, J., and Olaussen, S. (2014). The importance of natural fractures in a tight reservoir for potential co2 storage: a case study of the upper triassic–middle jurassic kapp toscana group (spitsbergen, arctic

norway). *Geological Society, London, Special Publications*, 374(1):395–415. DOI: https://doi.org/10.1144/SP374.9.

Oye, O. J., Aplin, A. C., Jones, S. J., Gluyas, J. G., Bowen, L., Orland, I. J., and Valley, J. W. (2018). Vertical effective stress as a control on quartz cementation in sandstones. *Marine and Petroleum Geology*, 98:640–652. DOI: https://doi.org/10.1016/j.marpetgeo.2018.09.017.

Patruno, S., Hampson, G. J., Jackson, C. A.-L., and Dreyer, T. (2015). Clinoform geometry, geomorphology, facies character and stratigraphic architecture of a sand-rich subaqueous delta: Jurassic sognefjord formation, offshore norway. *Sedimentology*, 62(1):350–388. DOI: https://doi.org/10.1111/sed.12153.

Praeg, D., Stoker, M., Shannon, P., Ceramicola, S., Hjelstuen, B., Laberg, J., and Mathiesen, A. (2005). Episodic cenozoic tectonism and the development of the nw european 'passive'continental margin. *Marine and Petroleum Geology*, 22(9-10):1007–1030. DOI: https://doi.org/10.1016/j.marpetgeo.2005.03.014.

Rattey, R. and Hayward, A. (1993). Sequence stratigraphy of a failed rift system: the middle jurassic to early cretaceous basin evolution of the central and northern north sea. In *Geological Society, London, Petroleum Geology Conference series*, volume 4, pages 215–249. Geological Society of London. DOI: https://doi.org/10.1144/0040215.

Richardsen, G., Vorren, T. O., and Tørudbakken, B. O. (1993). Post-early cretaceous uplift and erosion in the southern barents sea: a discussion based on analysis of seismic interval velocities. *Norsk Geologisk Tidsskrift*, 73(1):3–20. DOI: .

Riis, F. (1996). Quantification of cenozoic vertical movements of scandinavia by correlation of morphological surfaces with offshore data. *Global and Planetary Change*, 12(1-4):331–357.

Roberts, A., Yielding, G., Kusznir, N., Walker, I., and Dorn-Lopez, D. (1993). Mesozoic extension in the north sea: constraints from flexural backstripping, forward modelling and fault populations. In *Geological Society, London, Petroleum Geology Conference series*, volume 4, pages 1123–1136. Geological Society of London. DOI: https://doi.org/10.1144/0041123.

Roberts, A. M., Kusznir, N. J., Yielding, G., and Beeley, H. (2019). Mapping the bathymetric evolution of the northern north sea: from jurassic synrift archipelago through cretaceous–tertiary post-rift subsidence. *Petroleum Geoscience*, pages petgeo2018–066. DOI: https://doi.org/10.1144/petgeo2018-066.

Routh, P., Behura, J., and Tanis, M. C. (2016). Introduction to this special section: Full-waveform inversion part i. *The Leading Edge*, 35(12):1024–1024. DOI: https://doi.org/10.1190/tle35121024.1.

Russell, B. H. (1988). *Introduction to seismic inversion methods*. Society of Exploration Geophysicists. DOI: https://doi.org/10.1190/1.9781560802303.

Rutherford, S. R. and Williams, R. H. (1989). Amplitude-versus-offset variations in gas sands. *Geophysics*, 54(6):680–688. DOI: https://doi.org/10.1190/1.1442696.

Sclater, J. G. and Christie, P. A. (1980). Continental stretching: An explanation of the post-mid-cretaceous subsidence of the central north sea basin. *Journal of Geophysical Research: Solid Earth*, 85(B7):3711–3739. DOI: https://doi.org/10.1029/JB085iB07p03711.

Shukla, R., Ranjith, P., Haque, A., and Choi, X. (2010). A review of studies on co2 sequestration and caprock integrity. *Fuel*, 89(10):2651–2664. DOI: https://doi.org/10.1016/j.fuel.2010.05.012.

Simm, R., Bacon, M., and Bacon, M. (2014). *Seismic Amplitude: An interpreter's handbook*. Cambridge University Press.

Smith, G. and Gidlow, P. (1987). Weighted stacking for rock property estimation and detection of gas. *Geophysical Prospecting*, 35(9):993–1014. DOI: https://doi.org/10.1111/j.1365-2478.1987.tb00856.x.

Stewart, D., Schwander, M., and Bolle, L. (1995). Jurassic depositional systems of the horda platform, norwegian north sea: Practical consequences of applying sequence stratigraphic models. In *Norwegian Petroleum Society Special Publications*, volume 5, pages 291–323. Elsevier. DOI: https://doi.org/10.1016/S0928-8937(06)80073-1.

Stoker, M. S., Praeg, D., Hjelstuen, B. O., Laberg, J. S., Nielsen, T., and Shannon, P. M. (2005). Neogene stratigraphy and the sedimentary and oceanographic development of the nw european atlantic margin. *Marine and Petroleum Geology*, 22(9-10):977–1005. DOI: https://doi.org/10.1016/j.marpetgeo.2004.11.007.

Storvoll, V., Bjørlykke, K., and Mondol, N. H. (2005). Velocity-depth trends in mesozoic and cenozoic sediments from the norwegian shelf. *AAPG bulletin*, 89(3):359–381. DOI: https://doi.org/10.1306/10150404033.

the Ministry of Petroleum and Energy (2014). The Government's carbon capture and storage strategy kernel description. DOI: .

Thyberg, B., Jahren, J., Winje, T., Bjørlykke, K., Faleide, J. I., and Marcussen, Ø. (2010). Quartz cementation in late cretaceous mudstones, northern north sea: changes in rock properties due to dissolution of smectite and precipitation of microquartz crystals. *Marine and Petroleum Geology*, 27(8):1752–1764. DOI: https://doi.org/10.1016/j.marpetgeo.2009.07.005.

Walderhaug, O. (1996). Kinetic modeling of quartz cementation and porosity loss in deeply buried sandstone reservoirs. *AAPG bulletin*, 80(5):731–745. DOI: .

Whipp, P., Jackson, C. A.-L., Gawthorpe, R., Dreyer, T., and Quinn, D. (2014). Normal fault array evolution above a reactivated rift fabric; a subsurface example from the northern horda platform, norwegian north sea. *Basin Research*, 26(4):523–549. DOI: https://doi.org/10.1111/bre.12050.

Whitcombe, D. N., Connolly, P. A., Reagan, R. L., and Redshaw, T. C. (2002). Extended elastic impedance for fluid and lithology prediction. *Geophysics*, 67(1):63–67. DOI: https://doi.org/10.1190/1.1451337.

Worden, R. and Burley, S. (2003). Sandstone diagenesis: the evolution of sand to stone. *Sandstone Diagenesis: Recent and Ancient*, 4:3–44. DOI: .

Zoeppritz, K. (1919). Erdbebenwellen vii. *Nachrichten von der Gesellschaft der Wissenschaften zu Göttingen, Mathematisch-Physikalische Klasse*, 1919:57–65.